NTNU

Norwegian University of
Science and Technology

Calculation of Wavefunction Overlaps in First Principles Electronic Structure Codes

Dara Goldar

Master of Science in Physics and Mathematics
Submission date: July 2017
Supervisor: Jon Andreas Støvneng, IFY
Co-supervisor: Trond Brudevoll, FFI
Asta-Katrine Storebø, FFI

Norwegian University of Science and Technology
Department of Physics

Glossary

I Region of spheres centered around atomic sites in unit cell.

II Interstitial region in unit cell, covering everything except for region I spheres.

$J^{II}_{\mu\mu'}$ Integral involving initial and final wavefunctions of charge carrier. Taken over region II in unit cell.

$J^{I}_{\mu\mu'}$ Integral involving initial and final wavefunctions of charge carrier. Taken over region I in unit cell.

$J_{\mu\mu'}$ Integral involving initial and final wavefunctions of charge carrier.

L $\{l, m\}$. Compact notation for angular quantum number and magnetic quantum number.

N Number of bands participating in wannierization; number of lattice points in real-space supercell.

$P^{m}_{nn'}(\boldsymbol{k}, \boldsymbol{k'})$ Scattering probability per unit time from initial to final state for scattering mechanism m.

R_β Radius of sphere β.

$U^{\dagger}_{nm}(\boldsymbol{k})$ The conjugate-transpose of the unitary matrix that produces Maximally localized Wannier functions.

$U_{nm}(\boldsymbol{R})$ Unitary matrix contribution from lattice point $\boldsymbol{R}$, involved in Wannier interpolation.

$U_{nm}(\boldsymbol{k})$ Unitary matrix involved in Wannier transformation. The matrix is picked such that it maximally localized the Wannier functions according to a particular localization criterion.

V Volume of unit cell.

V_β Volume of region I sphere β.

$Y_L(\hat{\boldsymbol{r}}_{\boldsymbol{\beta}})$ Spherical harmonics function.

$\Phi^{\beta}_{L\sigma}(\boldsymbol{r}_\beta, E_l)$ Basis function acquired in the Scalar relativistic approximation using Dirac's equation. May be split into a radial part and an angular part: $\Phi^{\beta}_{L\sigma}(\boldsymbol{r}_\beta, E_l) = u^{\beta}_{l\sigma}(r_\beta, E_l)Y_L\hat{\boldsymbol{r}}_\beta$.

$\boldsymbol{K}$ Reciprocal lattice vector, involved in conservation of momentum for a scattering process.

$\boldsymbol{R}$ Bravais lattice vector.

$\boldsymbol{R}_\beta$ Vector originating in global origin of unit cell, and terminating at atomic site β; the local origin inside sphere β.

$\boldsymbol{q}$ Fourier component of perturbed potential.

$\boldsymbol{r}$ Global coordinate in the unit cell.

γ Compact notation for $\{n, \boldsymbol{\sigma}, \boldsymbol{R}\}$; band index, spin and lattice vector, respectively.

μ Compact notation for $\{n, \boldsymbol{\sigma}, \boldsymbol{k}\}$; band index, spin and wavevector, respectively.

$\omega_\gamma(\boldsymbol{r})$ Wannier function used in the calculation of overlap factors.

$\psi_\mu(\boldsymbol{r})$ Wavefunction of carrier state undergoing scattering.

r_β Local coordinate inside sphere β of region I.

$u.c$ Unit cell.

$u_\mu(\boldsymbol{r})$ Cell-periodic part of carrier wavefunction in state μ.

x Integration constant given by $R_\beta|\boldsymbol{G}_2 - \boldsymbol{G}_1 + \boldsymbol{K}|$ where $\boldsymbol{G}_1$, $\boldsymbol{G}_2$ and $\boldsymbol{K}$ are reciprocal lattice vectors.

$\mathbf{0}_{\boldsymbol{R}}$ Reference lattice point.

$\boldsymbol{\sigma}$ Spin orientation of initial carrier state.

$\boldsymbol{\sigma}'$ Spin orientation of final carrier state.

$\boldsymbol{k}$ Wavevector of initial carrier state.

$\boldsymbol{k}'$ Wavevector of final carrier state.

$\dot{u}^{\beta}_{l\sigma}(r_\beta, E_{1,l})$ Radial component of basis function, $u^{\beta}_{l\sigma}(r_\beta, E_{1,l})$, differentiated with respect to energy: $\equiv \frac{du_l(r_\beta, E_{1,l})}{dE}\big|_{E_{1,l}}$.

$a^{\beta}_{\gamma,L}$ Expansion coefficient for region I Wannier function, associated with $u_l(r_\beta, E_{1,l})$.

$a^{\beta}_{\mu,L}$ Expansion coefficient for region I in (L)APW(+lo) basis set, associated with $u_l(r_\beta, E_{1,l})$.

$b^{\beta}_{\gamma,L}$ Expansion coefficient for region I Wannier basis function, associated with $\dot{u}_l(r_\beta, E_{1,l})$.

$b^{\beta}_{\mu,L}$ Expansion coefficient for region I in (L)APW(+lo) basis set, associated with $\dot{u}_l(r_\beta, E_{1,l})$.

$C^{m}_{nn'}(\boldsymbol{k}, \boldsymbol{k'})$ Scattering interaction element for transition from initial to final state for scattering mechanism m.

$c^{\beta}_{\gamma,L}$ Expansion coefficient for region I Wannier function, associated with $u_l(r_\beta, E_{1,l})$.

$C^{\beta}_{\gamma}(\boldsymbol{G})$ Expansion coefficient for region II Wannier function, associated with $e^{i\boldsymbol{G}\cdot\boldsymbol{r}}$.

$c^{\beta}_{\mu,L}$ Expansion coefficient for region I in (L)APW(+lo) basis set, associated with $u_l(r_\beta, E_{1,l})$.

$C^{\beta}_{\mu}(\boldsymbol{G})$ Expansion coefficient for region II in (L)APW(+lo) basis set, associated with $e^{i(\boldsymbol{k}+\boldsymbol{G})\cdot\boldsymbol{r}}$.

$G_{\mu\mu'}$ Wavefunction overlap factor for transition from state $\mu = \{n, \boldsymbol{\sigma}, \boldsymbol{k}\}$ to $\mu' = \{n', \boldsymbol{\sigma'}, \boldsymbol{k'}\}$ for scattering mechanism m.

$G_{nn'}(\boldsymbol{k}, \boldsymbol{k'})$ Wavefunction overlap factor for transition from state $\{n, \boldsymbol{k}\}$ to $\{n', \boldsymbol{k'}\}$ for scattering mechanism m.

$j_l(x)$ Bessel function of the first kind.

l Angular momentum quantum number.

m Magnetic quantum number; scattering mechanism in Fermi's Golden Rule.

$M^{m}_{nn'}(\boldsymbol{k}, \boldsymbol{k'})$ Matrix element for transition from state $\{n, \boldsymbol{k}\}$ to $\{n', \boldsymbol{k'}\}$ for scattering mechanism m.

n Band index of initial carrier state.

n' Band index of final carrier state.

$u^{\beta}_{l\sigma}(r_\beta, E_{1,l})$ Radial component of basis function acquired in the Scalar relativistic approximation.

$u^{\beta}_{l\sigma}(r_\beta, E_{2,l})$ Radial component of basis function acquired in the Scalar relativistic approximation. Evaluated at a different energy $E_{2,l}$ than $u^{\beta}_{l\sigma}(r_\beta, E_{1,l})$.

x_σ Two-component spinor.

Acronyms

(L)APW(+lo) (Linearized) Augmented plane-wave (+ local orbitals).

AMF Around mean-field.

APW Augmented plane-wave.

APW+lo Augmented plane-wave + local orbitals.

BTE Boltzmann transport equation.

BZ Brillouin-zone.

DFT Density functional theory.

FLL Fully localized limit.

GGAs Generalized gradient approximations.

KS Kohn-Sham.

L(S)DA Local (spin) density approximation.

LAPW Linearized augmented plane-wave.

LDA Local density approximation.

MC Monte Carlo.

MLWFs Maximally localized Wannier functions.

SCF Self-consistent field.

SOC Spin-orbit coupling.

SRA Scalar relativistic approximation.

WFs Wavefunctions.

Abstract

In the work with this Master thesis, expressions for the wavefunction overlap factor between eigenfunctions are obtained. These expressions should be suitable for numeric integration over the Brillouin zone, and are derived in the Linearized Augmented plane-wave (+local orbitals) ((L)APW(+lo)) and Maximally localized Wannier functions (MLWFs) bases. The expression obtained for both bases is found to be suitable for numeric integration over the Brillouin zone. A routine computing the (L)APW(+lo) overlap has been implemented for normal scattering processes. Based on a Wien2k-simulation for GaAs, the bandstructure of GaAs is discussed. Furthermore, the implemented routine is used to plot the norm of near-band edge states. As expected, values very close to 1 are obtained. The distribution of the wavefunction between the two regions of the Augmented plane-wave method is also discussed for the near-band edge electron states.

I arbeidet med denne masteroppgaven har uttrykk for overlappintegralet mellom egenfunksjoner blitt beregnet. Uttrykkene skal være passende for numerisk integrasjon over Brillouinsonen, og er bergenet i de respektive basisene som på engelsk heter Linearized Augmented plane-wave (+local orbitals) ((L)APW(+lo)) og Maximally localized Wannier functions (MLWFs). De beregnede uttrykkene er vurdert til å passe for numerisk integrasjon over Brillouinsonen, og for (L)APW(+lo) er overlappet implementert for normale spredningsprosesser. Med utgangspunkt i en Wien2k-simulering på GaAs er båndstrukturen og normen til egenfunksjoner presentert. For bånd nær båndgapet er i tillegg fordelingen av bølgefunksjonen mellom de to regionene i Augmented plane-wave-metoden diskutert.

Table of Contents

Glossary iii

Acronyms vi

Abstract vii

Table of Contents x

1 Introduction 1

2 Theory 7
2.1 Scattering rates & Fermi's golden rule . . . 7
2.2 Density functional theory . . . 9
2.2.1 Kohn - Sham equations . . . 9
2.2.2 Spin-polarized systems . . . 11
2.2.3 L(S)DA+U . . . 12
2.2.4 Self-consistent cycle & the secular equation . . . 13
2.3 Full potential Augmented plane-wave method . . . 15
2.3.1 The original APW method . . . 15
2.3.2 LAPW . . . 17
2.3.3 APW+lo . . . 18
2.3.4 Kinetic energy operator . . . 18
2.3.5 Lattices with inversion symmetry . . . 19
2.3.6 Potential expansion . . . 20
2.3.7 Dirac equation & the Scalar Relativistic approximation . . . 20
2.3.8 Including Spin-orbit coupling as a second variational step . . . 24
2.3.9 (L)APW(+lo) . . . 26
2.4 Wannier functions . . . 27
2.4.1 Wannier transformation . . . 28
2.4.2 Maximally localized Wannier functions . . . 28
2.5 Gaunt numbers . . . 29

3 Matrix elements **31**
3.1 (L)APW(+lo) overlap . . . 32
3.1.1 Region I . . . 33
3.1.2 Region II . . . 37
3.1.3 Total overlap . . . 40
3.2 Wannier overlap . . . 41
3.2.1 Region I . . . 42
3.2.2 Region II . . . 46
3.2.3 Total overlap . . . 48
3.2.4 Wannier interpolation of matrix elements . . . 49

4 Implementation **51**
4.1 Output from first principles programs . . . 51
4.2 Overlap routines . . . 52
4.2.1 (L)APW(+lo) overlap . . . 52
4.2.2 Wannier overlap . . . 53
4.2.3 Spin-dependent overlap . . . 54
4.3 Numeric suitability for Brillouin-zone integration . . . 54

5 Results **55**
5.1 GaAs . . . 55

6 Conclusion **61**

Bibliography **61**

Chapter 1

Introduction

Computational electronics is increasingly playing an important role in explaining physical phenomena in semiconductor devices. As the size of electronic components enters the nanometer regime, the behavior of these components becomes ever more complex. At the nanometer scale, new physical phenomena, only occurring at the shortest scales, must be accounted for. The processes involved in manufacturing electronic components in the nanometer regime are usually too complex and time-consuming for a trial-and-error approach. Computational electronics offers the electronic engineer insight into component behavior at a significantly lower cost. Another exciting application of computational electronics is the investigation of hypothetical devices: electronic components that are currently not technologically feasible to manufacture may be modeled through computational simulations. Last, device simulations permits the engineer to observe aspects of device behavior that are impossible to observe in the laboratory, either due to the laws of quantum mechanics or limitations on sensors. Electronic device simulations should not only provide a sufficiently sophisticated model, but preferably do so at minimal computational cost [1, 2].

This thesis deals with the calculation of scattering matrix elements based on first principles generated eigenfunctions and band structures from *Density functional theory* (DFT) software Wien2k [3]. The work done here is part of a larger project aiming at providing a general purpose *Monte Carlo* (MC) particle simulator to be used in the fields of materials technology and semiconductor optoelectronic devices [4]. The program should be general purpose in the sense that it simulates various materials or devices equally well, with little effort needed switching from one material to another. As no transport simulations from the MC program are presented here, the MC method will only be discussed in light of the scattering matrix elements it takes as input. For more detail on the MC method, the reader is referred to *The Monte Carlo Method for Semiconductor Device Simulation* by C. Jacoboni and P. Lugli[5].

The Monte Carlo program accepts analytical as well as tabulated band structures as input. The analytical band model has a well-defined mathematical representation; the tabulated model is a discrete representation of the band structure over the Brillouin-zone, obtained from first principles calculations. In previous work by Karlsen, Selvåg and Bergslid, Monte Carlo simulations are presented, using scattering rates calculated from the $\boldsymbol{k} \cdot \boldsymbol{p}$ method as well as full-band data acquired from ab-initio pseudopotential software ABINIT [6, 7, 8, 9]. In the case of ab-initio software ABINIT, the scattering rates are based on first principles tabulated band structures, but the carrier state wavefunctions involved are calculated from the 14×14 $\boldsymbol{k} \cdot \boldsymbol{p}$ [10]. The $\boldsymbol{k} \cdot \boldsymbol{p}$ method requires empirical input to determine the hamiltonian matrix. Furthermore, the method is not expected to give an accurate description of the wavefunction near the Brillouin-zone edges as only first-order perturbation terms are accounted for. Although the band data is ab-initio, the wavefunctions are not. The chief achievement of the current scheme, then, is the step from a semi-experimental, pertubative approach, used to describe the carrier state wavefunctions to a description based solely on first principles electronic structure codes, valid over the entire Brillouin-zone.

The scattering matrix elements arrived upon must be applicable for the MC program. In the current MC simulator, carrier movement is treated classically, while scattering events are treated quantum mechanically. To determine the probability distribution of the free flights duration, i.e the time interval between two scattering events, one must integrate the scattering matrix elements over the Brillouin-zone. In addition, the MC program assumes a decomposition of the matrix elements into two parts: the first part is an interaction matrix element which depends on the particular scattering mechanism that the carrier undergoes. The second is an overlap integral between initial and final wavefunction state, referred to as the wavefunction overlap factor. It is the wavefunction overlap factor that we are interested in. The details of this decomposition are shown in Chapter 2.1. Since the wavefunction overlap elements are tabulated, we demand that they be suitable for numeric integration over the Brillouin-zone.

In a specialization project by this author, a *Local density approximation* (LDA) based DFT approach was shown to underestimate the band gap in the alloy HgCdTe [2]. Generally, the LDA+DFT approach is known to systematically underestimate the band gap by about 40% [11]. LDA by itself overestimates the energy level of deep-lying d states; a Hubbard model U will better account for the strongly correlated d states, and was in the mentioned specialization project shown to increase the band gap of HgCdTe. To tackle the systematic band gap underestimation, a modified Becke-Johnson potential should be used [12]. Finally, with respect to alloy semiconductors, it is possible to use a backfolding approach: One conducts supercell calculations, yielding a smaller supercell band structure as compared with that of a normal unit cell calculation. The supercell band structures must then in a second step be folded back to the larger unit cell band structure. This may be done using a spectral weight approach [13]. In summary, the band structures and eigenfunctions, to be used in the MC program, should be obtained using a DFT+U+mBJ+backfolding approach.

In addition to simulating carrier transport using the Wien2k augmented plane-wave representation, it is possible to use a real-space basis known as the *Maximally localized Wannier functions* (MLWFs). There are a number of advantages associated with the use of a ML-

WFs representation compared to the original (L)APW(+lo). First of all, the current Monte Carlo program uses band structures and potentially eigenfunctions from external ab-initio programs. Various ab-initio programs will generally be based on different bases, respectively. A standardization, where one does not need to worry about the basis in which input parameters are represented, will obviously make the transport program more attractive. One simply converts a specific ab-initio representation into a standardized representation used for the Monte Carlo program. In order to implement such a standardization, one needs a general algorithm able to change the representation found in most ab-initio programs to the standardized functions used. Indeed, such an algorithm has been developed by Nicola Marzari, Ivo Souza and David Vanderbilt, that iteratively transforms a set of Bloch orbitals obtained from a first principles calculation into a set of MLWFs. This algorithm works without regard to the particular first principles calculation technique adopted or the basis set, and therefore satisfies the requirements needed for a standardization of the Monte Carlo program [14]. Second, the Wannier representation is well-suited for quantum transport. MLWFs offer a compact representation, yielding much simplified tight-binding like operations related to band structure and transport calculations. Currently, band structure and transport are done in series, but in simulation of very small devices, band structures must be recalculated in parallel with the transport simulation to account for internal redistribution of charge [1]. This represents a formidable computational task and is done at a lower computational cost in a tight-binding-like representation. A final advantage of the Wannier representation is linear scaling. Linear scaling methods are electronic structure calculation methods where the computational cost increases linearly with the size of the system. One uses results from electronic-structure calculations on smaller systems to model larger ones. Due to the above reasons, it may be expedient to post-process the Wien2k data using the Wien2k-interface software Wien2Wannier and the program Wannier90, carrying eigenfunctions in the (L)APW(+lo) representation over to a MLWFs basis [15, 16]. It should be emphasized that Wannier functions are to be used only when they are beneficial in their own right for the particular problem at hand. Possibly, both the (L)APW(+lo) method and Wannier representation will be available in the Monte Carlo simulations.

Electronic transport in semiconductors is governed by the *Boltzmann transport equation* (BTE), which is commonly solved either analytically or by MC simulation. With respect to the (L)APW(+lo) and Wannier bases, two interesting schemes, based on solving the Boltzmann transport equations (BTEs) in the relaxation time approximation are available. The relaxation time τ represents the overall contribution to transport from scattering mechanisms; there is indeed a formal connection [10]. The first scheme is presented by Madsen et al. (2006), a software named BoltzTraP [17]. BoltzTraP is a code for calculating transport quantities such as the semi-classic Seebeck and Hall coefficients using the (L)APW(+lo) basis. Band structures are Fourier expanded and interpolated to obtain an analytical band structure. The analytical expression readily permits the computation of transport quantities such as first and second derivatives of the band structure. Once analytical band structure expressions are obtained, the Botzmann transport equations (BTEs) are solved in the relaxation time approximation. In its early days, the code assumed constant relaxation time, but since recently accepts an energy-dependent model, i.e where $\tau = \tau(\epsilon)$. The second scheme, BoltzWann, is presented by G. Pizzi et al. (2014) [18]. Also based on BTEs

within the relaxation time approximation, BoltzWann calculates band structure dependent quantities using the Wannier representation. Analytical band structures are obtained using Wannier interpolation, making band structure-dependent quantities easily accessible. While BoltzTrap accounts for an energy-dependent relaxation time model, BoltzWann is able to use any model for the relaxation time, even those based on first principles calculations. Although the above methods differ fundamentally from MC in that the BTEs are solved in the relaxation time approximation, rather than using pseudorandom numbers to simulate transport, we may capitalize on the interpolation schemes presented in BoltzWann and BoltzTrap in the MC scheme. Fourier and Wannier interpolation offer a way of saving data on a coarse mesh and then interpolate without significant loss of precision. In particular, one should consider two possible applications for the MC program: First, when dealing with the wavefunction overlap factor between states of differing wavenumber $\boldsymbol{k}$ and $\boldsymbol{k}'$. The amount of data needed to tabulate the wavefunction overlap factors on a fine mesh is impractical, and Fourier or Wannier interpolation permits a coarser grid without significant loss of detail. Second, Bergslid (2013) reported in his work on the current MC program a so-called ripple effect from the Brillouin-zone-integration. Currently, the Gilat-Raubenheimer method is employed for Brillouin-zone-integration, and for finer grid the bands are interpolated using a method by Fischetti & Laux [19, 20]. To prevent the ripple effect reported by Bergslid, a band interpolation scheme developed by E. Pickett et al. (1988), on which the BoltzTrap interpolation scheme is based, may be of interest [21].

With regard to the wavefunction overlap factors to be calculated in this thesis, packages exist which calculate optical matrix elements in the (L)APW(+lo) and Wannier bases, respectively, based on first principles code Wien2k. Ambrosch-Draxl et al. (2006) presents a scheme, implemented in Wien2k as Optic, for calculating optical properties within the random-phase approximation using the full-potential LAPW method [22, 23]. Since Ambrosch-Draxl et al. are interested in the dielectric constant, they develop an expression involving momentum matrix elements in the LAPW basis. Another package, Woptic, developed by Assmann et al. (2015), calculates the optical conductivity in a basis of Maximally localized Wannier functions. Within the framework of dynamical-mean-field-theory, a method to determine the electronic structure of strongly correlated materials, the optical conductivity is given as a Brillouin-zone sum involving dipole matrix elements expressed in terms of Wannier functions [24, 25, 26]. Once a Wien2k-simulation has been run, optical matrix elements may be extracted, either from the program Optic or Woptic, according to what basis is used: (L)APW(+lo) or Wannier. These dipole matrix elements are then fed into the MC program. As mentioned above, the MC program assumes a decomposition of the scattering matrix element in Fermi's Golden Rule, meaning both the interaction matrix element and the wavefunction overlap factor are required. In the case of matrix elements from Optic and Woptic, no such decomposition is made. The appropriate way to employ these dipole matrix elements is therefore to input them as the interaction element while the wavefunction overlap factor between initial and final scattering states is set to identity. Finally, Fabien Tran has developed a routine computing the wavefunction overlap factor between (L)APW(+lo) functions. Although this is exactly the kind of operator matrix elements needed for the MC program, the routine applies only to identical initial and final wavevectors; if initial wavevector differs from final wavevector, some phase factors will be missing from the wavefunction overlap factor [27].

The discussion above on Wannier functions, the packages Boltztrap, Boltzwann, Optic and Woptic is based on a similar discussion presented in a specialization project by this author [2].

This thesis is organized as follows: In Chapter 2, relevant theory for the calculation of scattering matrix elements is presented. This includes topics such as Scattering rates & Fermi's Golden Rule, Density Functional theory, the Full-potential Augmented plane-wave method, Wannier functions and Gaunt numbers. In Chapter 3, we first calculate scattering rates in the (L)APW(+lo) basis set and Wannier basis, respectively. In Chapter 4, we consider the computation of scattering rates as well as numeric suitability of the scattering rates. Finally, in Chapter 5, we apply the scheme developed to investigate the electron states og GaAs near the band edge.

Chapter 2

Theory

In this chapter, theory relevant for the calculation and computation of scattering operator matrix elements used in MC simulation of electron transport is discussed. Some of the theory is built on that of a specialization project written by this author [2]. Chapters 2.1 and 2.4 have merely been improved with tidier notation, while all other sections involve more comprehensive changes. The discussions on APW, LAPW and local orbitals have been rewritten entirely. New sections have been added on the following topics: the secular equation, the scalar relativistic approximation, the inclusion of spin-orbit effects as a second variational step, inversion symmetries, the kinetic energy operator, and finally Gaunt numbers. In summary, except for the section on scattering rates and Wannier functions, all material in this chapter is either new or it has been changed significantly.

2.1 Scattering rates & Fermi's golden rule

A number of different scattering mechanisms contribute to the transport of electrons, some of them being

- Acoustic deformation potential phonon scattering
- Acoustic piezoelectric phonon scattering
- Polar optical phonon scattering
- Nonpolar optical phonon scattering
- Ionized impurity scattering
- Neutral impurity scattering
- Carrier-carrier scattering

- Alloy scattering

Depending on material, temperature and carrier concentration, some of the mechanisms play a negligible role in carrier transport and may be omitted. The scattering rates are in the Monte Carlo program given in first-order time-dependent perturbation theory. The probability of transition per unit time from one energy eigenstate to another for a particular scattering mechanism is according to Fermi's Golden Rule given as

$$P^m_{nn'}(\boldsymbol{k},\boldsymbol{k'}) = \frac{2\pi}{\hbar}\left|M^m_{nn'}(\boldsymbol{k},\boldsymbol{k'})\right|^2 \delta\Big(E_n(\boldsymbol{k}) + \Delta E^m(\boldsymbol{k},\boldsymbol{k'}) - E_{n'}(\boldsymbol{k'})\Big) \tag{2.1}$$

where the initial state is labeled by band index n and wavevector $\boldsymbol{k}$ and the final state labeled by $\{n', \boldsymbol{k'}\}$. $M^m_{nn'}(\boldsymbol{k},\boldsymbol{k'})$ represents the matrix element for the transition, depending on the initial and final state as well as the perturbed potential; m denotes the particular scattering mechanism at play. $\Delta E^m(\boldsymbol{k},\boldsymbol{k'})$ is the energy difference between initial and final carrier undergoing scattering. Finally, $E_n(\boldsymbol{k})$ is the dispersion relation for band n. While the δ-function ensures energy conservation, the interaction matrix element ensures momentum conservation. In the context of Bloch states, the momentum conservation holds only up to a reciprocal lattice vector: $\boldsymbol{k} - \boldsymbol{k'} + \boldsymbol{q} = \boldsymbol{K}$. Here, $\boldsymbol{q}$ denotes a Fourier component of the perturbed potential. In the case of carrier-phonon scattering, it is interpreted as $\pm$ the phonon momentum, depending on whether the phonon is absorbed or emitted, respectively. $\boldsymbol{K}$ represents a reciprocal lattice vector. If $\boldsymbol{K}$ is nonzero, the scattering process is referred to as an Umklapp process. If zero, it is referred to as a normal scattering process.

It is often convenient to decompose the matrix element into a part involving the scattering interaction and another the overlap between initial and final scattering states, referred to as the wavefunction overlap factor

$$\left|M^m_{nn'}(\boldsymbol{k},\boldsymbol{k'})\right|^2 = \left|C^m_{nn'}(\boldsymbol{k},\boldsymbol{k'})\right|^2 G_{nn'}(\boldsymbol{k},\boldsymbol{k'}) \tag{2.2}$$

While $C^m_{nn'}(\boldsymbol{k},\boldsymbol{k'})$ represents the scattering interaction element, generally depending on the particular interaction as well as initial and final carrier states, $G_{nn'}(\boldsymbol{k},\boldsymbol{k'})$ involves only the wavefunctions. The latter is an integral taken over the unit cell and only involves the cell-periodic part of the initial and final Bloch wave. The decomposition in (2.2) is strictly speaking formal, i.e

$$\left|C^m_{nn'}(\boldsymbol{k},\boldsymbol{k'})\right|^2 = \frac{\left|M^m_{nn'}(\boldsymbol{k},\boldsymbol{k'})\right|^2}{G_{nn'}(\boldsymbol{k},\boldsymbol{k'})} \tag{2.3}$$

In practicality though, one often approximates this relation by assuming the interaction to be constant over the unit cell. See for example Chapter 6.5 of J. Singh, *Electronic and optoelectronic properties of semiconductor structures* [10, 28]. In MC transport simulations, we are often not interested in the spin orientation of initial and final states. To appropriately deal with this, one averages over initial spin states and sums over final ones

$$G_{nn'}(\boldsymbol{k}, \boldsymbol{k'}) = \frac{1}{2} \sum_{\boldsymbol{\sigma}} \sum_{\boldsymbol{\sigma'}} G_{\mu\mu'} \tag{2.4}$$

where $G_{\mu\mu'}$ is the wavefunction overlap factor between initial state μ with spin $\boldsymbol{\sigma}$ and final state μ' with spin $\boldsymbol{\sigma}$. μ by itself already includes the spin orientation, used as a compact notation for $\{n, \boldsymbol{\sigma}, \boldsymbol{k}\}$; namely band index, spin and wavenumber, respectively. $G_{\mu\mu'}$ is given by

$$G_{\mu\mu'} = \Big| \int_{\text{u.c}} d^3 r u^*_{\mu'}(\boldsymbol{r}) u_{\mu}(\boldsymbol{r}) e^{i\boldsymbol{K}\cdot\boldsymbol{r}} \Big|^2 \tag{2.5}$$

where $\boldsymbol{K}$ is again a reciprocal lattice vector and $u_\mu(\boldsymbol{r})$ is the cell-periodic part of the Bloch state. The integral in (2.5) runs over the unit cell. If the scattering interaction $\left|C^m_{nn'}(\boldsymbol{k}, \boldsymbol{k'})\right|^2$ for a particular scattering mechanism is known, then only $G_{nn'}(\boldsymbol{k}, \boldsymbol{k'})$ is needed to determine the scattering rate. The interaction matrix element $\left|C^m_{nn'}(\boldsymbol{k}, \boldsymbol{k'})\right|^2$ may be found for a number of scattering mechanisms from Brudevoll et al. (1990) and Ridley B. K, *Quantum Processes in Semiconductors* [29, 30].

2.2 Density functional theory

To calculate scattering rates with Fermi's golden rule, the energy bands and wavefunctions of initial and final states must be available. This information may be obtained using *Density functional theory* (DFT). DFT is a computational quantum-mechanical method used in the investigation of many-body systems. The essence of the method is to treat the electron density of the many-body system as a functional; namely a function of functions. First, the Hohenberg-Kohn theorem and Kohn-Sham equations are presented, before the exchange-correlation potential is investigated. At the end, the self-consistent solution method and the secular equation are discussed.

2.2.1 Kohn - Sham equations

The Hohenberg-Kohn theorem states that for a given system, the total energy may be given as a functional of the ground state electron density. Furthermore, this ground state electron density minimizes the total energy functional. Both electron interactions and external potentials are taken into account in the total energy functional. For our purposes, a given system denotes the crystal of interest and the external potential is the Coulomb potential from the nuclei crystal. While the original theorems applied to non-magnetic systems, it has later been generalized to take spin-polarization into account.

Starting with the non-magnetic version, the energy functional reads

$$E = E[\rho] \tag{2.6}$$

Even though the Hohenberg-Kohn theorem guarantees that an energy functional exists, it does not provide any model for the energy functional itself. For density functional theory to be useful, it is vital that the model used for the functional is sufficiently accurate. The functional may be decomposed into a set of terms corresponding to different kinds of energy contributions

$$E[\rho] = T_s[\rho] + E_{ei}[\rho] + E_H[\rho] + E_{ii}[\rho] + E_{xc}[\rho] \tag{2.7}$$

T_s is the single particle kinetic energy, E_{ei} is the energy due to the Coulomb interaction between electrons and nuclei, and E_{ii} comes from nucleon-nuclei interactions. The electron-electron interaction is decomposed into E_H and E_{xc}. These are given by

$$E_H[\rho] = \frac{e^2}{2} \int d^3r d^3r' \frac{\rho(\boldsymbol{r})\rho(\boldsymbol{r'})}{|\boldsymbol{r} - \boldsymbol{r'}|} \tag{2.8}$$

$$E_{xc}[\rho] = \int d^3r \rho(\boldsymbol{r}) \epsilon_{xc}(\rho(\boldsymbol{r})) \tag{2.9}$$

The Hartree energy originates from the Coulomb repulsion between electrons, and its analytical expression is given exactly. On the other hand, the exchange-correlation term is not known; it must be approximated by defining $E_H[\rho]$ appropriately. The expression in (2.9) corresponds to a *Local density approximation* (LDA) since ϵ_{xc} is a function local in the density. Another common model, the *Generalized gradient approximations* (GGAs), includes the local density as well as the local gradient.

In order to determine the ground state energy and ground state density, the total density is expressed in terms of single particle densities

$$\rho(\boldsymbol{r}) = \sum_i^N \phi_i^*(\boldsymbol{r})\phi_i(\boldsymbol{r}) \tag{2.10}$$

Here, i runs over the N electrons present in the crystal structure, and $\phi_i(\boldsymbol{r})$ is the single particle wavefunction for electron i. Next, the variational principle is invoked to find the ground state energy with respect to $\rho(\boldsymbol{r})$. Doing so yields the *Kohn-Sham* (KS) equations as shown by W. Kohn and L. J. Sham in 1965 [31]

$$V^{KS}\phi_i(\boldsymbol{r}) = \big(T + V_{ei}(\boldsymbol{r}) + V_H(\boldsymbol{r}) + V_{xc}(\boldsymbol{r})\big)\phi_i(\boldsymbol{r}) = \epsilon_i\phi_i(\boldsymbol{r}) \tag{2.11}$$

$$\rho(\boldsymbol{r}) = \sum_i^N \phi_i(\boldsymbol{r})\phi_i^*(\boldsymbol{r}) \tag{2.12}$$

where V^{KS} is the KS potential. T is the single particle kinetic energy operator, V_{ei} denotes the Coulomb potential operator due to electron-nuclei interactions for orbital $\phi_i(\boldsymbol{r})$, V_H represents the Coulomb interaction between electrons, and V_{xc} stands for the exchange-correlation potential. Finally, ϵ_i is the KS eigenvalue corresponding to the KS orbital $\phi_i(\boldsymbol{r})$. $V_H(\boldsymbol{r})$ and $V_{xc}(\boldsymbol{r})$ are explicitly given by

$$V_H(\boldsymbol{r}) = e^2 \int d^3\boldsymbol{r'} \frac{\rho(\boldsymbol{r'})}{|\boldsymbol{r} - \boldsymbol{r'}|} \tag{2.13}$$

$$V_{xc}(\boldsymbol{r}) = \frac{\delta E_{xc}[\rho]}{\delta \rho(\boldsymbol{r})} \tag{2.14}$$

In (2.12), the sum again runs over the N electrons in the crystal. The total energy is related to the KS eigenvalues through

$$E = \sum_i^N \epsilon_i - E_H[\rho] + E_{xc}[\rho - \int \frac{\delta E_{xc}[\rho]}{\delta \rho} \rho(\boldsymbol{r}) d\boldsymbol{r} \tag{2.15}$$

2.2.2 Spin-polarized systems

If an external magnetic field is applied to an electronic system, this will modify the charge density will be modified due to the electron and its spin interacting with the external magnetic field. This generally gives rise to a preferred spin orientation for the electrons, so such a system is referred to as a *spin-polarized system*. While the magnetization may generally vary in magnitude and direction from one point in space to another, it is reduced to a scalar field in the case of collinear magnetization. Then, the magnetization varies only along one direction. The two relevant scalar fields read

$$\rho(\boldsymbol{r}) = \rho_\uparrow(\boldsymbol{r}) + \rho_\downarrow(\boldsymbol{r}) \tag{2.16}$$

$$m(\boldsymbol{r}) = \rho_\uparrow(\boldsymbol{r}) - \rho_\downarrow(\boldsymbol{r}) \tag{2.17}$$

where $\rho_\uparrow(\boldsymbol{r})$ and $\rho_\downarrow(\boldsymbol{r})$ denote spin-up and spin-down electron densities, respectively. It is in this magnetic case the *generalized Hohenberg-Kohn theorem* that postulates a ground state energy. This energy is acquired by invoking the variational principle on an energy functional which now depends on the spin densities in (2.16) and (2.17) [32]

$$E = E[\rho_\uparrow, \rho_\downarrow] \tag{2.18}$$

The energy functional is segmented into different energy contributions, analogous to the decomposition made in (2.7), and invoke the variational principle to obtain the Kohn-Sham orbitals for the spin-polarized case

$$V^{KS}\phi_{i\boldsymbol{\sigma}}(\boldsymbol{r}) = \big[T + V_{ei}(\boldsymbol{r}) + V_H(\boldsymbol{r}) + V_{xc,\boldsymbol{\sigma}}(\boldsymbol{r})\big]\phi_{i\boldsymbol{\sigma}}(\boldsymbol{r}) = \epsilon_{i\boldsymbol{\sigma}}\phi_{i\boldsymbol{\sigma}}(\boldsymbol{r}) \tag{2.19}$$

$$\rho_\sigma(\boldsymbol{r}) = \sum_i^N \phi_{i\sigma}(\boldsymbol{r})\phi^*_{i\sigma}(\boldsymbol{r}) \tag{2.20}$$

A new index $\boldsymbol{\sigma}$ corresponding to spin $\uparrow$ and $\downarrow$ has been introduced. Except for the exchange-correlation potential, given by

$$V_{xc,\boldsymbol{\sigma}}(\boldsymbol{r}) = \frac{\delta E_{xc}[\rho_\uparrow, \rho_\downarrow]}{\delta \rho_\sigma(\boldsymbol{r})} \tag{2.21}$$

all other energy terms remain as in (2.11). As seen from above, in the spin-polarized case there are two spin electron densities instead of one, yielding two sets of Kohn-Sham equations.

2.2.3 L(S)DA+U

Since *Local (spin) density approximation* (L(S)DA) assumes local exchange-correlation, it does not properly capture the contribution from strongly correlated electron states. L(S)DA+U is an attempt to better model these strongly correlated states, typically f and d orbitals, using the Hubbard model [33, 34]. The modified energy functional in L(S)DA+U is given by

$$E_{LDA+U}[\rho(\boldsymbol{r})] = E_{LDA}[\rho(\boldsymbol{r})] + E_{Hub} - E_{dc} \tag{2.22}$$

E_{LDA} is the original energy functional from (2.7) and E_{hub} is the contribution to the energy functional from strongly correlated electron states through the Hubbard model. Since E_{LDA} already takes the local exchange-correlation into account, a third term E_{dc} is added to correct for the double counting. E_{Hub} is given by

$$E_{Hub}[\{n_m^{I\sigma}, n_{m'}^{I\sigma'}\}] = \frac{U^I}{2} \sum_{m,\sigma \neq m'\sigma'} n_m^{I\sigma} n_{m'}^{I\sigma'} \tag{2.23}$$

where $n_m^{I\sigma}$ represents the occupation number characterized by atomic site I, spin σ and z-component angular quantum number m, the latter corresponding to eigenvalues of operator $\hat{L}_z$ for a given orbital angular momentum number l. E_{dc} is not uniquely defined as there are more ways of making the double-counting correction. Of the different schemes available, the two most popular choices are the *Around mean-field* (AMF) and *Fully localized limit* (FLL) [35, 36].

The L(S)DA is an approximate model for the true exchange-correlation potential. Since the energy functional is only approximately modeled, the ground state energy and its corresponding orbitals will not be the true ground state of our system. The KS ground state energy of this approximate energy functional may be higher or lower than the real system, but a sufficiently good approximation for the energy functional yields a ground state closely resembling the true ground state.

2.2.4 Self-consistent cycle & the secular equation

While (2.19) and (2.20) provide a recipe for the ground state density and thereby the total ground state energy of the system, the KS equations form a self-consistent set of equations: In order to compute the KS potential in (2.19), the electron density is needed as input for the Hartree and exchange-correlation potentials. At the same time, (2.19) are solved for the orbitals on the RHS of (2.20). The KS equations are solved in a *Self-consistent field* (SCF) cycle by making an initial guess for the density, and then solve the KS equations for a new electron density repeatedly until convergence. To capitalize on information from previous iterations in order to accelerate the convergence, it is possible to use a mixing scheme for ρ^{out} and ρ^{in}. The perhaps simplest mixing scheme is $\rho_{in}^{i+1} = (1-\alpha)\rho_{in}^{i} + \alpha\rho_{out}^{i}$ for α between 0 and 1. A commonly used mixing scheme in self-consistent calculations is called Broyden's method [37]. Figure 2.1 illustrates the self-consistent cycle.

Let the wavefunction be expressed in terms of a basis set

$$\phi_\mu(\boldsymbol{r}) = \sum_\alpha c_{\mu\alpha}\phi_\alpha(\boldsymbol{r}) \tag{2.24}$$

Again, $\mu = \{n, \boldsymbol{\sigma}, \boldsymbol{k}\}$ for band index, spin and wavevector, respectively. $c_{\mu\alpha}$ are the expansion coefficients, and $\phi_\alpha(\boldsymbol{r})$ are the basis functions. Also let $\langle\phi_\alpha|\phi_\beta\rangle = S_{\alpha\beta}$. Inserting (2.24) into (2.20) and moving everything to the LHS yields an equation

$$\sum_\alpha [V^{KS}\,|\phi_\alpha(\boldsymbol{r})\rangle - \epsilon_n\,|\phi_\alpha(\boldsymbol{r})\rangle]c_{\mu\alpha} = 0 \tag{2.25}$$

Operating with $\langle\phi_\alpha(\boldsymbol{r})|$ from the left yields

$$\sum_\alpha [\langle\phi_\beta(\boldsymbol{r})|\,V^{KS}\,|\phi_\alpha(\boldsymbol{r})\rangle - \epsilon_n\,\langle\phi_\beta(\boldsymbol{r})|\phi_\alpha(\boldsymbol{r})\rangle]c_{\mu\alpha} = 0 \tag{2.26}$$

Now let $V_{\alpha\beta}^{KS} = \langle\phi_\beta(\boldsymbol{r})|\,V^{KS}\,|\phi_\alpha(\boldsymbol{r})\rangle$. This yields the so-called secular equation

$$[\boldsymbol{V}^{KS} - \epsilon_n \boldsymbol{S}]\boldsymbol{c}_\mu = 0 \tag{2.27}$$

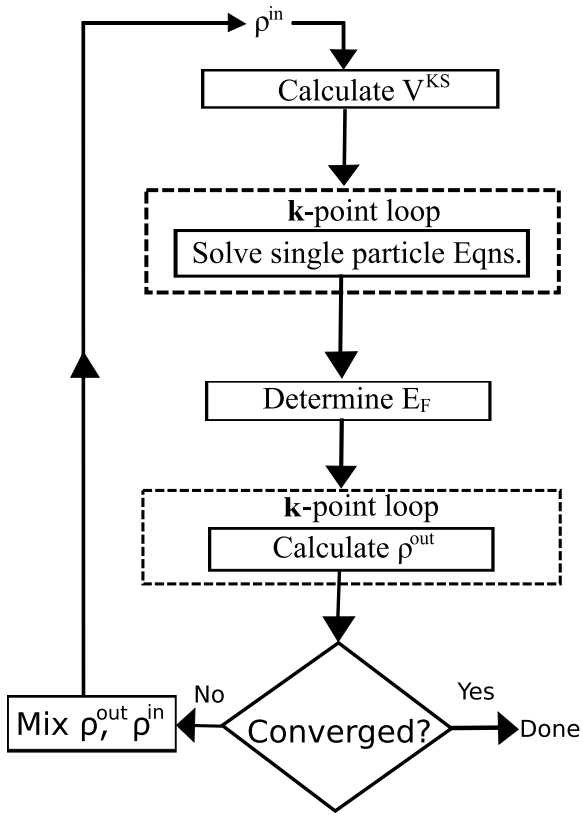

Figure 2.1: *Schematic chart for density functional theory calculations. An initial guess for ρ^{in} is used to compute the Kohn-Sham potential V^{KS}. Once the new orbitals have been solved for, the Fermi energy is determined to identify occupied orbitals. These make up ρ^{out}. A mixture of ρ^{out} and ρ^{in} is finally used as the new electron density in the next iteration. This process is repeated until the electron density ρ^{out} converges. This figure is largely based on one presented in Singh (2006) [38].*

where $\boldsymbol{V}^{KS}$ and $\boldsymbol{S}$ are matrices of rank equal to n_b, n_b denoting the number of basis functions. (2.27) is solved at each $\boldsymbol{k}$-point using standard linear algebra routines for every iteration in the self-consistent loop [39].

By cutting off the basis set at a finite number, we risk not being able to fully express the true KS orbitals. Minimizing $\{c_{\mu\alpha}\}$ with respect to the energy functional yields the exact KS ground state orbitals only when the basis set is capable of expressing the KS orbitals exactly. In practicality, a finite basis set, only approximately expressing the true KS orbitals, is sufficient.

2.3 Full potential Augmented plane-wave method

The Full potential Augmented plane-wave method is a popular method in the context of electronic structure calculations of crystals. The method is a procedure for solving the Kohn-Sham equations for the total energy, ground state density, eigenfunctions and eigenvalues of a many-electron system. Solving the Kohn-Sham equations is the main computational task in density functional theory [40]. The APW basis has been adapted specifically for electronic structure calculations in the context of crystals.

Starting with the original method to convey the basic idea behind the Augmented plane-wave method, the Linearized augmented plane-wave and Augmented plane-wave + local orbitals methods are presented. Finally, aspects of the APW method, relevant for the wavefunction overlap factor, are discussed.

2.3.1 The original APW method

All *Augmented plane-wave* (APW) methods are based on partitioning the unit cell into two regions: in region I, inside spheres centered around each basis atom, solutions to the spherically symmetric Schrödinger equation are employed. Since region I is near the nuclei, the potential is expected to resemble a spherically symmetric potential. In the interstitial region, region II, plane-waves are used. These solve Schrödinger's equation in a constant potential. See figure 3.4 for the partitioning of the unit cell. Region I is given in grey; region II is given in red.

In the APW method, the basis set is defined as

$$\psi^{APW}_{\mu \boldsymbol{G}}(\boldsymbol{r}) = \begin{cases} \sum_L a^{\beta}_{\mu,L,\boldsymbol{G}} u_l(r_\beta, E) Y_L(\hat{\boldsymbol{r}}_\beta) & \text{region I, } \beta \\ \frac{1}{\sqrt{V}} e^{i(\boldsymbol{k}+\boldsymbol{G})\cdot\boldsymbol{r}} & \text{region II} \end{cases} \tag{2.28}$$

where $\mu = \{n, \boldsymbol{\sigma}, \boldsymbol{k}\}$. $L = \{l, m\}$, standing for angular momentum quantum number and magnetic quantum number, respectively. $Y_L(\hat{\boldsymbol{r}})$ denote the Spherical harmonics and $u_l(r, E_l)$, if multiplied by the radius r, represent the radial solutions to Schrödinger's equation in a spherical potential. V is the unit cell volume. At the boundary between the two regions, the plane-wave is re-expressed using Bessel functions. This determines the coefficients

$$a^{\beta}_{\mu,L,\boldsymbol{G}} = 4\pi i^l Y^*_L(\hat{\boldsymbol{k}}_{\boldsymbol{G}}) \frac{j_l(|\boldsymbol{k}+\boldsymbol{G}|R_\beta)}{u_l(R_\beta, E)} \tag{2.29}$$

where $\boldsymbol{k}_{\boldsymbol{G}} = \boldsymbol{k} + \boldsymbol{G}$, j_l is the Bessel function and R_β is the radius of region I sphere β. The total wavefunction is then expanded in this basis set

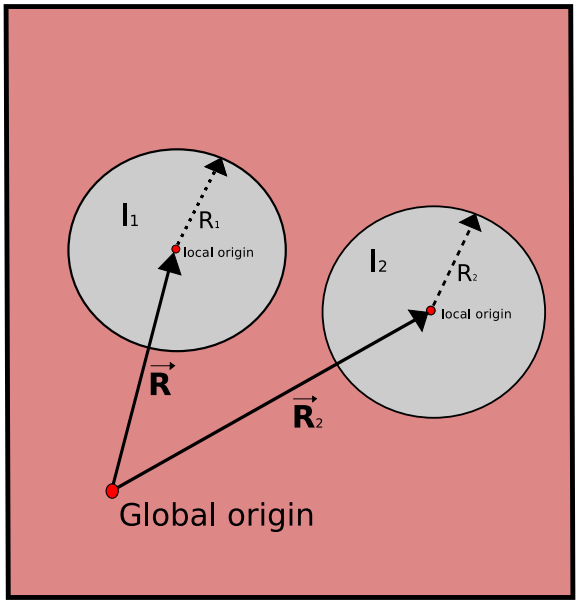

Figure 2.2: *Partitioning of the unit cell into two regions: atomic spheres centered around atomic sites at $\boldsymbol{R}_\beta$ in region I, and an interstitial region referred to as region II. The global origin is given as a red dot in region II. There may generally be several spheres making up region I, each sphere corresponding to an atom in the unit cell. Centered inside each sphere, a local origin is shown in red, and defines a new coordinate $\boldsymbol{r}_\beta$. The radius of sphere β is denoted R_β. The global origin is related to $\boldsymbol{r}_\beta$ through $\boldsymbol{r}_\beta = \boldsymbol{r} - \boldsymbol{R}_\beta$.*

$$\psi_\mu^{APW}(\boldsymbol{r}) = \sum_{\boldsymbol{G}} C_\mu(\boldsymbol{G}) \psi_{\mu\boldsymbol{G}}^{APW}(\boldsymbol{r}) \tag{2.30}$$

Since the radial functions of region I depend on energy, they must be picked inside a small energy window of interest in order to describe the wavefunction effectively. A new set of radial functions must be used in another energy window. This makes the APW method a very time-consuming method as a new basis function set must be constructed for each small energy window of interest.

It is also possible to carry out the summation over reciprocal lattice vectors in region I to obtain a new set of coefficients

$$A_{\mu,L}^\beta = \sum_{\boldsymbol{G}} a_{\mu,L,\boldsymbol{G}}^\beta \tag{2.31}$$

in which case the wavefunction reads

$$\psi_{\mu}^{APW}(\boldsymbol{r}) = \begin{cases} \sum_L A_{\mu,L}^{\beta} u_l(r_\beta, E) Y_L(\hat{\boldsymbol{r}}_\beta) & \text{region I, } \beta \\ \frac{1}{\sqrt{V}} \sum_{\boldsymbol{G}} C_\mu(\boldsymbol{G}) e^{i(\boldsymbol{k}+\boldsymbol{G})\cdot\boldsymbol{r}} & \text{region II} \end{cases} \tag{2.32}$$

2.3.2 LAPW

To overcome the issue of the basis functions being energy-dependent, a linearization energy E_l is introduced. This linearization energy is typically in the middle of the energy domain of interest. Having restricted the basis set dramatically, an additional term proportional to $\dot{u}_l(r, E_l)$ is included in this new basis set to add extra flexibility.

$$\psi_{\mu\boldsymbol{G}}^{LAPW}(\boldsymbol{r}) = \begin{cases} \sum_L R_{L,\mu,\boldsymbol{G}}^{LAPW,\beta}(r_\beta) Y_L(\hat{\boldsymbol{r}}_\beta) & \text{region I, } \beta \\ \frac{1}{\sqrt{V}} e^{i(\boldsymbol{k}+\boldsymbol{G})\cdot\boldsymbol{r}} & \text{region II} \end{cases} \tag{2.33}$$

where $R_{L,\mu,\boldsymbol{G}}^{LAPW,\beta}(r_\beta) = a_{L,\mu,\boldsymbol{G}}^{\beta} u_l(r_\beta, E_l) + b_{L,\mu,\boldsymbol{G}}^{\beta} \dot{u}_l(r_\beta, E_l)$. The expansion coefficients $a_{L,\boldsymbol{G},\mu}^{\beta}$ and $b_{L,\boldsymbol{G},\mu}^{\beta}$ are continuously differentiable at the sphere boundary. The wavefunction is given by

$$\psi_{\mu}^{LAPW}(\boldsymbol{r}) = \sum_{\boldsymbol{G}} C_\mu(\boldsymbol{G}) \psi_{\mu\boldsymbol{G}}^{LAPW}(\boldsymbol{r}) \tag{2.34}$$

Although the introduction of a linearized energy greatly simplifies the basis construction, it has a disadvantage, revealed in the case of localized states for which $\frac{\dot{u}_l}{u_l}\big|_{R_\beta}$ is generally very large. Due to the constraint of continuous differentiability, the region II basis-function must be matched with $\frac{\dot{u}_l}{u_l}\big|_{R_\beta}$. For a linear combination of plane-waves, the maximum value of this fraction is $|\boldsymbol{G}_{max}|$, max denoting the cut-off reciprocal lattice vector. Whereas the LAPW method simplifies the evaluation of different energies, it requires a larger number of plane-waves to satisfy continuous differentiability on sphere boundaries.

As with the APW method, a slightly alternative representation is given by carrying out the summation over reciprocal lattice vectors

$$\begin{aligned} \sum_{\boldsymbol{G}} a_{L,\mu,\boldsymbol{G}}^{\beta} &\equiv A_{L,\mu}^{\beta} \\ \sum_{\boldsymbol{G}} b_{L,\mu,\boldsymbol{G}}^{\beta} &\equiv B_{L,\mu}^{\beta} \end{aligned} \tag{2.35}$$

where in the above, the summation has been carried out over region I. The wavefunction is then expressed as

$$\psi_{\mu}^{LAPW}(\boldsymbol{r}) = \begin{cases} \sum_L [A_{L,\mu}^{\beta} u_l(r_\beta, E_l) + B_{L,\mu}^{\beta} \dot{u}_l(r_\beta, E_l)] Y_L(\hat{\boldsymbol{r}}_\beta) & \text{region I, } \beta \\ \frac{1}{\sqrt{V}} \sum_{\boldsymbol{G}} C_\mu(\boldsymbol{G}) e^{i(\boldsymbol{k}+\boldsymbol{G})\cdot\boldsymbol{r}} & \text{region II} \end{cases} \tag{2.36}$$

2.3.3 APW+lo

Sjöstedt et al. introduces a third APW method [41]. This method has an energy-independent basis set, but it at the same time overcomes the high cut-off issue in LAPW. Starting with the original APW method, one adds local orbitals for $l \leq 3$. The orbitals are local in the sense that they are confined to the region I spheres, hence not affecting the number of plane-waves in the interstitial region. The local orbitals are given by

$$\phi_{L,n,\boldsymbol{\sigma}}^{lo}(\boldsymbol{r}) = \begin{cases} R_{L,n,\boldsymbol{\sigma}}^{lo,\beta}(r_\beta) Y_L(\hat{\boldsymbol{r}}_\beta) & \text{region I, } \beta \\ 0 & \text{region II} \end{cases} \tag{2.37}$$

with $R_{L,n,\boldsymbol{\sigma}}^{lo,\beta}(r_\beta) = a_{L,n\boldsymbol{\sigma}}^{lo,\beta} u_l(r_\beta, E_l) + b_{L,n\boldsymbol{\sigma}}^{lo,\beta} \dot{u}_l(r_\beta, E_l)$.

The crucial difference between LAPW and APW+lo are boundary conditions. Whereas continuous differentiable basis functions are demanded in LAPW, the APW+lo basis functions are allowed to be discontinuous differentiable at the sphere boundary. The relaxation of this condition in the APW+lo method permits a plane-wave cut-off $|\boldsymbol{G}_{max}|$ independent of the local orbitals in region I. Since the local orbitals are confined to region I, one sets $a_{L,n\boldsymbol{\sigma}}^{lo,\beta} = 1$ and determines $b_{L,n\boldsymbol{\sigma}}^{lo,\beta}$ by demanding the local orbital to disappear at the sphere boundary: $\phi_{L,n,\boldsymbol{\sigma}}^{lo}(R_\beta) = 0$.

APW+lo basis functions are set up faster than in LAPW. A majority of the basis functions include only terms proportional to $u_l(r)$; in LAPW, both $u_l(r)$ and $\dot{u}_l(r)$ terms are included for all basis functions. In fact, Madsen et al. (2001) have shown that compared to the LAPW method, the APW+lo scheme converges at a much lower cost to essentially the same results [42].

2.3.4 Kinetic energy operator

Having introduced the possibility of kinks on the basis functions at the sphere boundary, the kinetic energy operator must be treated carefully. There are two expressions for the kinetic energy operator: $\int_V \chi_{\boldsymbol{G}}^*(-\nabla^2)\chi_{\boldsymbol{G}'} dV$ which is the Laplacian operator formulation, and $\int_V \chi_{\boldsymbol{G}}^*(-\nabla^2)\chi_{\boldsymbol{G}'} dV$ which is the nabla operator formulation. It has been argued that the second formulation is more fundamental as it enters in the variational principle [43]. As may be shown using Green's theorem, the two representations differ by a term

$$\oint_S \chi^*_{\boldsymbol{G}}\left(\frac{\partial \chi^I_{\boldsymbol{G'}}}{\partial r} - \frac{\partial \chi^{II}_{\boldsymbol{G'}}}{\partial r}\right) d\boldsymbol{S} \tag{2.38}$$

In the case of LAPW, this term vanished due to smooth basis functions, and both formulations may be used without taking (2.38) into account. For APW+lo however, this extra term must be added to the kinetic energy operator whenever the Laplacian energy operator formalism is used.

2.3.5 Lattices with inversion symmetry

To deal with lattices with inversion symmetry, a final modification is made to the basis set. First, the origin is chosen at an inversion center to ensure the secular equation is real [38]. Second, one demands that the local orbitals form linear combinations transforming like plane-waves. This is achieved by attaching a fictitious plane-wave to each local orbital through a Bessel expansion, as done in (2.29) in the discussion on the APW method. The plane-wave is fictitious in the sense that the local orbitals are completely confined to the region I spheres and do not extend to region II. For N local orbitals, one must use N fictitious plane-waves, the plane-wave set $\{\boldsymbol{G}_{lo}\}$ chosen such that the basis functions are linearly independent. This yields

$$e^{i\boldsymbol{G}_{lo}\cdot\boldsymbol{r}} = e^{i\boldsymbol{G}_{lo}\cdot\boldsymbol{R}_\beta} \sum_L i^l j_l(|\boldsymbol{G}||\boldsymbol{R}_\beta|) Y^*_L(\hat{\boldsymbol{G}}) Y_L(\hat{r}_\beta) \tag{2.39}$$

where $L = \{l, m\}$. (2.39) is matched with the local orbital expression $\phi^{lo}_{L,n\boldsymbol{\sigma}}(\boldsymbol{r}_\beta) = R^{lo,\beta}_{L,n,\boldsymbol{\sigma}}(r_\beta) Y_L(\hat{\boldsymbol{r}}_\beta)$ from (2.37). In other words, instead of setting $a^{lo,\beta}_{L,n\boldsymbol{\sigma}} = 1$ and determining $b^{lo,\beta}_{L,n\boldsymbol{\sigma}}$ as in Chapter 2.3.3, one determines the local orbital coefficients by invoking the matching conditions above. Once $a^{lo,\beta}_{L,n\boldsymbol{\sigma}}$ and $b^{lo,\beta}_{L,n\boldsymbol{\sigma}}$ have been determined, the wavefunction reads

$$\begin{aligned}\psi_\mu = &\sum_L \Big(\sum_{\boldsymbol{G}} c_{\boldsymbol{G}} [A^\beta_{L,\mu}(\boldsymbol{G}) u_l(r) + B^\beta_{L,\mu}(\boldsymbol{G}) \dot{u}_l(r)] Y_L(\hat{\boldsymbol{r}}) \\ &+ \sum_{lo} c_{lo} [A^\beta_{L,n\boldsymbol{\sigma}}(lo) u_l(r) + B^\beta_{L,n\boldsymbol{\sigma}}(lo) \dot{u}_l(r)] Y_L(\hat{\boldsymbol{r}}) e^{i\boldsymbol{G}_{lo}\cdot\boldsymbol{R}_\beta} \Big)\end{aligned} \tag{2.40}$$

with $c_{\boldsymbol{G}}$ and c_{lo} being associated with their respective reciprocal lattice vectors $\boldsymbol{G}$ and $\boldsymbol{G}_{lo}$. As earlier, $\mu = \{n, \boldsymbol{\sigma}, \boldsymbol{k}\}$. The phase shift present for (2.40), along with the lo coefficients, ensure the local orbitals transform like plane-waves. Finally interchanging the summation over L with the summation over lo and $\boldsymbol{G}$, yields a new set of expansion coefficients

$$\psi_\mu = \sum_L a^\beta_{L,\mu} u_l(r) + b^\beta_{L,\mu} \dot{u}_l(r)] Y_L(\hat{\boldsymbol{r}}) \tag{2.41}$$

where the new coefficients are given by

$$\begin{aligned} a^{\beta}_{L,\mu} &= \sum_{\boldsymbol{G}} A^{\beta}_{L,\mu}(\boldsymbol{G}) + \sum_{lo} c(lo) B^{\beta}_{L,n\boldsymbol{\sigma}}(lo) \\ b^{\beta}_{L,\mu} &= \sum_{\boldsymbol{G}} A^{\beta}_{L,\mu}(\boldsymbol{G}) + \sum_{lo} c(lo) B^{\beta}_{L,n,\boldsymbol{\sigma}}(lo) \end{aligned} \tag{2.42}$$

2.3.6 Potential expansion

The potential for both schemes is expanded according to

$$V(\boldsymbol{r}) = \begin{cases} \sum_L V_L(r) Y_L(\hat{\boldsymbol{r}}) & \text{region I} \\ \sum_{\boldsymbol{K}} V_{\boldsymbol{K}}(r) e^{i\boldsymbol{K}\cdot\boldsymbol{r}} & \text{region II} \end{cases} \tag{2.43}$$

where $\boldsymbol{K}$ denotes a reciprocal lattice vector, Y_L again corresponds to spherical harmonics and $L = \{l, m\}$.

2.3.7 Dirac equation & the Scalar Relativistic approximation

Relativistic effects play a significant role in semiconductor transport, and must be incorporated into the (L)APW(+lo) basis set. In the study of semiconductor transport behaviour, the energy bands of interest are usually low in energy, so in the interstitial region, electrons are treated sufficiently well non-relativistically. On the other hand, electrons that are closer to a particular nucleus are subject to much larger negative potentials. Therefore, relativistic effects are taken into account in region I. The core electrons, those confined to the atomic spheres, are treated fully-relativistically by solving the Dirac equation for a spherically symmetric potential. Valence electrons in region I are treated in the *Scalar relativistic approximation* (SRA) [44]. The valence electrons are in transport phenomena of particular interest since these participate the most actively in charge transport.

To obtain a description consistent with the theory of special relativity, one starts with the Dirac equation. Consider an electron moving in the field of a stationary nucleus producing a central field $V_{nuc}(r)$. To an approximation, other electrons altogether will also contribute with a central field $V_{MF}(r)$. The electron will then satisfy the one-electron Dirac equation

$$H_D \Phi = \{c\boldsymbol{\alpha} \cdot \boldsymbol{p} + \beta m_e c^2 + V(r)\}\Phi = \epsilon\Phi \tag{2.44}$$

where H_D has 4 x 4 components and Ψ is four-dimensional. $V(r) = V_{nuc}(r) + V_{MF}(r)$, $\boldsymbol{p}$ is the momentum operator and m_e the electron mass. c denotes the speed of light. A comparison with the non-relativistic energy is made after subtracting the restmass: $E = \epsilon - mc^2$. The elements of $\boldsymbol{\alpha}$ are given by

$$\alpha_k = \begin{bmatrix} 0 & \sigma_k \\ \sigma_k & 0 \end{bmatrix} \tag{2.45}$$

with σ_k being the Pauli matrices

$$\sigma_1 = \begin{bmatrix} 0 & 1 \\ 1 & 0 \end{bmatrix}, \quad \sigma_2 = \begin{bmatrix} 0 & -i \\ i & 0 \end{bmatrix}, \quad \sigma_3 = \begin{bmatrix} 1 & 0 \\ 0 & -1 \end{bmatrix} \tag{2.46}$$

β represents

$$\beta = \begin{bmatrix} \mathbf{1} & \mathbf{0} \\ \mathbf{0} & -\mathbf{1} \end{bmatrix} \tag{2.47}$$

where $\mathbf{1}$ represents the 2 x 2 identity matrix, and $\mathbf{0}$ the 2 x 2 zero matrix. The Dirac equation differs with Schrödinger's in that orbital angular momentum and spin do not commute with the Dirac Hamiltonian. Instead, now $\hat{J}^2$ and $\hat{J}_z$, where $\boldsymbol{J} = \boldsymbol{L} + \boldsymbol{S}$ is the total angular momentum, have eigenstates in common with the Dirac hamiltonian. To construct these eigenstates, one combines the familiar spherical harmonics $Y_L(\theta, \phi)$ which are eigenstates of operators $\hat{L}^2$ and $\hat{L}_z$, with a two-component spinor x_σ, which is an eigenstate of $\hat{S}^2$ and $\hat{S}_z$, to form eigenstates of $\hat{J}^2$ and $\hat{J}_z$. Using the Clebsch-Gordan coefficients, one gets

$$\chi_{jlm}(\theta, \phi) = \sum_{\sigma=\pm\frac{1}{2}} C(l, 1/2, j; m-\sigma, \sigma, m) Y_{lm-\sigma}(\theta, \phi) x_\sigma \tag{2.48}$$

where $C(j_1, j_2, j_3; m_1, m_2, m_3)$ are the Clebsch-Gordan coefficients and x_σ for $\sigma = \pm\frac{1}{2}$ reads

$$x_{\frac{1}{2}} = \begin{bmatrix} 1 \\ 0 \end{bmatrix}, \quad x_{-\frac{1}{2}} = \begin{bmatrix} 0 \\ 1 \end{bmatrix} \tag{2.49}$$

The quantum numbers $\{j, l, m\}$ are not independent since $j = l \pm \frac{1}{2}$. It is therefore expedient to introduce the operator $\hat{K} = -1 - \boldsymbol{\sigma} \cdot \boldsymbol{L}$. $\hat{K}$ has eigenvalues $\kappa = \pm(j + \frac{1}{2})$ for $j = l \pm \frac{1}{2}$. Since κ determines both j and l, one may now use a more compact notation of $\{\kappa, m\}$, and the relativistic equivalent to the Spherical harmonics is $\chi_{\kappa m}$. A solution to Dirac's equation now reads

$$\Phi_{\kappa m} = \begin{bmatrix} g_\kappa(r)\chi_{\kappa m} \\ -i\sigma_r f_\kappa(r)\chi_{\kappa m} \end{bmatrix} \tag{2.50}$$

Each element in equation (2.50) consists of a time-independent spatial function and the two-component spinor constructed in (2.48), corresponding to the spatial as well as the

1/2 spin degrees of freedom. σ_r is given by $\sigma_r = \boldsymbol{\sigma} \cdot \hat{\boldsymbol{r}}$. (2.50) is a solution to (2.44) as long as the radial components f_κ and g_κ satisfy the two coupled radial equations

$$\frac{df_\kappa}{dr} = \frac{1}{c}\big(V - E\big)g_\kappa + \left(\frac{\kappa - 1}{r}\right)f_\kappa \tag{2.51}$$

$$\frac{dg_\kappa}{dr} = -\left(\frac{\kappa + 1}{r}\right)g_\kappa + 2Mcf_\kappa \tag{2.52}$$

with $M \equiv m_e + \frac{1}{2c^2}\big(E - V\big)$ and $E = \epsilon - m_e c^2$. (2.51) and (2.52) may be decoupled by first solving (2.52) for f_κ and substituting the result into (2.51). This yields

$$\begin{aligned}\left(-\frac{1}{2M}\right)\left[\frac{d^2 g_\kappa}{dr^2} + \frac{2}{r}\frac{dg_\kappa}{dr} - \frac{l(l+1)}{r^2}g_\kappa\right] \\ - \frac{dV}{dr}\frac{dg_\kappa}{dr}\frac{1}{4M^2c^2} + Vg_\kappa - \frac{\kappa + 1}{r}\frac{dV}{dr}\frac{g_\kappa}{4M^2c^2} = Eg_\kappa\end{aligned} \tag{2.53}$$

The first bracket on the LHS gives rise to the so-called Mass-velocity effect, and the subsequent term is denoted the Darwin term. Only the last term on the LHS depends explicitly on the sign of κ; this is the *Spin-orbit coupling* (SOC) term. Including this term, the eigenfunctions in (2.50) will not be eigenstates of spin σ. In the Scalar Relativistic approximation, this last term is omitted, allowing one to maintain orbital angular momentum l and spin σ as good quantum numbers. We write $\bar{f}$ and $\bar{g}$ to emphasize that the radial functions are solutions only in the Scalar relativistic approximation. Introducing

$$\phi_l \equiv \frac{1}{2Mc}\frac{d\bar{g}_l}{dr} \tag{2.54}$$

(2.53) is written as

$$\frac{d\phi_l}{dr} = -\frac{2}{r}\phi_l + \left[\frac{l(l+1)}{2Mcr^2} + \frac{1}{c}\big(V - E\big)\right]\bar{g}_l \tag{2.55}$$

Here, $\{\kappa, m\}$ has been replaced by $\{l, m, \sigma\}$, permissible since the SOC term has been dropped. (2.50) may now be written as

$$\Phi_{L\sigma} = \begin{bmatrix} \bar{g}_l Y_L x_\sigma \\ \frac{i\sigma_r}{2Mc}\big(-\frac{d\bar{g}_l}{dr} + \frac{1}{r}\bar{g}_l \boldsymbol{\sigma}\cdot\boldsymbol{L}\big)Y_L x_\sigma \end{bmatrix} \tag{2.56}$$

where again $L = \{l, m\}$. The relativistic spinor has been replaced by a spherical harmonic Y_L multiplied with a non-relativistic two-component spinor x_σ. $\bar{g}_l Y_L x_\sigma$ is referred to as the large component, the lower element is referred to as the small component. Finally, to achieve a more suitable expression for numerical solution methods, $P_l = r\bar{g}_l$ and $Q_l = rc\phi_l$ are introduced. (2.57) is now written as

$$\Phi_{L\sigma} = \frac{1}{r}\begin{bmatrix} P_l Y_L x_\sigma \\ i\sigma_r\big(-Q_l + \frac{P_l}{2Mcr}\boldsymbol{\sigma}\cdot\boldsymbol{L}\big)Y_L x_\sigma \end{bmatrix} \tag{2.57}$$

and (2.51) and (2.52) as

$$\frac{dP_l}{dr} = 2MQ_l + \frac{1}{r}P_l \tag{2.58}$$

$$\frac{dQ_l}{dr} = -\frac{1}{r}Q_l + \left[\frac{l(l+1)}{2Mr^2} + (V - E_l)\right]P_l \tag{2.59}$$

where a particular linearization energy E_l is assumed. These equations may be solved in the same way one would numerically solve the non-relativistic Schrödinger equation as long as the following boundary condition is met [38]

$$\lim_{r\to 0}\frac{Q}{P} = c\frac{[l(l+1)+1-(2Z/c)^2]^{1/2}-1}{(2Z/c)} \tag{2.60}$$

We also include an expression for the energy derivative of (2.58) and (2.59) since this is needed in the linearization. Let $\dot{P}_l \equiv \frac{dP_l}{dE}|_{E_l}$ and equivalently for $\dot{Q}_l$. Write

$$\dot{P}_l' = 2(\dot{M}Q_l + M\dot{Q}_l) + \frac{1}{r}\dot{P}_l \tag{2.61}$$

$$\dot{Q}_l' = -\frac{1}{r}\dot{Q}_l + [\frac{l(l+1)}{2Mr^2} + (V - E_l)]\dot{P}_l - [\frac{l(l+1)}{2Mr^2} + 1]P_l \tag{2.62}$$

For future reference

$$\Phi_{L\sigma} = u_{l\sigma}Y_L \tag{2.63}$$

where

$$u_{l\sigma} = \begin{bmatrix} \bar{g}_l x_\sigma \\ \frac{i\sigma_r}{2Mc}\big(-\frac{d\bar{g}_l}{dr} + \frac{1}{r}\bar{g}_l\boldsymbol{\sigma}\cdot\boldsymbol{L}\big)x_\sigma \end{bmatrix} \tag{2.64}$$

The Scalar relativistic approximation in short amounts to including relativistic effects from the Mass-velocity term and Darwin term, but cast away the effect of Spin-orbit coupling. The Dirac equation furthermore gives rise to the large and small components of the radial wavefunction. Both must participate when evaluating matrix elements: instead of u^2, now $f^2 + g^2$ is normalized.

2.3.8 Including Spin-orbit coupling as a second variational step

In the scalar relativistic approximation, just presented, the spin-orbit coupling is neglected to decouple spin from angular momentum. Although the scalar relativistic approximation allows one to maintain spin number and angular momentum number as good quantum numbers, it fails to explain the near-band edge behavior of many semiconductors. Near the band edge, spin-orbit coupling effects must be taken into account. For the core states, a fully relativistic model, including spin-orbit coupling from the beginning, will be necessary. For valence states, it is often economical to include spin-orbit coupling as a second variational step, after having completed a scalar relativistic calculation first. Due to our interest in the valence states, paramount in transport phenomena, the second method is of particular interest, and will be presented here.

If we start with n basis functions in the scalar relativistic approximation, and include spin-orbit coupling as a second step, double the number of basis functions is needed in the spin-orbit calculations. This is due to a coupling between spin-up and spin-down basis functions, manifesting itself as nonzero matrix elements between spin-up and spin-down basis functions in the hamiltonian. At each $\boldsymbol{k}$-point, a $2n \times 2n$ secular equation must now be solved, requiring eight times more computational resources compared with SRA [38]. An alternative approach is to capitalize on spin-orbit coupling often being a small effect, and thereby include it as a second variational step. First solve the secular equation for n basis functions in the scalar relativistic approximation. After that, the hamiltonian, including spin-orbit terms, is diagonalized in the space of a selected low-lying bands obtained from the scalar relativistic calculations.

In the first variational step which excludes spin-orbit coupling, solutions to Dirac's equation (2.57) are used to construct wavefunctions within region I. Recall from Chapter 2.3.7 that these solutions are of the form

$$\Phi_{L\sigma} = \frac{1}{r}\begin{bmatrix} P_l Y_L x_\sigma \\ i\sigma_r\big(-Q_l + \frac{P_l}{2Mcr}\boldsymbol{\sigma}\cdot\boldsymbol{L}\big)Y_L x_\sigma \end{bmatrix} \tag{2.65}$$

These are not eigenfunctions of the Dirac hamiltonian in (2.44) since they were obtained in SRA. In order to define the spin-orbit operator, one nonetheless operates with the Dirac hamiltonian on the SRA wavefunctions, yielding

$$H_D\Phi_{L\sigma} = \epsilon\Phi_{L\sigma} + H_{so}\Phi_{L\sigma} \tag{2.66}$$

where H_{so} is given by

$$H_{so} = \frac{1}{(2Mc)^2}\frac{1}{r}\frac{dV}{dr}\begin{bmatrix} \boldsymbol{\sigma}\cdot\boldsymbol{L} & 0 \\ 0 & 0 \end{bmatrix} \tag{2.67}$$

The term $H_{so}\Phi_{L\sigma}$ is a measure of how much the SRA eigenfunctions deviate from the true eigenfunctions in (2.44). Notice that H_{so} acts only on the large component of the radial

wavefunction. Let the wavefunctions obtained in the first variational step be

$$\begin{aligned} &\Psi_{n\uparrow\boldsymbol{k}}, \quad E_{n\uparrow\boldsymbol{k}} \\ &\Psi_{n\downarrow\boldsymbol{k}}, \quad E_{n\downarrow\boldsymbol{k}} \end{aligned} \tag{2.68}$$

where $E_{n\uparrow\boldsymbol{k}}$ and $E_{n\downarrow\boldsymbol{k}}$ are the corresponding energies. These are, as mentioned above, a linear combination of (2.65). In the second variational step, one considers a new eigenproblem for the total hamiltonian H_D, including H_{so}, with a selected subset of (2.68) used as a new basis set. Often, this subset is significantly smaller than the set (2.68), resulting in a smaller secular equation. In addition, only the SOC matrix elements must be evaluated, since we in the first variational step already determined the SRA eigenenergies.

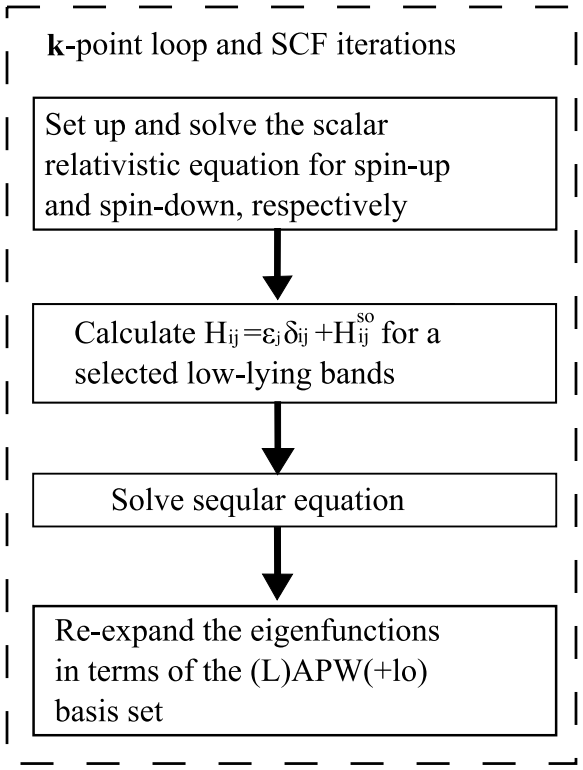

Figure 2.3: *Schematic chart for the first and second variational steps. First, the secular equation is solved in SRA for spin-up and spin-down basis functions, respectively. Next, a new hamiltonian including the SOC matrix elements is constructed for a selected subset of the original bands. A second secular equation is then solved, this time including SOC, yielding a new set of wavefunctions. This figure is largely based on one presented in Singh (2006) [38].*

For simplicity, the discussion on the spin-orbit matrix elements is restricted to the LAPW basis set

$$\psi_\mu = \sum_{\boldsymbol{G}} C_\mu(\boldsymbol{G})\psi_\mu^{\boldsymbol{G}} \tag{2.69}$$

The second variational treatment is restricted to region I of the unit cell. Inside the spheres of region I, the basis reads

$$\psi_\mu^{\boldsymbol{G}} = \sum_L \{a^\beta_{n\boldsymbol{k},L}(\boldsymbol{G})\Phi^\beta_{L\sigma} + b^\beta_{n\boldsymbol{k},L}(\boldsymbol{G})\dot{\Phi}^\beta_{L\sigma}\} \tag{2.70}$$

In the above, $\mu = \{n, \boldsymbol{k}, \sigma\}$ and $L = \{l, m\}$, as usual. The matrix element between $\psi_\mu^{\boldsymbol{G}}$ and $\psi_{\mu'}^{\boldsymbol{G'}}$ reads

$$\begin{aligned}\left\langle \psi_\mu^{\boldsymbol{G}} \right| H_{so} \left| \psi_{\mu'}^{\boldsymbol{G'}} \right\rangle = \sum_{L,L'} & a^{\beta *}_{n\boldsymbol{k}L} a^\beta_{n'\boldsymbol{k}'L'} \left\langle \Phi^\beta_{L\sigma} \right| H_{so} \left| \Phi^\beta_{L'\sigma'} \right\rangle \\ & + b^{\beta *}_{n\boldsymbol{k}L} a^\beta_{n'\boldsymbol{k}'L'} \left\langle \dot{\Phi}^\beta_{L\sigma} \right| H_{so} \left| \Phi^\beta_{L'\sigma'} \right\rangle \\ & + a^{\beta *}_{n\boldsymbol{k}L} b^\beta_{n'\boldsymbol{k}'L'} \left\langle \Phi^\beta_{L\sigma} \right| H_{so} \left| \dot{\Phi}^\beta_{L'\sigma'} \right\rangle \\ & + b^{\beta *}_{n\boldsymbol{k}L} b^\beta_{n'\boldsymbol{k}'L'} \left\langle \dot{\Phi}^\beta_{L\sigma} \right| H_{so} \left| \dot{\Phi}^\beta_{L'\sigma'} \right\rangle\end{aligned} \tag{2.71}$$

The $\left|\Phi^\beta_{L\sigma}\right\rangle$ and $\left|\dot{\Phi}^\beta_{L\sigma}\right\rangle$ are known on beforehand, so the overlaps on the LHS of (2.71) may be stored initially and reused rather than recalculated in every SCF iteration. Using (2.65) and (2.67), these elements are calculated. For example

$$\begin{aligned}&\left\langle \Phi^\beta_{L\sigma} \right| H_{so} \left| \Phi^\beta_{L'\sigma'} \right\rangle = \\ &\frac{1}{(2Mc)^2} \int_{r_\beta=0}^{R_\beta} dr_\beta \frac{P_l^* P_{l'}}{r_\beta} \frac{dV}{dr_\beta} \int_{\phi=0}^{2\pi} \int_{\theta=0}^{\pi} d\Omega Y_L^* x_\sigma^\dagger \boldsymbol{\sigma} \cdot \boldsymbol{L} Y_{L'} x_\sigma\end{aligned} \tag{2.72}$$

The summation over L and L' is greatly restricted since spin-orbit couples only for $l = l'$ and $|m - m'| \leq 1$ [38, 44]. Analogous expressions are easily obtained for the other three overlaps on the RHS of (2.71). Whether LAPW or APW+lo is used, $\left\langle \psi_\mu^{\boldsymbol{G}} \right| H_{so} \left| \psi_{\mu'}^{\boldsymbol{G'}} \right\rangle$ will take the form of a linear combination of the overlaps on the LHS of (2.71).

2.3.9 (L)APW(+lo)

We finally present a general expression which will be used to obtain scattering rates independent of which of the methods LAPW or APW+lo is used. By defining the expansion coefficients of this general expression appropriately, one is able to use the more general overlap expression obtained in Chapter 3 to the particular method used. This expression

also uses notation consistent with a relativistic treatment of the basis functions in region I. The general expression reads

$$\psi_{\mu\boldsymbol{G}}(\boldsymbol{r}) = \begin{cases} \sum_L R^{\beta}_{\mu,L}(\boldsymbol{G}, \boldsymbol{r}_\beta) & \text{region I} \\ \\ \frac{1}{\sqrt{V}} e^{i(\boldsymbol{k}+\boldsymbol{G})\cdot\boldsymbol{r}} & \text{region II} \end{cases} \tag{2.73}$$

with

$$\begin{aligned} &R^{\beta}_{\mu,L}(\boldsymbol{G}, \boldsymbol{r}_\beta) = \\ &a^{\beta}_{\mu,L}(\boldsymbol{G})\Phi^{\beta}_{1,L\sigma}(\boldsymbol{r}_\beta, E_{1,l}) + b^{\beta}_{\mu,L}(\boldsymbol{G})\dot{\Phi}^{\beta}_{1,L\sigma}(r_\beta, E_{1,l}) + c^{\beta}_{\mu,L}(\boldsymbol{G})\Phi^{\beta}_{2,L\sigma}(r_\beta, E_{2,l}) \end{aligned} \tag{2.74}$$

The total wavefunction reads

$$\psi_\mu(\boldsymbol{r}) = \sum_{\boldsymbol{G}} C_\mu(\boldsymbol{G})\psi_{\mu\boldsymbol{G}}(\boldsymbol{r}) \tag{2.75}$$

One may also use an equivalent representation, where the summation over $\boldsymbol{G}$ has been carried out, yielding a new set of basis coefficients for region I

$$\psi_\mu(\boldsymbol{r}) = \begin{cases} \sum_L R^{\beta}_{\mu,L}(\boldsymbol{r}) & \text{region I} \\ \\ \sum_{\boldsymbol{G}} \frac{1}{\sqrt{V}} \sum_{\boldsymbol{G}} C_\mu(\boldsymbol{G}) e^{i(\boldsymbol{k}+\boldsymbol{G})\cdot\boldsymbol{r}} & \text{region II} \end{cases} \tag{2.76}$$

where this time, there is no $\boldsymbol{G}$ dependence in region I

$$R^{\beta}_{\mu,L}(\boldsymbol{r}) = a^{\beta}_{\mu,L}\Phi^{\beta}_{1,L\sigma}(\boldsymbol{r}_\beta, E_{1,l}) + b^{\beta}_{\mu,L}\dot{\Phi}^{\beta}_{1,L\sigma}(\boldsymbol{r}_\beta, E_{1,l}) + c^{\beta}_{\mu,L}\Phi^{\beta}_{1L\sigma}(\boldsymbol{r}_\beta, E_{2,l}) \tag{2.77}$$

Here, $\Phi^{\beta}_{1,L\sigma}$, $\dot{\Phi}^{\beta}_{1,L\sigma}$ and $\Phi^{\beta}_{2,L\sigma}$ are 4-component wavefunctions given by (2.57). Again, $\mu = \{\boldsymbol{k}, n, \boldsymbol{\sigma}\}$. $E_{1,l}$ and $E_{2,l}$ denote linearization energies, and $L = \{l, m\}$, where l is orbital quantum number and m represents magnetic quantum number. Finally, the radius $r_\beta = |\boldsymbol{r} - \boldsymbol{R}_\beta|$ is defined according to the center of the sphere β.

2.4 Wannier functions

For the independent-particle approximation in a perfect crystal, electron states are conventionally described by Bloch waves labeled by a band index n and a wavevector $\boldsymbol{k}$. An

alternative representation in real space was introduced by Gregory Wannier in 1937 [45]. This localized orbital in a periodic structure description is now known as a Wannier representation. In the Wannier representation, each state is labeled by band index n and lattice vector $\boldsymbol{R}$, making it a real-space representation of the electron states.

2.4.1 Wannier transformation

According to Bloch's theorem, a common eigenstate of the one-electron Hamiltonian $\hat{\mathcal{H}}$ and the lattice translation operator $\hat{\mathcal{T}}_{\mathcal{R}}$ is given by

$$\psi_\mu(\boldsymbol{r}) = e^{i\phi_{n\boldsymbol{\sigma}}(\boldsymbol{r})} u_\mu(\boldsymbol{r}) e^{i\boldsymbol{k}\cdot\boldsymbol{r}} \tag{2.78}$$

where again $\mu = \{n, \boldsymbol{\sigma}, \boldsymbol{k}\}$. One demands that $u_\mu(\boldsymbol{r})$ has the periodicity of the real-space crystal lattice, and $e^{i\phi_{n\boldsymbol{\sigma}}(\boldsymbol{r})}$ the periodicity of the corresponding reciprocal lattice. The latter, typically not written out explicitly, is not assigned by Schrödinger's equation, and offers an arbitrary phase to the Bloch wavefunction. This makes the Bloch-state non-unique. As stated earlier, a real-space representation is more convenient in many applications, for instance when dealing with transport properties [14]. One finds such a representation by a Fourier transformation of the Bloch state into a Wannier state. The indeterminacy of the Bloch state represented by $e^{i\phi_{n\boldsymbol{\sigma}}(\boldsymbol{r})}$ propagates to the Wannier representation which also becomes non-unique. A Wannier representation of the Bloch state is given as

$$\omega_{n\boldsymbol{\sigma}}(\boldsymbol{r} - \boldsymbol{R}) = \omega_\gamma(\boldsymbol{r}) = \frac{V}{\left(2\pi\right)^3} \int_{BZ} \sum_{m=1}^{N} U_{mn}(\boldsymbol{k}) \psi_\mu e^{-i\boldsymbol{k}\cdot\boldsymbol{R}} d\boldsymbol{k} \tag{2.79}$$

where the label $\gamma = \{n, \boldsymbol{\sigma}, \boldsymbol{R}\}$. $\boldsymbol{R}$ denotes a lattice point and V the crystal volume. This time, $\mu = \{m, \boldsymbol{\sigma}, \boldsymbol{R}\}$. The phase factor $U_{mn}(\boldsymbol{k})$ represents the arbitrariness inherited from the Bloch-function phase factor $e^{i\phi_n(\boldsymbol{r})}$ resulting in the indeterminacy of the Wannier representation. The set $\{|\boldsymbol{R}n\rangle\}$ constitute an orthonormal basis and $|\boldsymbol{R}n\rangle$ is transformed into $|\boldsymbol{R'}n\rangle$ by a translation of the lattice vector $\boldsymbol{R'} - \boldsymbol{R}$ [14]. Finally, the inverse transformation, carrying one from the Wannier representation to Bloch, is given by

$$\psi_\mu(\boldsymbol{r}) = \sum_{\boldsymbol{R}} \sum_{m=1}^{N} U^\dagger_{nm}(\boldsymbol{k}) e^{i\boldsymbol{k}\cdot\boldsymbol{R}} \omega_\gamma(\boldsymbol{r}) \tag{2.80}$$

where $\mu = \{n, \boldsymbol{\sigma}, \boldsymbol{k}\}$ and $\gamma = \{m, \boldsymbol{\sigma}, \boldsymbol{R}\}$.

2.4.2 Maximally localized Wannier functions

The gauge freedom present in the Bloch state, and inherited by the Wannier representation, may be used to maximally localize the Wannier functions. This localization corresponds to

choosing a particular unitary matrix $U_{mn}(\boldsymbol{k})$ in (2.79). In order to carry out this procedure, one first introduces a well-defined localization-criterion

$$\Omega = \sum_n \left[\langle \mathbf{0}n | \, \boldsymbol{r}^2 \, | \mathbf{0}n \rangle - \langle \mathbf{0}n | \, \boldsymbol{r} \, | \mathbf{0}n \rangle^2 \right] \tag{2.81}$$

where Ω denotes the spread in the Wannier function and $\boldsymbol{r}$ is the position operator. Minimizing this spread yields the so-called *Maximally localized Wannier functions* (MLWFs). In (2.81), the braket notation indicates integration over the entire crystal. The sum runs over all basis functions. For details on the minimizing procedure of (2.81), interested readers are referred to Marzari et al. (2012). We still point out one thing in particular about the minimizing procedure here: in 1962 Blount showed that the matrix elements in Ω may be expressed in terms of Bloch orbitals, ∇_k and ∇_k^2 [46]

$$\langle \boldsymbol{R}n | \, \boldsymbol{r} \, | \mathbf{0}m \rangle = i \frac{V}{\left(2\pi\right)^3} \int d\boldsymbol{k} e^{i\boldsymbol{k}\cdot\boldsymbol{R}} \langle u_{n\boldsymbol{k}} | \, \nabla_{\boldsymbol{k}} \, | u_{m\boldsymbol{k}} \rangle \tag{2.82}$$

$$\langle \boldsymbol{R}n | \, \boldsymbol{r}^2 \, | \mathbf{0}m \rangle = -\frac{V}{\left(2\pi\right)^3} \int d\boldsymbol{k} e^{i\boldsymbol{k}\cdot\boldsymbol{R}} \langle u_{n\boldsymbol{k}} | \, \nabla_{\boldsymbol{k}}^2 \, | u_{m\boldsymbol{k}} \rangle \tag{2.83}$$

To evaluate the matrix elements of (2.82) and (2.83), the Bloch orbitals are assumed to be discretized onto a uniform Monkhorst-Pack mesh [47]. Using finite-differences to evaluate the matrix elements of ∇_k and ∇_k^2, Marzari et al. (2012) show that the information needed to carry out the localization procedure is the overlap between Bloch orbitals at neighboring $\boldsymbol{k}$-points

$$G_{nm}(\boldsymbol{k}, \boldsymbol{b}) = \langle u_{m,\boldsymbol{k}} | u_{n,\boldsymbol{k}+\boldsymbol{b}} \rangle \tag{2.84}$$

The braket notation in (2.84) again indicates integration over the whole crystal structure. If the overlaps (2.84) are tabulated, the localization and, equally important, the effect any unitary transformation may have on the localization, is available through (2.81), (2.82) and (2.83) with no need to recalculate overlaps, or through any other interaction with the original Bloch states used to generate Wannier functions.

2.5 Gaunt numbers

The calculation of scattering rates with Fermi's Golden rule involves overlaps between (L)APW(+lo) functions. As shown in Chapter 3, the angular integral over three spherical harmonics functions must then be evaluated. These are normally called Gaunt numbers [48]

$$\left\langle Y_{m_1}^{l_1} \middle| Y_{m_2}^{l_2} \middle| Y_{m_3}^{l_3} \right\rangle = (-1)^{m_1} \left[\frac{(2l_1+1)(2l_2+1)(2l_3+1)}{4\pi} \right]^{1/2} \begin{pmatrix} l_1 & l_2 & l_3 \\ 0 & 0 & 0 \end{pmatrix} \begin{pmatrix} l_1 & l_2 & l_3 \\ m_1 & m_2 & m_3 \end{pmatrix} \tag{2.85}$$

Here, the LHS represents the integral over three spherical harmonics, each with their own angular momentum and magnetic quantum numbers l and m. The last two parentheses matrices on the RHS denote Wigner 3-j symbols [49]. These are related to the Clebsch-Gordan coefficients and similarly denote quantities arising when considering coupled angular momenta. While an exact treatment of the Wigner 3-j symbols for all values of angular momentum and magnetic quantum numbers is difficult, an expression providing high accuracy for $l \leq 50$ is presented in the EXCITING code manual [50]. This expression reads

$$\begin{pmatrix} l_1 & l_2 & l_3 \\ m_1 & m_2 & m_3 \end{pmatrix} = (-1)^{l_1+l_2+m_3} \times \sqrt{\frac{(l_1+m_1)!(l_2+m_2)!(l_3+m_3)!(l_3-m_3)!(l_2-m_2)!(l_1-m_1)!}{(l_2-l_1+l_3)!(l_1-l_2+l_3)!(l_1+l_2-l_3)!(1+j_1+j_2+j_3)!}} \sum_{k=max(0,l_2-l_3-m_1,l_1-l_3+m_2)}^{min(l_1+l_2-l_3,l_1-m_1,l_2+m_2)} (-1)^k \frac{(l_2-l_1+l_3)!(l_1-l_2+l_3)!(l_1+l_2-l_3)!}{(l_3-l_1-m_2+k)!(l_3-l_2+m_1+k)!(l_1+l_2-l_3-k)!k!(l_1-m_1-k)!(l_2+m_2-k)} \tag{2.86}$$

For this expression to yield accurate Gaunt numbers, none of the spherical harmonics states participating in the overlap can have quantum angular momentum exceeding $l = 50$. To see that this is indeed the case for us, consider the states of interest when dealing with transport phenomena: In semiconductors, the band edge states mainly consist of s, p, d and f components, corresponding to l ranging from zero to four [10, 30]. At most, a handful of higher l components may be added to account for the crystal nature of semiconductors. In conclusion, with the expression in (2.86) it becomes possible to evaluate the Gaunt coefficients of (2.85) at high precision, in a rather straightforward manner, instead of numerically evaluating the angular integrals over three spherical harmonics.

Chapter 3

Matrix elements

In this section, an analytical expression for the wavefunction overlap factor between different carrier states, suitable for integration over the Brillouin-zone, is arrived upon. The wavefunction overlap factor is expressed in terms of, first, an integral between (L)APW(+lo) basis functions, and second, an integral between Wannier functions.

Such overlap expressions have already been presented in a specialization project by this author [2], and comparably, the expressions presented in this thesis are a continuation as well as an improvement in many respects: First, a much tidier notation has been employed, permitting the reintroduction of band indices n, spin indices $\boldsymbol{\sigma}$, and region I indices β explicitly. This is made possible by using the compact notations $\mu = \{n, \boldsymbol{\sigma}, \boldsymbol{k}\}$ and $\gamma = \{n, \boldsymbol{\sigma}, \boldsymbol{R}\}$. Second, a generalization has been made from radial functions acquired by solving the one-electron Schrödinger equation, to relativistic 4-component radial functions obtained from the one-electron Dirac equation. This results in a two-component norm, as demonstrated in Chapter 2.3.7. Third, the region I overlaps involve an integral over three spherical harmonics. Although these were identified as Gaunt numbers in the specialization project, no analytical expression was given. The discussion in Chapter 2.5 permits the immediate computation of a Gaunt number once l and m of each spherical harmonic is provided. Finally, the original expression presented for the Wannier overlap was found to be unsuitable for numeric integration over the Brillouin-zone. In particular, no connection between the Wannier overlap and the original (L)APW(+lo) functions had been established, and no convincing argument for a justifiable cut-off in the summation over Bravais lattice vectors had been discovered. As shown below in the Wannier section, a sufficiently good expression for the Wannier overlap is arrived upon here.

Turning now to the wavefunction overlap factor, we want to calculate the expression in (2.5). Once obtained, spin-flipping is taken into account through (2.4). Recall that the spin-dependent overlap factor reads

$$G_{\mu\mu'} = \left|J_{\mu\mu'}\right|^2; \quad J_{\mu\mu'} = \int_{\text{u.c}} d^3r u^*_{\mu'}(\boldsymbol{r}) u_\mu(\boldsymbol{r}) e^{i\boldsymbol{K}\cdot\boldsymbol{r}} \tag{3.1}$$

with $\mu = \{n, \boldsymbol{\sigma}, \boldsymbol{k}\}$. We will derive an expression for $J_{\mu\mu'}$ in (3.1), and once obtained, it is simply multiplied with its complex-conjugate to yield $G_{\mu\mu'}$. We split the overlap calculation into an overlap over region I and another over region II

$$J_{\mu\mu'} = J^I_{\mu\mu'} + J^{II}_{\mu\mu'} \tag{3.2}$$

with

$$\begin{aligned} J^I_{\mu\mu'} &= \int_I d^3r u^*_{\mu'}(\boldsymbol{r}) u_\mu(\boldsymbol{r}) e^{i\boldsymbol{K}\cdot\boldsymbol{r}} \\ J^{II}_{\mu\mu'} &= \int_{II} d^3r u^*_{\mu'}(\boldsymbol{r}) u_\mu(\boldsymbol{r}) e^{i\boldsymbol{K}\cdot\boldsymbol{r}} \end{aligned} \tag{3.3}$$

Before turning to the overlap in the respective bases, we consider the approximation $e^{i(\boldsymbol{k'}-\boldsymbol{k})\cdot\boldsymbol{r}} \approx 1$, expected to hold over the unit cell. This approximation is used both for the (L)APW(+lo) and Wannier overlaps, and holds well if $(\boldsymbol{k} - \boldsymbol{k}') \cdot \boldsymbol{r} \ll 1$. In the case of a small unit cell, the integration variable $\boldsymbol{r}$ will be sufficiently small over the integration domain that the approximation above is appropriate. Even if the unit cell grows, this causes the Brillouin-zone to shrink, due to their inverse relation. Let us write $\boldsymbol{k} - \boldsymbol{k}' = \tilde{\boldsymbol{K}} + \delta\boldsymbol{k}$ where $\tilde{\boldsymbol{K}}$ is a reciprocal lattice vector and $\delta\boldsymbol{k}$ is the remainder in the first BZ. As the Brillouin-zone shrinks, $\tilde{\boldsymbol{K}}$ increases in magnitude at the expense of $\delta\boldsymbol{k}$. $\tilde{\boldsymbol{K}}$ is simply absorbed into the reciprocal lattice vector in $\boldsymbol{K}$ appearing in (3.1). At the same time, $\delta\boldsymbol{k}$ shrinks so that the approximation above is justified, despite the unit cell having grown in size. Admittedly, for wavevectors at the Brillouin-zone edge, this approximation fails if $\boldsymbol{r}$ is appreciable; at the very unit cell boundary, $e^{i\boldsymbol{K}\cdot\boldsymbol{r}} = i$. Be that as it may, a similar simplification has already been made to the matrix element: in (2.2), we approximated to a constant scattering mechanism over the unit cell. Casting away the slowly varying exponential factors $e^{i\boldsymbol{k}\cdot\boldsymbol{r}}$ is consistent with the matrix element segmentation in (2.2).

3.1 (L)APW(+lo) overlap

Recall that the wavefunction in the (L)APW(+lo) basis set is given by

$$\psi_\mu(\boldsymbol{r}) = \begin{cases} \sum_L R^\beta_{\mu,L}(\boldsymbol{r}) & \text{region I} \\ \\ \frac{1}{\sqrt{V}} \sum_{\boldsymbol{G}} C_\mu(\boldsymbol{G}) e^{i(\boldsymbol{k}+\boldsymbol{G})\cdot\boldsymbol{r}} & \text{region II} \end{cases} \tag{3.4}$$

where

$$R^{\beta}_{\mu,L}(\boldsymbol{r}) = a^{\beta}_{\mu,L}\Phi^{\beta}_{1,L\sigma}(\boldsymbol{r}_{\beta}, E_{1,l}) + b^{\beta}_{\mu,L}\dot{\Phi}^{\beta}_{1,L\sigma}(\boldsymbol{r}_{\beta}, E_{1,l}) + c^{\beta}_{\mu,L}\Phi^{\beta}_{2,L\sigma}(\boldsymbol{r}_{\beta}, E_{2,l}) \quad (3.5)$$

Here, β is associated with a particular region I sphere. $\Phi^{\beta}_{L\sigma}$ is given by

$$\Phi^{\beta}_{L\sigma} = u^{\beta}_{l\sigma}Y_L \quad (3.6)$$

with $u^{\beta}_{l\sigma}$ given by

$$u^{\beta}_{l\sigma} = \begin{bmatrix} \bar{g}_l x_\sigma \\ \frac{i\sigma_r}{2Mc}\big(-\frac{d\bar{g}_l}{dr} + \frac{1}{r}\bar{g}_l\boldsymbol{\sigma}\cdot\boldsymbol{L}\big)x_\sigma \end{bmatrix} \quad (3.7)$$

which yields

$$R^{\beta}_{\mu,L}(\boldsymbol{r}) = [a^{\beta}_{\mu,L}u^{\beta}_{1,l\sigma}(r_{\beta}, E_{1,l}) + b^{\beta}_{\mu,L}\dot{u}^{\beta}_{1,l\sigma}(r_{\beta}, E_{1,l}) + c^{\beta}_{\mu,L}u^{\beta}_{2,l\sigma}(r_{\beta}, E_{2,l})]Y_L(\boldsymbol{r}_{\beta}) \quad (3.8)$$

3.1.1 Region I

Only the cell-periodic part should participate in the overlap, but using $e^{i(\boldsymbol{k'}-\boldsymbol{k})\cdot\boldsymbol{r}} \approx 1$ over the unit-cell, we instead compute the region I overlap using the whole wavefunction.

$$\begin{aligned} J_{\mu\mu'} &= \int_{\text{u.c}} d^3r u^*_{\mu'}(\boldsymbol{r})u_{\mu}(\boldsymbol{r})e^{i\boldsymbol{K}\cdot\boldsymbol{r}} \\ &= \int_{\text{u.c}} d^3r e^{i(\boldsymbol{k'}-\boldsymbol{k})\cdot\boldsymbol{r}}\psi^*_{\mu'}(\boldsymbol{r})\psi_{\mu}(\boldsymbol{r})e^{i\boldsymbol{K}\cdot\boldsymbol{r}} \\ &\approx \int_{\text{u.c}} d^3r \psi^*_{\mu'}(\boldsymbol{r})\psi_{\mu}(\boldsymbol{r})e^{i\boldsymbol{K}\cdot\boldsymbol{r}} \end{aligned} \quad (3.9)$$

In order to evaluate the overlap in region I, we first focus our attention on a given sphere β. The plane-wave $e^{i\boldsymbol{K}\cdot\boldsymbol{r}}$, appearing in (3.1), is expanded into Bessel functions and Spherical harmonics with their origin at the center of sphere β. This point is given by the vector $\boldsymbol{R_\beta}$. See figure 3.4.

$$e^{i\boldsymbol{K}\cdot\boldsymbol{r}} = 4\pi e^{i\boldsymbol{K}\cdot\boldsymbol{R_\beta}}\sum_L i^l j_l(|\boldsymbol{K}|r_{\beta})Y_L(\hat{\boldsymbol{K}})Y_L(\hat{\boldsymbol{r}}_{\boldsymbol{\beta}}) \quad (3.10)$$

Here, $j_l(|\boldsymbol{K}|r_\beta)$ is a Bessel function, Y_L is a Spherical harmonics function and $\hat{\boldsymbol{K}}$ and $\hat{\boldsymbol{r}}_{\boldsymbol{\beta}}$ unit vectors pointing along $\boldsymbol{K}$ and $\boldsymbol{r}_\beta$, respectively. $L = \{l, m\}$ as usual, and i denotes

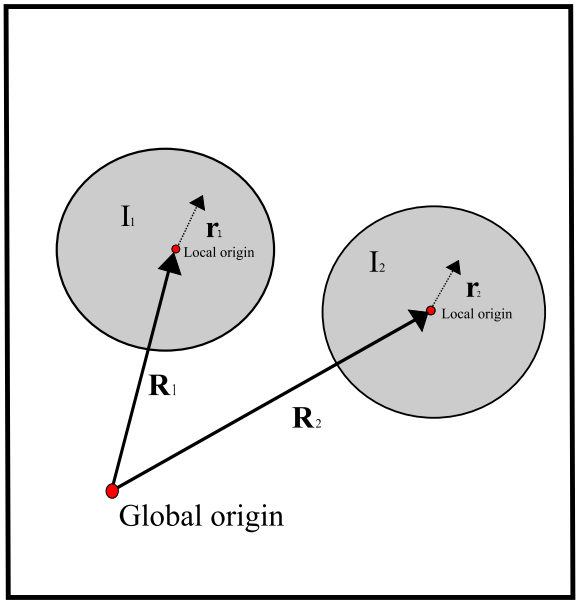

Figure 3.1: *For region I, the integral is conducted inside each atomic sphere. The integration variable $\boldsymbol{r_\beta}$ is centered around each respective $\boldsymbol{R}_\beta$ as indicated above. $\boldsymbol{R}_\beta$ associates the local origin with the global one.*

the imaginary unit. While the initial plane-wave was expressed in terms of a global origin, we have now changed from a coordinate $\boldsymbol{r}$ with respect to the global origin to $\boldsymbol{r}_\beta$ which has its origin at the center of sphere β. The two coordinate representations are related by $\boldsymbol{r} = \boldsymbol{r_\beta} - \boldsymbol{R_\beta}$. Inserting the basis from (3.5) and the Bessel expansion (3.10) into the first integral in (3.3), we get

$$
\begin{aligned}
J^I_{\mu\mu} = &\sum_{L_1,L_2,L_3} \int_I \\
&\left[a^{\beta *}_{\mu',L_1} u^{\beta *}_{1,l_1\sigma'}(r_\beta, E_{1,l_1}) + b^{\beta *}_{\mu',L_1} \dot{u}^{\beta *}_{1,l_1\sigma'}(r_\beta, E_{1,l_1}) + c^{\beta *}_{\mu',L_1} u^{\beta *}_{2,l_1\sigma'}(r_\beta, E_{2,l_1})\right] Y^*_{L_1}(\hat{\boldsymbol{r}}_\beta) \times \\
&4\pi e^{i\boldsymbol{K}\cdot\boldsymbol{R_\beta}} i^{l_2} j_{l_2}(|\boldsymbol{K}| r_\beta) Y_{L_2}(\hat{\boldsymbol{K}}) Y_{L_2}(\hat{\boldsymbol{r}}_{\boldsymbol{\beta}}) \times \\
&\left[a^{\beta}_{\mu,L_3} u^{\beta}_{1,l_3\sigma}(r_\beta, E_{1,l_3}) + b^{\beta}_{\mu,L_3} \dot{u}^{\beta}_{1,l_3\sigma}(r_\beta, E_{1,l_3}) + c^{\beta}_{\mu,L_3} u^{\beta}_{2,l_3\sigma}(r_\beta, E_{2,l_3})\right] Y_{L_3}(\hat{\boldsymbol{r}}_\beta)
\end{aligned}
\tag{3.11}
$$

The first line on the LHS is inserted for $\psi^*_{\mu'}(\boldsymbol{r})$, second line is inserted for the expansion of $e^{i\boldsymbol{K}\cdot\boldsymbol{r}}$ and the third line is inserted for $\psi_\mu(\boldsymbol{r})$. Since these depend on their own respective summation indices $L = \{l, m\}$, a subindex has been added to prevent mixing them up: 1 corresponds to expansion coefficients for $\psi^*_{\mu'}(\boldsymbol{r})$, 2 corresponds to expansion coefficients for $e^{i\boldsymbol{K}\cdot\boldsymbol{r}}$, and finally 3 corresponds to $\psi_\mu(\boldsymbol{r})$. (3.11) consists of a radial and an angular integral over the chosen sphere β in region I. Sorting out the different integrals, we are left

with a prefactor given by

$$4\pi e^{i\boldsymbol{K}\cdot\boldsymbol{R_\beta}} i^{l_2} Y_{L_2}(\hat{\boldsymbol{K}}) \tag{3.12}$$

an angular integral given by

$$\int_{\phi=0}^{2\pi}\int_{\theta=0}^{\pi} d\Omega Y^*_{L_1}(\hat{\boldsymbol{r}}_\beta) Y_{L_2}(\hat{\boldsymbol{r}}_\beta) Y_{L_3}(\hat{\boldsymbol{r}}_\beta) \tag{3.13}$$

and a radial integral given by

$$\begin{aligned}&\int_0^{R_\beta} dr_\beta r_\beta^2 \left[a^{\beta *}_{\mu',L_1} u^{\beta *}_{1,l_1\sigma'}(r_\beta, E_{1,l_1}) + b^{\beta *}_{\mu',L_1} \dot{u}^{\beta *}_{1,l_1\sigma'}(r_\beta, E_{1,l_1}) + c^{\beta *}_{\mu',L_1} u^{\beta *}_{2,l_1\sigma'}(r_\beta, E_{2,l_1})\right] j_{l_2}(|\boldsymbol{K}|r_\beta) \\ &\left[a^{\beta}_{\mu,L_3} u^{\beta}_{1,l_3\sigma}(r_\beta, E_{1,l_3}) + b^{\beta}_{\mu,L_3} \dot{u}^{\beta}_{1,l_3\sigma}(r_\beta, E_{1,l_3}) + c^{\beta}_{\mu,L_3} u^{\beta}_{2,l_3\sigma}(r_\beta, E_{2,l_3})\right]\end{aligned} \tag{3.14}$$

where the radial integral goes from radius zero to R_β, the radius of atomic sphere β. The contribution to equation (3.1) now reads

$$\begin{aligned}J^I_{\mu\mu'} = &\sum_{L_1,L_2,L_3} 4\pi e^{i\boldsymbol{K}\cdot\boldsymbol{R_\beta}} i^{l_2} Y_{L_2}(\hat{\boldsymbol{K}}) \times \\ &\int_{\phi=0}^{2\pi}\int_{\theta=0}^{\pi} d\Omega Y^*_{L_1}(\hat{\boldsymbol{r}}_\beta) Y_{L_2}(\hat{\boldsymbol{r}}_\beta) Y_{L_3}(\hat{\boldsymbol{r}}_\beta) \times \\ &\int_0^{R_\beta} dr_\beta r_\beta^2 \left[a^{\beta *}_{\mu',L_1} u^{\beta *}_{1,l_1\sigma'}(r_\beta, E_{1,l_1}) + b^{\beta *}_{\mu',L_1} \dot{u}^{\beta}_{1,l_1\sigma'}(r_\beta, E_{1,l_1}) + c^{\beta *}_{\mu',L_1} u^{\beta *}_{2,l_1\sigma'}(r_\beta, E_{2,l_1})\right] j_{l_2}(|\boldsymbol{K}|r_\beta) \times \\ &\left[a^{\beta}_{\mu,L_3} u^{\beta}_{1,l_3\sigma}(r_\beta, E_{1,l_3}) + b^{\beta}_{\mu,L_3} \dot{u}^{\beta}_{1,l_3\sigma}(r_\beta, E_{1,l_3}) + c^{\beta}_{\mu,L_3} u^{\beta}_{2,l_3\sigma}(r_\beta, E_{2,l_3})\right]\end{aligned} \tag{3.15}$$

Reorganized a bit

$$
\begin{aligned}
J^I_{\mu\mu'} &= \sum_{L_1,L_2,L_3} 4\pi e^{i\boldsymbol{K}\cdot\boldsymbol{R_\beta}} i^{l_2} Y_{L_2}(\hat{\boldsymbol{K}})\times \\
&+ \int_{\phi=0}^{2\pi}\int_{\theta=0}^{\pi} d\Omega Y^*_{L_1}(\hat{\boldsymbol{r}}_\beta) Y_{L_2}(\hat{\boldsymbol{r}}_\beta) Y_{L_3}(\hat{\boldsymbol{r}}_\beta)\times \\
&+ a^{\beta *}_{\mu',L_1} a^{\beta}_{\mu,L_3} \int_0^{R_\beta} dr_\beta r_\beta^2 u^{\beta *}_{1,l_1\sigma'}(r_\beta, E_{1,l_1}) u^{\beta}_{1,l_3\sigma}(r_\beta, E_{1,l_3})\big] j_{l_2}(|\boldsymbol{K}|r_\beta) \\
&+ a^{\beta *}_{\mu',L_1} b^{\beta}_{\mu,L_3} \int_0^{R_\beta} dr_\beta r_\beta^2 u^{\beta *}_{1,l_1\sigma'}(r_\beta, E_{1,l_1}) \dot{u}^{\beta}_{1,l_3\sigma}(r_\beta, E_{1,l_3})\big] j_{l_2}(|\boldsymbol{K}|r_\beta) \\
&+ a^{\beta *}_{\mu',L_1} c^{\beta}_{\mu,L_3} \int_0^{R_\beta} dr_\beta r_\beta^2 u^{\beta *}_{1,l_1\sigma'}(r_\beta, E_{1,l_1}) u^{\beta}_{2,l_3\sigma}(r_\beta, E_{2,l_3})\big] j_{l_2}(|\boldsymbol{K}|r_\beta) \\
&+ b^{\beta *}_{\mu',L_1} a^{\beta}_{\mu,L_3} \int_0^{R_\beta} dr_\beta r_\beta^2 \dot{u}^{\beta *}_{1,l_1\sigma'}(r_\beta, E_{1,l_1}) u^{\beta}_{1,l_3\sigma}(r_\beta, E_{1,l_3})\big] j_{l_2}(|\boldsymbol{K}|r_\beta) \\
&+ b^{\beta *}_{\mu',L_1} b^{\beta}_{\mu,L_3} \int_0^{R_\beta} dr_\beta r_\beta^2 \dot{u}^{\beta *}_{1,l_1\sigma'}(r_\beta, E_{1,l_1}) \dot{u}^{\beta}_{1,l_3\sigma}(r_\beta, E_{1,l_3})\big] j_{l_2}(|\boldsymbol{K}|r_\beta) \\
&+ b^{\beta *}_{\mu',L_1} c^{\beta}_{\mu,L_3} \int_0^{R_\beta} dr_\beta r_\beta^2 \dot{u}^{\beta *}_{1,l_1\sigma'}(r_\beta, E_{1,l_1}) u^{\beta}_{2,l_3\sigma}(r_\beta, E_{2,l_3})\big] j_{l_2}(|\boldsymbol{K}|r_\beta) \\
&+ c^{\beta *}_{\mu',L_1} a^{\beta}_{\mu,L_3} \int_0^{R_\beta} dr_\beta r_\beta^2 u^{\beta *}_{2,l_1\sigma'}(r_\beta, E_{2,l_1}) u^{\beta}_{1,l_3\sigma}(r_\beta, E_{1,l_3})\big] j_{l_2}(|\boldsymbol{K}|r_\beta) \\
&+ c^{\beta *}_{\mu',L_1} b^{\beta}_{\mu,L_3} \int_0^{R_\beta} dr_\beta r_\beta^2 u^{\beta *}_{2,l_1\sigma'}(r_\beta, E_{2,l_1}) \dot{u}^{\beta}_{1,l_3\sigma}(r_\beta, E_{1,l_3})\big] j_{l_2}(|\boldsymbol{K}|r_\beta) \\
&+ c^{\beta *}_{\mu',L_1} c^{\beta}_{\mu,L_3} \int_0^{R_\beta} dr_\beta r_\beta^2 u^{\beta *}_{2,l_1\sigma'}(r_\beta, E_{2,l_1}) u^{\beta}_{2,l_3\sigma}(r_\beta, E_{2,l_3})\big] j_{l_2}(|\boldsymbol{K}|r_\beta)
\end{aligned}
\tag{3.16}
$$

This expression is greatly simplified in the case of a normal scattering process, i.e for $\boldsymbol{K} = 0$. In that case, the angular integral involves only two spherical harmonics functions, obeying orthonormality

$$
\int_{\phi=0}^{2\pi}\int_{\theta=0}^{\pi} d\Omega Y^*_{L_1}(\hat{\boldsymbol{r}}_\beta) Y_{L_3}(\hat{\boldsymbol{r}}_\beta) = \delta_{L_1 L_3} \tag{3.17}
$$

Also ignoring the factors in (3.16) arising from the Bessel expansion of $e^{i\boldsymbol{K}\cdot\boldsymbol{r}}$, the region I overlap will therefore read

$$
\begin{aligned}
J^I_{\mu\mu'} = \sum_L & a^{\beta*}_{\mu',L} a^{\beta}_{\mu,L} \int_0^{R_\beta} dr_\beta r_\beta^2 u^{\beta*}_{1,l\sigma'}(r_\beta, E_{1,l}) u^{\beta}_{1,l\sigma}(r_\beta, E_{1,l})\big] \\
& + a^{\beta*}_{\mu',L} b^{\beta}_{\mu,L} \int_0^{R_\beta} dr_\beta r_\beta^2 u^{\beta*}_{1,l\sigma'}(r_\beta, E_{1,l}) \dot{u}^{\beta}_{1,l\sigma}(r_\beta, E_{1,l})\big] \\
& + a^{\beta*}_{\mu',L} c^{\beta}_{\mu,L} \int_0^{R_\beta} dr_\beta r_\beta^2 u^{\beta*}_{1,l\sigma'}(r_\beta, E_{1,l}) u^{\beta}_{2,l\sigma}(r_\beta, E_{2,l})\big] \\
& + b^{\beta*}_{\mu',L} a^{\beta}_{\mu,L} \int_0^{R_\beta} dr_\beta r_\beta^2 \dot{u}^{\beta*}_{1,l\sigma'}(r_\beta, E_{1,l}) u^{\beta}_{1,l\sigma}(r_\beta, E_{1,l})\big] \\
& + b^{\beta*}_{\mu',L} b^{\beta}_{\mu,L} \int_0^{R_\beta} dr_\beta r_\beta^2 \dot{u}^{\beta*}_{1,l\sigma'}(r_\beta, E_{1,l}) \dot{u}^{\beta}_{1,l\sigma}(r_\beta, E_{1,l})\big] \\
& + b^{\beta*}_{\mu',L} c^{\beta}_{\mu,L} \int_0^{R_\beta} dr_\beta r_\beta^2 \dot{u}^{\beta*}_{1,l\sigma'}(r_\beta, E_{1,l}) u^{\beta}_{2,l\sigma}(r_\beta, E_{2,l})\big] \\
& + c^{\beta*}_{\mu',L} a^{\beta}_{\mu,L} \int_0^{R_\beta} dr_\beta r_\beta^2 u^{\beta*}_{2,l\sigma'}(r_\beta, E_{2,l}) u^{\beta}_{1,l\sigma}(r_\beta, E_{1,l}) \\
& + c^{\beta*}_{\mu',L} b^{\beta}_{\mu,L} \int_0^{R_\beta} dr_\beta r_\beta^2 u^{\beta*}_{2,l\sigma'}(r_\beta, E_{2,l}) \dot{u}^{\beta}_{1,l\sigma}(r_\beta, E_{1,l})\big] \\
& + c^{\beta*}_{\mu',L} c^{\beta}_{\mu,L} \int_0^{R_\beta} dr_\beta r_\beta^2 u^{\beta*}_{2,l\sigma'}(r_\beta, E_{2,l}) u^{\beta}_{2,l\sigma}(r_\beta, E_{2,l})\big]
\end{aligned}
\tag{3.18}
$$

3.1.2 Region II

We evaluate the overlap for region II by inserting the plane-wave basis in equation (2.33) into the second integral in (3.3)

$$
J^{II}_{\mu\mu'} = \frac{1}{V} \sum_{\boldsymbol{G_1 G_2}} C^*_{\mu'}(\boldsymbol{G_1}) C_\mu(\boldsymbol{G_2}) \int_{II} d^3 r e^{i(\boldsymbol{G_2} - \boldsymbol{G_1} + \boldsymbol{K})\cdot \boldsymbol{r}} \tag{3.19}
$$

where the integral runs over region II. We now split the integral $\int_{II} d^3\boldsymbol{r} e^{i(\boldsymbol{G_2}-\boldsymbol{G_1}-\boldsymbol{K})\cdot\boldsymbol{r}}$ into one over the unit cell and another over region I, the latter subtracted to give the right integration domain

$$
\begin{aligned}
& \frac{1}{V} \sum_{\boldsymbol{G_1 G_2}} C^*_{\mu'}(\boldsymbol{G_1}) C_\mu(\boldsymbol{G_2}) \int_{II} d^3 r e^{i(\boldsymbol{G_2} - \boldsymbol{G_1} + \boldsymbol{K})\cdot \boldsymbol{r}} \\
= & \frac{1}{V} \sum_{\boldsymbol{G_1 G_2}} C^*_{\mu'}(\boldsymbol{G_1}) C_\mu(\boldsymbol{G_2}) \int_{u.c} d^3 r e^{i(\boldsymbol{G_2} - \boldsymbol{G_1} + \boldsymbol{K})\cdot \boldsymbol{r}} \\
- & \frac{1}{V} \sum_{\boldsymbol{G_1 G_2}} C^*_{\mu'}(\boldsymbol{G_1}) C_\mu(\boldsymbol{G_2}) \int_{I} d^3 r e^{i(\boldsymbol{G_2} - \boldsymbol{G_1} + \boldsymbol{K})\cdot \boldsymbol{r}}
\end{aligned}
\tag{3.20}
$$

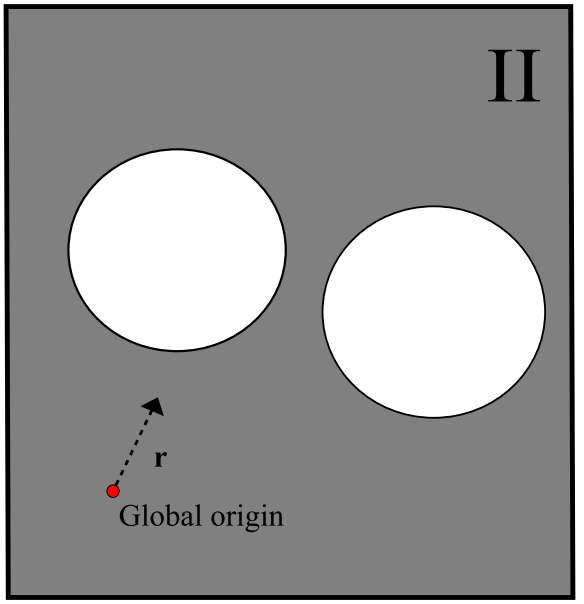

Figure 3.2: *For region II, the integral is conducted in the interstitial region, given in grey. The integration variable $\boldsymbol{r}$ is given with respect to the global origin.*

Since $\boldsymbol{G_1}$, $\boldsymbol{G_2}$ and $\boldsymbol{K}$ are reciprocal lattice vectors, so is $\boldsymbol{G_2} - \boldsymbol{G_1} + \boldsymbol{K}$. This results in a delta-function $V\delta(\boldsymbol{G_2} - \boldsymbol{G_1} + \boldsymbol{K})$ for the integral over the unit cell

$$\begin{aligned} &\frac{1}{V}\sum_{\boldsymbol{G_1}\boldsymbol{G_2}} C^*_{\mu'}(\boldsymbol{G_1})C_\mu(\boldsymbol{G_2})\int_{u.c} d^3r e^{i(\boldsymbol{G_2}-\boldsymbol{G_1}+\boldsymbol{K})\cdot\boldsymbol{r}} \\ &= \sum_{\boldsymbol{G_1}\boldsymbol{G_2}} C^*_{\mu'}(\boldsymbol{G_1})C_\mu(\boldsymbol{G_2})\delta(\boldsymbol{G_2} - \boldsymbol{G_1} + \boldsymbol{K}) \end{aligned} \tag{3.21}$$

The plane-wave integral over region I is on the other hand a sum over each atomic sphere, denoted by β in the unit cell. $\boldsymbol{r}$ represents the coordinate within the unit cell, so we write $\boldsymbol{r} = \boldsymbol{R_\beta} + \boldsymbol{r_\beta}$ to express the integral in terms of coordinates centered inside each sphere β of region I

$$\frac{1}{V}\sum_{\boldsymbol{G_1}\boldsymbol{G_2}}\sum_{\beta} C^*_{\mu'}(\boldsymbol{G_1})C_\mu(\boldsymbol{G_2})e^{i(\boldsymbol{G_2}-\boldsymbol{G_1}+\boldsymbol{K})\cdot\boldsymbol{R_\beta}}\int_{I_\beta} d^3r_\beta e^{i(\boldsymbol{G_2}-\boldsymbol{G_1}+\boldsymbol{K})\cdot\boldsymbol{r_\beta}} \tag{3.22}$$

and the sum runs over all atomic spheres β. In case $\boldsymbol{G_2} - \boldsymbol{G_1} + \boldsymbol{K} = 0$, (3.22) reduces to V_β for the respective sphere. Otherwise, we orient the z-axis along $\boldsymbol{G_2} - \boldsymbol{G_1} + \boldsymbol{K}$ and change to spherical coordinates. In total

$$\int_{I_\beta} d^3 r_\beta e^{i(\boldsymbol{G_2}-\boldsymbol{G_1}+\boldsymbol{K})\cdot\boldsymbol{r_\beta}} = \begin{cases} V_\beta & \boldsymbol{G}_2 - \boldsymbol{G}_1 + \boldsymbol{K} = 0 \\ 3V_\beta \frac{\sin x - x\cos x}{x^3} & \boldsymbol{G}_2 - \boldsymbol{G}_1 + \boldsymbol{K} \neq 0 \end{cases} \tag{3.23}$$

where $x = R_\beta|\boldsymbol{G_2} - \boldsymbol{G_1} + \boldsymbol{K}|$ and $V_\beta = \frac{4}{3}\pi R_\beta^3$, R_β being the radius of sphere β. Subtracting (3.23) from (3.21) yields

$$\begin{aligned} & J^{II}_{\mu\mu'} = \\ & \sum_{\boldsymbol{G_2}-\boldsymbol{G_1}+\boldsymbol{K}=\boldsymbol{0}} C_\mu(\boldsymbol{G_2}) \left[C^*_{\mu'}(\boldsymbol{G_1}) \left(V - \sum_\beta V_\beta \right) - \sum_\beta 3V_\beta \right. \\ & \left. \sum_{\boldsymbol{G_2}-\boldsymbol{G_1}+\boldsymbol{K}\neq\boldsymbol{0}} C^*_{\mu'}(\boldsymbol{G_1}) 3V_\beta \frac{\sin x - x\cos x}{x^3} e^{i(\boldsymbol{G_2}-\boldsymbol{G_1}+\boldsymbol{K})\cdot\boldsymbol{R_\beta}} \right] \end{aligned} \tag{3.24}$$

3.1.3 Total overlap

To summarize, we have an expression from region I

$$
\begin{aligned}
J^I_{\mu\mu'} = & \sum_{L_1,L_2,L_3} 4\pi e^{i\boldsymbol{K}\cdot\boldsymbol{R_\beta}} i^{l_2} Y_{L_2}(\hat{\boldsymbol{K}}) \times \\
+ & \int_{\phi=0}^{2\pi}\int_{\theta=0}^{\pi} d\Omega Y^*_{L_1}(\hat{\boldsymbol{r}}_\beta) Y_{L_2}(\hat{\boldsymbol{r}}_\beta) Y_{L_3}(\hat{\boldsymbol{r}}_\beta) \times \\
& + a^{\beta *}_{\mu',L_1} a^{\beta}_{\mu,L_3} \int_0^{R_\beta} dr_\beta r_\beta^2 u^{\beta *}_{1,l_1\sigma'}(r_\beta, E_{1,l_1}) u^{\beta}_{1,l_3\sigma}(r_\beta, E_{1,l_3})\big] j_{l_2}(|\boldsymbol{K}|r_\beta) \\
& + a^{\beta *}_{\mu',L_1} b^{\beta}_{\mu,L_3} \int_0^{R_\beta} dr_\beta r_\beta^2 u^{\beta *}_{1,l_1\sigma'}(r_\beta, E_{1,l_1}) \dot{u}^{\beta}_{1,l_3\sigma}(r_\beta, E_{1,l_3})\big] j_{l_2}(|\boldsymbol{K}|r_\beta) \\
& + a^{\beta *}_{\mu',L_1} c^{\beta}_{\mu,L_3} \int_0^{R_\beta} dr_\beta r_\beta^2 u^{\beta *}_{1,l_1\sigma'}(r_\beta, E_{1,l_1}) u^{\beta}_{2,l_3\sigma}(r_\beta, E_{2,l_3})\big] j_{l_2}(|\boldsymbol{K}|r_\beta) \\
& + b^{\beta *}_{\mu',L_1} a^{\beta}_{\mu,L_3} \int_0^{R_\beta} dr_\beta r_\beta^2 \dot{u}^{\beta *}_{1,l_1\sigma'}(r_\beta, E_{1,l_1}) u^{\beta}_{1,l_3\sigma}(r_\beta, E_{1,l_3})\big] j_{l_2}(|\boldsymbol{K}|r_\beta) \\
& + b^{\beta *}_{\mu',L_1} b^{\beta}_{\mu,L_3} \int_0^{R_\beta} dr_\beta r_\beta^2 \dot{u}^{\beta *}_{1,l_1\sigma'}(r_\beta, E_{1,l_1}) \dot{u}^{\beta}_{1,l_3\sigma}(r_\beta, E_{1,l_3})\big] j_{l_2}(|\boldsymbol{K}|r_\beta) \\
& + b^{\beta *}_{\mu',L_1} c^{\beta}_{\mu,L_3} \int_0^{R_\beta} dr_\beta r_\beta^2 \dot{u}^{\beta *}_{1,l_1\sigma'}(r_\beta, E_{1,l_1}) u^{\beta}_{2,l_3\sigma}(r_\beta, E_{2,l_3})\big] j_{l_2}(|\boldsymbol{K}|r_\beta) \\
& + c^{\beta *}_{\mu',L_1} a^{\beta}_{\mu,L_3} \int_0^{R_\beta} dr_\beta r_\beta^2 u^{\beta *}_{2,l_1\sigma'}(r_\beta, E_{2,l_1}) u^{\beta}_{1,l_3\sigma}(r_\beta, E_{1,l_3})\big] j_{l_2}(|\boldsymbol{K}|r_\beta) \\
& + c^{\beta *}_{\mu',L_1} b^{\beta}_{\mu,L_3} \int_0^{R_\beta} dr_\beta r_\beta^2 u^{\beta *}_{2,l_1\sigma'}(r_\beta, E_{2,l_1}) \dot{u}^{\beta}_{1,l_3\sigma}(r_\beta, E_{1,l_3})\big] j_{l_2}(|\boldsymbol{K}|r_\beta) \\
& + c^{\beta *}_{\mu',L_1} c^{\beta}_{\mu,L_3} \int_0^{R_\beta} dr_\beta r_\beta^2 u^{\beta *}_{2,l_1\sigma'}(r_\beta, E_{2,l_1}) u^{\beta}_{2,l_3\sigma}(r_\beta, E_{2,l_3})\big] j_{l_2}(|\boldsymbol{K}|r_\beta)
\end{aligned}
\tag{3.25}
$$

and an expression from region II

$$
\begin{aligned}
& J^{II}_{\mu\mu'} = \\
& \sum_{\boldsymbol{G_2}-\boldsymbol{G_1}+\boldsymbol{K}=\boldsymbol{0}} C_\mu(\boldsymbol{G_2}) \Bigg[C^*_{\mu'}(\boldsymbol{G_1}) \Bigg(V - \sum_\beta V_\beta \Bigg) - \sum_\beta 3V_\beta \\
& \sum_{\boldsymbol{G_2}-\boldsymbol{G_1}+\boldsymbol{K}\neq\boldsymbol{0}} C^*_{\mu'}(\boldsymbol{G_1}) 3V_\beta \frac{\sin x - x\cos x}{x^3} e^{i(\boldsymbol{G_2}-\boldsymbol{G_1}+\boldsymbol{K})\cdot\boldsymbol{R_\beta}} \Bigg]
\end{aligned}
\tag{3.26}
$$

with $x = R_\beta|\boldsymbol{G_2}-\boldsymbol{G_1}+\boldsymbol{K}|$ and $V_\beta = \frac{4}{3}\pi R_\beta^3$, R_β being the radius of sphere β. Together, these correspond to the overlap integral in (3.1)

3.2 Wannier overlap

Having obtained an overlap expression for (3.1) based on (L)APW(+lo), the next step is to do the same for a Wannier representation. The inverse Wannier transformation reads

$$\psi_\mu(\boldsymbol{r}) = \frac{1}{N}\sum_{\boldsymbol{R}}\sum_{m=1}^{N} U^\dagger_{nm}(\boldsymbol{k}) e^{i\boldsymbol{k}\cdot\boldsymbol{R}}\omega_\gamma(\boldsymbol{r}) \tag{3.27}$$

where $\mu = \{n, \boldsymbol{\sigma}, \boldsymbol{k}\}$ and $\gamma = \{m, \boldsymbol{\sigma}, \boldsymbol{R}\}$, $\boldsymbol{R}$ denoting a Bravais lattice vector. We are interested in the cell-periodic Bloch function. The dagger denotes the conjugate transpose of the unitary matrix used to maximally localize the WFs.

$$u_\mu(\boldsymbol{r}) = \frac{1}{N}\sum_{\boldsymbol{R}}\sum_{m=1}^{N} U^\dagger_{nm}(\boldsymbol{k}) e^{i\boldsymbol{k}\cdot(\boldsymbol{R}-\boldsymbol{r})}\omega_\gamma(\boldsymbol{r}) \tag{3.28}$$

Inserting the expression from (3.28) and its complex-conjugate into (3.1) yields

$$\begin{aligned} J_{\mu\mu'} = \frac{1}{N^2}\int_{\text{u.c}} d^3r \sum_{\boldsymbol{R'}} e^{i\boldsymbol{k'}\cdot(\boldsymbol{R'}-\boldsymbol{r})} \sum_{m'=1}^{N} \left(U^\dagger_{n'm'}(\boldsymbol{k'})\right)^* \omega^*_{\gamma'}(\boldsymbol{r}) \\ \sum_{\boldsymbol{R}} e^{-i\boldsymbol{k}\cdot(\boldsymbol{R}-\boldsymbol{r})} \sum_{m=1}^{N} U^\dagger_{nm}(\boldsymbol{k})\omega_\gamma(\boldsymbol{r}) e^{i\boldsymbol{K}\cdot\boldsymbol{r}} \end{aligned} \tag{3.29}$$

with $\mu = \{n, \boldsymbol{\sigma}, \boldsymbol{k}\}$ and $\gamma = \{m, \boldsymbol{\sigma}, \boldsymbol{R}\}$; $\mu' = \{n', \boldsymbol{\sigma'}, \boldsymbol{k'}\}$ and $\gamma' = \{m', \boldsymbol{\sigma'}, \boldsymbol{R'}\}$. To proceed, we now evaluate the Wannier integral in (3.29). This must be done for each region of the (L)APW(+lo) basis. We again omit the factor $e^{i(\boldsymbol{k'}-\boldsymbol{k})\cdot\boldsymbol{r}}$ since it is slowly-varying over the unit cell

$$\begin{aligned} J_{\mu\mu'} =& \frac{1}{N^2}\sum_{\boldsymbol{R'}}\sum_{\boldsymbol{R}} e^{i\boldsymbol{k'}\cdot\boldsymbol{R'}-i\boldsymbol{k}\cdot\boldsymbol{R}} \sum_{m'=1}^{N}\sum_{m=1}^{N} U_{m'n'}(\boldsymbol{k'}) U^\dagger_{nm}(\boldsymbol{k}) \\ & \int_{\text{u.c}} d^3r e^{i\boldsymbol{K}\cdot\boldsymbol{r}} \omega^*_{\gamma'}(\boldsymbol{r})\omega_\gamma(\boldsymbol{r}) \end{aligned} \tag{3.30}$$

From (3.30), we see that the Wannier overlap includes a summation over real-space lattice points. A discrete $\boldsymbol{k}$-mesh in the Brillouin-zone yields a periodicity of the Bloch states, and consequently the Wannier states, over a supercell in real space. The number of lattice points in this supercell equals the number of $\boldsymbol{k}$-points in the original first principles mesh. The summations each run over all crystal lattice points within this supercell, typically a couple of thousand, as the number of lattice points scales with the number of k-points in the Brillouin-zone. A practical implementation must involve a cut-off radius around a given lattice point $\boldsymbol{R}$ to restrict the summation.

A guarantee for such a cut-off radius is given by Panati and Pisante (2011). They prove that Maximally localized Wannier functions in 3D decay exponentially, something that had earlier only been conjectured [51]. If we start evaluating the overlap between Wannier functions centered around the nearest lattice points, and move outward from $\boldsymbol{R}_0$, we will eventually reach a distance $|\boldsymbol{R}_{cut} - \boldsymbol{R}_0|$ where contributions from any Wannier function centered around lattice points further out, becomes negligible. This is ensured by the exponential localization of WFs.

The introduction of a cut-off radius allows us to perform a manageable summation within the cut-off radius distance $|\boldsymbol{R}_{cut} - \boldsymbol{R}_0|$ from a selected lattice point $\boldsymbol{R}_o$ without loss of significant contributions to the overlap factor. Such a summation should in principle be carried out for the equivalent Wannier function centered around every lattice point in the crystal structure, but Wannier function $\omega_{\boldsymbol{R'}n}$ is the periodic image of $\omega_{\boldsymbol{R}n}$, shifted by $\boldsymbol{R'} - \boldsymbol{R}$. This means that once all contributions within the cut-off radius have been taken into account for a particular $\omega_{\boldsymbol{R}_0 n}$ centered around $\boldsymbol{R}_0$, we take all periodic images into account simply by multiplying with the number of lattice points. This reduces the formidable task of carrying out a summation over $\boldsymbol{R}$ and $\boldsymbol{R'}$ to a summation over real-space lattice points confined to a cut-off radius, conceivably a couple of unit cells in each direction. Surface effects are neglected in this final step, appropriate for a sufficiently large crystal. We are left with

$$\begin{aligned} J_{\mu\mu'} =& \frac{1}{N} \sum_{\boldsymbol{R}} e^{i\boldsymbol{k'}\cdot\boldsymbol{0_R} - i\boldsymbol{k}\cdot\boldsymbol{R}} \sum_{m'=1}^{N} \sum_{m=1}^{N} U_{m'n'}(\boldsymbol{k'}) U^{\dagger}_{nm}(\boldsymbol{k}) \\ & \int_{\text{u.c}} d^3 r e^{i\boldsymbol{K}\cdot\boldsymbol{r}} \omega^*_{\gamma'}(\boldsymbol{r}) \omega_{\gamma}(\boldsymbol{r}) \end{aligned} \tag{3.31}$$

where now $\gamma = \{n, \boldsymbol{\sigma}, \boldsymbol{R}\}$ and $\gamma' = \{n', \boldsymbol{\sigma'}, \boldsymbol{0_R}\}$, $\boldsymbol{0_R}$ being a reference lattice point.

3.2.1 Region I

For a particular sphere β in region I, the Bloch state reads

$$\psi_\mu(\boldsymbol{r}_\beta) = \sum_L \left[a^\beta_{\mu L} u^\beta_{1,l\sigma}(r_\beta, E_{1,l}) + b^\beta_{\mu L} \dot{u}^\beta_{1,l\sigma}(r_\beta, E_{1,l}) + c^\beta_{\mu L} u^\beta_{2,l\sigma}(r_\beta, E_{2,l}) \right] Y_L(\hat{\boldsymbol{r}}_\beta) \tag{3.32}$$

where r_β originates in the center of the sphere β, at point $\boldsymbol{R}_\beta$. The Wannier transformation, relating N Wannier states to N Bloch states, reads

$$w_\gamma(\boldsymbol{r}) = \frac{V}{(2\pi)^3} \int_{BZ} d\boldsymbol{k} \sum_{p=1}^{N} e^{-i\boldsymbol{k}\cdot\boldsymbol{R}} U_{pn}(\boldsymbol{k}) \psi_\mu(\boldsymbol{r}) \tag{3.33}$$

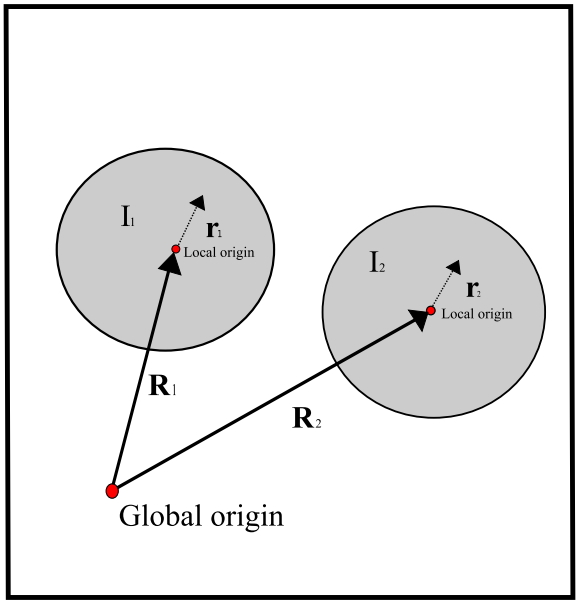

Figure 3.3: *For region I, the integral is conducted inside each atomic sphere. The integration variable $\boldsymbol{r_\beta}$ is centered around each respective $\boldsymbol{R}_\beta$ as indicated above. $\boldsymbol{R}_\beta$ associates the local origin with the global one.*

where the unitary matrix is chosen such that it maximally localizes the Wannier functions. This corresponds to N Wannier functions since the index n will take on N integer values. Inserting for (3.32) into (3.33) yields

$$\begin{aligned} w_\gamma(\boldsymbol{r}_\beta) = \sum_L \Big[\Big(\frac{V}{(2\pi)^3} \int_{BZ} d\boldsymbol{k} \sum_{p=1}^{N} e^{-i\boldsymbol{k}\cdot\boldsymbol{R}} U_{pn}(\boldsymbol{k}) a^\beta_{\mu L}(\boldsymbol{k}) \Big) u^\beta_{1,l\sigma}(r_\beta, E_{1,l}) + \\ \Big(\frac{V}{(2\pi)^3} \int_{BZ} d\boldsymbol{k} \sum_{p=1}^{N} e^{-i\boldsymbol{k}\cdot\boldsymbol{R}} U_{pn}(\boldsymbol{k}) b^\beta_{\mu L}(\boldsymbol{k}) \Big) \dot{u}^\beta_{1,l\sigma}(r_\beta, E_{1,l}) + \\ \Big(\frac{V}{(2\pi)^3} \int_{BZ} d\boldsymbol{k} \sum_{p=1}^{N} e^{-i\boldsymbol{k}\cdot\boldsymbol{R}} U_{pn}(\boldsymbol{k}) c^\beta_{\mu L}(\boldsymbol{k}) \Big) u^\beta_{2,l\sigma}(r_\beta, E_{2,l}) \Big] Y_L(\hat{\boldsymbol{r}}_\beta) \end{aligned} \tag{3.34}$$

where the wavevector dependence of the expansion coefficients is shown explicitly because an integral is performed over the Brillouin-zone: instead of $a^\beta_{\mu L}$, $b^\beta_{\mu L}$ and $c^\beta_{\mu L}$, we write $a^\beta_{\mu L}(\boldsymbol{k})$, $b^\beta_{\mu L}(\boldsymbol{k})$ and $c^\beta_{\mu L}(\boldsymbol{k})$. Defining the parentheses in each line as a new set of expansion coefficients

$$\begin{aligned}
\Big(\frac{V}{(2\pi)^3}\int_{BZ} d\boldsymbol{k} \sum_{p=1}^{N} e^{-i\boldsymbol{k}\cdot\boldsymbol{R}} U_{pn}(\boldsymbol{k}) a^{\beta}_{\mu L}(\boldsymbol{k})\Big) &\equiv a^{\beta}_{\gamma L} \\
\Big(\frac{V}{(2\pi)^3}\int_{BZ} d\boldsymbol{k} \sum_{p=1}^{N} e^{-i\boldsymbol{k}\cdot\boldsymbol{R}} U_{pn}(\boldsymbol{k}) b^{\beta}_{\mu L}(\boldsymbol{k})\Big) &\equiv b^{\beta}_{\gamma L} \\
\Big(\frac{V}{(2\pi)^3}\int_{BZ} d\boldsymbol{k} \sum_{p=1}^{N} e^{-i\boldsymbol{k}\cdot\boldsymbol{R}} U_{pn}(\boldsymbol{k}) c^{\beta}_{\mu L}(\boldsymbol{k})\Big) &\equiv c^{\beta}_{\gamma L}
\end{aligned} \tag{3.35}$$

where again $\gamma = \{n, \boldsymbol{\sigma}, \boldsymbol{R}\}$, yields Wannier functions

$$w_{\gamma}(\boldsymbol{r}_{\beta}) = \sum_{L} \Big[a^{\beta}_{\gamma L} u^{\beta}_{1,l\sigma}(r_{\beta}, E_{1,l}) + b^{\beta}_{\gamma L} \dot{u}^{\beta}_{1,l\sigma}(r_{\beta}, E_{1,l}) + c^{\beta}_{\gamma L} u^{\beta}_{2,l\sigma}(r_{\beta}, E_{2,l})\Big] Y_L(\hat{\boldsymbol{r}}_{\beta}) \tag{3.36}$$

We next turn to the exponential factor $e^{i\boldsymbol{K}\cdot\boldsymbol{r}}$ appearing in (3.30). $\boldsymbol{r}$ denotes the coordinate vector with respect to a global origin. We expand it in terms of Bessel functions centered around sphere β

$$e^{i\boldsymbol{K}\cdot\boldsymbol{r}} = 4\pi e^{i\boldsymbol{K}\cdot\boldsymbol{R}_{\boldsymbol{\beta}}} \sum_{L} i^l j_l(|\boldsymbol{q}|r_{\beta}) Y_L(\hat{\boldsymbol{K}}) Y_L(\hat{\boldsymbol{r}}_{\boldsymbol{\beta}}) \tag{3.37}$$

We finally insert for (3.36) and (3.37) into the integral in (3.30)

$$\begin{aligned}
&\int_{\mathrm{I}} d^3r \\
&\sum_{L_1} \Big[a^{\beta *}_{\gamma' L_1} u^{\beta *}_{1,l_1\sigma}(r_{\beta}, E_{1,l_1}) + b^{\beta *}_{\gamma' L_1} \dot{u}^{\beta *}_{1,l_1\sigma}(r_{\beta}, E_{1,l_1}) + c^{\beta *}_{\gamma' L_1} u^{\beta *}_{2,l_1\sigma}(r_{\beta}, E_{2,l_1})\Big] Y^*_{L_1}(\hat{\boldsymbol{r}}_{\beta}) \\
&4\pi e^{i\boldsymbol{K}\cdot\boldsymbol{R}_{\boldsymbol{\beta}}} \sum_{L_2} i^l j_{l_2}(|\boldsymbol{q}|r_{\beta}) Y_{L_2}(\hat{\boldsymbol{K}}) Y_{L_2}(\hat{\boldsymbol{r}}_{\boldsymbol{\beta}}) \\
&\sum_{L_3} \Big[a^{\beta}_{\gamma L_3} u_{1,l_3\sigma}(r_{\beta}, E_{1,l_3}) + b^{\beta}_{\gamma L_3} \dot{u}^{\beta}_{1,l_3\sigma}(r_{\beta}, E_{1,l_3}) + c^{\beta}_{\gamma L_3} u^{\beta}_{2,l_3\sigma}(r_{\beta}, E_{2,l_3})\Big] Y^*_{L_3}(\hat{\boldsymbol{r}}_{\beta})
\end{aligned} \tag{3.38}$$

This yields an overlap for region I

$$J^I_{\mu\mu'} = \frac{1}{N}\sum_{\boldsymbol{R}} e^{i\boldsymbol{k'}\cdot\mathbf{0}_{\boldsymbol{R}} - i\boldsymbol{k}\cdot\boldsymbol{R}} \sum_{m'=1}^{N}\sum_{m=1}^{N} U_{m'n'}(\boldsymbol{k'})U^{\dagger}_{nm}(\boldsymbol{k}) \sum_{L_1,L_2,L_3}\int_I$$
$$\big[a^{\beta *}_{\gamma',L_1}u^{\beta *}_{1,l_1\sigma}(r_\beta,E_{1,l_1}) + b^{\beta *}_{\gamma',L_1}\dot{u}^{\beta *}_{1,l_1\sigma}(r_\beta,E_{1,l_1}) + c^{\beta *}_{\gamma',L_1}u^{\beta *}_{2,l_1\sigma}(r_\beta,E_{2,l_1})\big]Y^*_{L_1}(\hat{\boldsymbol{r}}_{\boldsymbol{\beta}})$$
$$\times 4\pi e^{i\boldsymbol{K}\cdot\boldsymbol{R}_{\boldsymbol{\beta}}} i^{l_2} j_{l_2}(|\boldsymbol{K}|r_\beta)Y_{L_2}(\hat{\boldsymbol{K}})Y_{L_2}(\hat{\boldsymbol{r}}_{\boldsymbol{\beta}})$$
$$\times \big[a^{\beta}_{\gamma,L_3}u^{\beta}_{1,l_3\sigma}(r_\beta,E_{1,l_3}) + b^{\beta}_{\gamma,L_3}\dot{u}^{\beta}_{1,l_3\sigma}(r_\beta,E_{1,l_3}) + c^{\beta}_{\gamma,l_3m_3}u^{\beta}_{2,l_3\sigma}(r_\beta,E_{2,l_3})\big]Y_{L_3}(\hat{\boldsymbol{r}}_{\boldsymbol{\beta}}) \tag{3.39}$$

$J^I_{\mu\mu'}$ denotes the contribution to (3.29) from region I. The first line on the LHS is inserted for $\omega^*_{\gamma'}(\boldsymbol{r})$, the second line is inserted for the expansion of $e^{i\boldsymbol{K}\cdot\boldsymbol{r}}$ and the third line is inserted for $\omega_\gamma(\boldsymbol{r})$. Since these depend on their own respective summation indices $L = \{l, m\}$, a subindex has been added to prevent mixing them up: 1 corresponds to expansion coefficients for $\omega^*_{\gamma'}(\boldsymbol{r})$, 2 corresponds to expansion coefficients for $e^{i\boldsymbol{K}\cdot\boldsymbol{r}}$, and 3 corresponds to expansion coefficients for $\omega_\gamma(\boldsymbol{r})$. Sorting out the different factors, we are left with a prefactor given by

$$4\pi e^{i\boldsymbol{K}\cdot\boldsymbol{R}_{\boldsymbol{\beta}}} i^{l_2} Y_{L_2}(\hat{\boldsymbol{K}}) \tag{3.40}$$

an angular integral given by

$$\int_{\phi=0}^{2\pi}\int_{\theta=0}^{\pi} d\Omega Y^*_{L_1}(\hat{\boldsymbol{r}}_\beta)Y_{L_2}(\hat{\boldsymbol{r}}_\beta)Y_{L_3}(\hat{\boldsymbol{r}}_\beta) \tag{3.41}$$

and a radial integral given by

$$\int_0^{R_\beta} dr_\beta r^2_\beta \big[a^{\beta *}_{\gamma',L_1}u^{\beta *}_{1,l_1\sigma}(r_\beta,E_{1,l_1}) + b^{\beta *}_{\gamma',L_1}\dot{u}^{\beta *}_{1,l_1,\sigma}(r_\beta,E_{1,l_1}) + c^{\beta *}_{\gamma',L_1}u^{\beta *}_{2,l_1}(r_\beta,E_{2,l_1})\big] j_{l_2}(|\boldsymbol{K}|r_\beta)$$
$$\big[a^{\beta}_{\gamma,L_3}u^{\beta}_{1,l_3}(r_\beta,E_{1,l_3}) + b^{\beta}_{\gamma,L_3}\dot{u}^{\beta}_{1,l_3}(r_\beta,E_{2,l_3}) + c^{\beta}_{\gamma,L_3}u^{\beta}_{2,l_3}(r_\beta,E_{2,l_3})\big] \tag{3.42}$$

where the radial integral goes from radius zero to R_β, the radius of atomic sphere β. The contribution from region I to equation (3.1) now reads

$$J^I_{\mu\mu'} = \frac{1}{N}\sum_{\boldsymbol{R}} e^{i\boldsymbol{k'}\cdot\boldsymbol{0_R} - i\boldsymbol{k}\cdot\boldsymbol{R}} \sum_{m'=1}^{N}\sum_{m=1}^{N} U_{m'n'}(\boldsymbol{k'})U^{\dagger}_{nm}(\boldsymbol{k}) \sum_{L_1,L_2,L_3} 4\pi e^{i\boldsymbol{K}\cdot\boldsymbol{R_\beta}} i^{l_2} Y_{L_2}(\hat{\boldsymbol{K}})$$
$$\int_{\phi=0}^{2\pi}\int_{\theta=0}^{\pi} d\Omega Y^*_{L_1}(\hat{\boldsymbol{r}}_\beta)Y_{L_2}(\hat{\boldsymbol{r}}_\beta)Y_{L_3}(\hat{\boldsymbol{r}}_\beta)$$
$$\int_0^{R_\beta} dr_\beta r_\beta^2 \left[a^{\beta *}_{\gamma',L_1} u^{\beta *}_{1,l_1}(r_\beta, E_{1,l_1}) + b^{\beta *}_{\gamma',L_1} \dot{u}^{\beta *}_{1,l_1}(r_\beta, E_{1,l_1}) + c^{\beta *}_{\gamma',L_1} u^{\beta *}_{2,l_1}(r_\beta, E_{2,l_1})\right] j_{l_2}(|\boldsymbol{K}|r_\beta)$$
$$\left[a^{\beta}_{\gamma,L_3} u^{\beta}_{1,l_3}(r_\beta, E_{1,l_3}) + b^{\beta}_{\gamma,L_3} \dot{u}^{\beta}_{1,l_3}(r_\beta, E_{1,l_3}) + c^{\beta}_{\gamma,L_3} u^{\beta}_{2,l_3}(r_\beta, E_{2,l_3})\right] \tag{3.43}$$

3.2.2 Region II

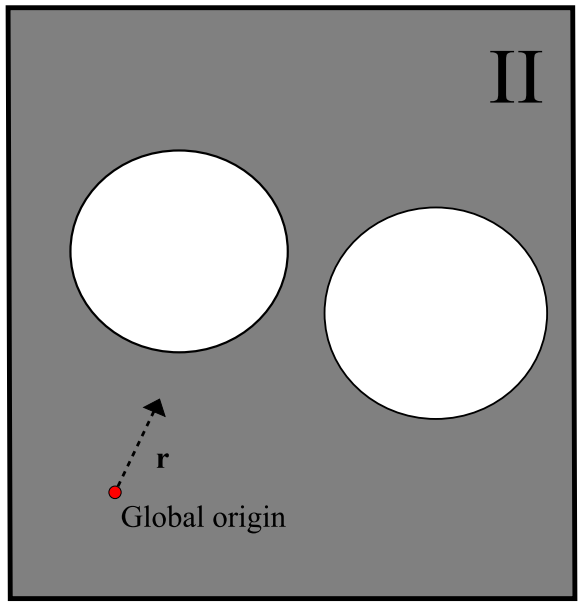

Figure 3.4: *For region II the integral is conducted in the interstitial region, given in grey. The integration variable $\boldsymbol{r}$ is given with respect to the global origin.*

In region II, the basis reads

$$\psi_\mu(\boldsymbol{r}) = \frac{1}{\sqrt{V}}\sum_{\boldsymbol{G}} C_\mu(\boldsymbol{G}) e^{i(\boldsymbol{k}+\boldsymbol{G})\cdot\boldsymbol{r}} \tag{3.44}$$

with $\mu = \{n, \boldsymbol{\sigma}, \boldsymbol{k}\}$. The Wannier transformation (3.33) yields Wannier functions for region II of the form

$$w_\gamma(\boldsymbol{r}) = \frac{1}{\sqrt{V}} \sum_{\boldsymbol{G}} \frac{V}{(2\pi)^3} \int_{BZ} d\boldsymbol{k} \sum_{m=1}^{N} U_{mn}(\boldsymbol{k}) C_\mu(\boldsymbol{G}) e^{i(\boldsymbol{k}+\boldsymbol{G})\cdot\boldsymbol{r} - i\boldsymbol{k}\cdot\boldsymbol{R}} \tag{3.45}$$

with $\gamma = \{n, \boldsymbol{\sigma}, \boldsymbol{R}\}$ and $\mu = \{m, \boldsymbol{\sigma}, \boldsymbol{k}\}$. Making the approximation $e^{i\boldsymbol{k}\cdot\boldsymbol{r}} \approx 1$ over the unit cell again allows us to express the region II Wannier functions in terms of plane-waves

$$w_\gamma(\boldsymbol{r}) = \frac{1}{\sqrt{V}} \sum_{\boldsymbol{G}} \frac{V}{(2\pi)^3} \int_{BZ} d\boldsymbol{k} \sum_{m=1}^{N} U_{mn}(\boldsymbol{k}) C_\mu(\boldsymbol{G}) e^{i\boldsymbol{G}\cdot\boldsymbol{r} - i\boldsymbol{k}\cdot\boldsymbol{R}} \tag{3.46}$$

By introducing

$$C_\gamma(\boldsymbol{g}) \equiv \left(\frac{V}{(2\pi)^3} \int_{BZ} d\boldsymbol{k} \sum_{m=1}^{N} U_{mn}(\boldsymbol{k}) C_\mu(\boldsymbol{G}) e^{-i\boldsymbol{k}\cdot\boldsymbol{R}} \right) \tag{3.47}$$

the Wannier functions in region II may be written as

$$w_\gamma(\boldsymbol{r}) = \frac{1}{\sqrt{V}} \sum_{\boldsymbol{G}} C_{\gamma\boldsymbol{G}} e^{i\boldsymbol{G}\cdot\boldsymbol{r}} \tag{3.48}$$

This expression is now inserted into the overlap integral for region II

$$J^{II}_{\mu\mu'} = \frac{1}{N} \sum_{\boldsymbol{R}} e^{i\boldsymbol{k'}\cdot\boldsymbol{0_R} - i\boldsymbol{k}\cdot\boldsymbol{R}} \sum_{m'=1}^{N} \sum_{m=1}^{N} U_{m'n'}(\boldsymbol{k'}) U^\dagger_{nm}(\boldsymbol{k}) \int_{\mathrm{II}} d^3r e^{i\boldsymbol{K}\cdot\boldsymbol{r}} \omega^*_{\gamma'}(\boldsymbol{r}) \omega_\gamma(\boldsymbol{r}) \tag{3.49}$$

yielding

$$\begin{aligned} J^{II}_{\mu\mu'} = & \frac{1}{N} \sum_{\boldsymbol{R}} e^{i\boldsymbol{k'}\cdot\boldsymbol{0_R} - i\boldsymbol{k}\cdot\boldsymbol{R}} \sum_{m'=1}^{N} \sum_{m=1}^{N} U_{m'n'}(\boldsymbol{k'}) U^\dagger_{nm}(\boldsymbol{k}) \\ & \frac{1}{V} \int_{\mathrm{II}} d^3r e^{i\boldsymbol{K}\cdot\boldsymbol{r}} \sum_{\boldsymbol{G_1}} C^*_{\gamma'\boldsymbol{G_1}} e^{-i\boldsymbol{G_1}\cdot\boldsymbol{r}} \sum_{\boldsymbol{G_2}} C_{\gamma\boldsymbol{G_2}} e^{i\boldsymbol{G_2}\cdot\boldsymbol{r}} \end{aligned} \tag{3.50}$$

and reorganized a bit

$$\begin{aligned} J^{II}_{\mu\mu'} = & \frac{1}{N} \sum_{\boldsymbol{R}} e^{i\boldsymbol{k'}\cdot\boldsymbol{0_R} - i\boldsymbol{k}\cdot\boldsymbol{R}} \sum_{m'=1}^{N} \sum_{m=1}^{N} U_{m'n'}(\boldsymbol{k'}) U^\dagger_{nm}(\boldsymbol{k}) \\ & \frac{1}{V} \sum_{\boldsymbol{G_1}} \sum_{\boldsymbol{G_2}} \int_{\mathrm{II}} d^3r e^{i\boldsymbol{K}\cdot\boldsymbol{r}} C^*_{\gamma'\boldsymbol{G_1}} e^{-i\boldsymbol{G_1}\cdot\boldsymbol{r}} C_{\gamma\boldsymbol{G_2}} e^{i\boldsymbol{G_2}\cdot\boldsymbol{r}} \end{aligned} \tag{3.51}$$

We now split the integral over region II into an integral over the whole unit cell and subtract the contribution from the region I atomic spheres β. This is analogous to the treatment of the (L)APW(+lo) overlap in region II. This yields

$$\begin{aligned} J^{II}_{\mu\mu'} = \frac{1}{N}\sum_{\boldsymbol{R}} e^{i\boldsymbol{k'}\cdot\boldsymbol{0_R}-i\boldsymbol{k}\cdot\boldsymbol{R}} \sum_{m'=1}^{N}\sum_{m=1}^{N} U_{m'n'}(\boldsymbol{k'})U^{\dagger}_{nm}(\boldsymbol{k}) \\ \sum_{\boldsymbol{G_2}-\boldsymbol{G_1}+\boldsymbol{K}=\boldsymbol{0}} C_{\gamma}(\boldsymbol{G_2})\Bigg[C^{*}_{\gamma'}(\boldsymbol{G_1})\Big(V-\sum_{\beta}V_{\beta}\Big)-\sum_{\beta}3V_{\beta} \\ \sum_{\boldsymbol{G_2}-\boldsymbol{G_1}+\boldsymbol{K}\neq\boldsymbol{0}} C^{*}_{\gamma'}(\boldsymbol{G_1})3V_{\beta}\frac{\sin x - x\cos x}{x^3}e^{i(\boldsymbol{G_2}-\boldsymbol{G_1}+\boldsymbol{K})\cdot\boldsymbol{R_\beta}}\Bigg] \end{aligned} \tag{3.52}$$

Here, $x = R_\beta|\boldsymbol{G_2}-\boldsymbol{G_1}+\boldsymbol{K}|$ and $V_\beta = \frac{4}{3}\pi R^3_\beta$, R_β being the radius of sphere β.

3.2.3 Total overlap

We have an expression from region I

$$\begin{aligned} J^{I}_{\mu\mu'} = \frac{1}{N}\sum_{\boldsymbol{R}} e^{i\boldsymbol{k'}\cdot\boldsymbol{0_R}-i\boldsymbol{k}\cdot\boldsymbol{R}} \sum_{m'=1}^{N}\sum_{m=1}^{N} U_{m'n'}(\boldsymbol{k'})U^{\dagger}_{nm}(\boldsymbol{k}) \sum_{L_1,L_2L_3} 4\pi e^{i\boldsymbol{K}\cdot\boldsymbol{R_\beta}} i^{l_2} Y_{L_2}(\hat{\boldsymbol{K}}) \\ \int_{\phi=0}^{2\pi}\int_{\theta=0}^{\pi} d\Omega Y^{*}_{L_1}(\hat{\boldsymbol{r}}_\beta)Y_{L_2}(\hat{\boldsymbol{r}}_\beta)Y_{L_3}(\hat{\boldsymbol{r}}_\beta) \\ \int_0^{R_\beta} dr_\beta r^2_\beta \big[a^{\beta *}_{\gamma',L_1}u^{\beta *}_{1,l_1}(r_\beta,E_{1,l_1}) + b^{\beta *}_{\gamma',L_1}\dot{u}^{\beta *}_{1,l_1}(r_\beta,E_{1,l_1}) + c^{\beta *}_{\gamma',L_1}u^{\beta *}_{2,l_1}(r_\beta,E_{2,l_1})\big] j_{l_2}(|\boldsymbol{K}|r_\beta) \\ \big[a^{\beta}_{\gamma,L_3}u^{\beta}_{1,l_3}(r_\beta,E_{1,l_3}) + b^{\beta}_{\gamma,L_3}\dot{u}^{\beta}_{1,l_3}(r_\beta,E_{1,l_3}) + c^{\beta}_{\gamma,L_3}u^{\beta}_{2,l_3}(r_\beta,E_{2,l_3})\big] \end{aligned} \tag{3.53}$$

with the Wannier coefficients given by

$$\begin{aligned} a^{\beta}_{\gamma L} &= \int_{BZ} d\boldsymbol{k}\sum_{p=1}^{N} e^{-i\boldsymbol{k}\cdot\boldsymbol{R}}U_{pn}(\boldsymbol{k})a^{\beta}_{\mu L}(\boldsymbol{k}) \\ b^{\beta}_{\gamma L} &= \int_{BZ} d\boldsymbol{k}\sum_{p=1}^{N} e^{-i\boldsymbol{k}\cdot\boldsymbol{R}}U_{pn}(\boldsymbol{k})b^{\beta}_{\mu L}(\boldsymbol{k}) \\ c^{\beta}_{\gamma L} &= \int_{BZ} d\boldsymbol{k}\sum_{p=1}^{N} e^{-i\boldsymbol{k}\cdot\boldsymbol{R}}U_{pn}(\boldsymbol{k})c^{\beta}_{\mu L}(\boldsymbol{k}) \end{aligned} \tag{3.54}$$

and an expression from region II

$$J^{II}_{\mu\mu'} = \frac{1}{N}\sum_{\boldsymbol{R}} e^{i\boldsymbol{k'}\cdot\boldsymbol{0_R}-i\boldsymbol{k}\cdot\boldsymbol{R}} \sum_{m'=1}^{N}\sum_{m=1}^{N} U_{m'n'}(\boldsymbol{k'})U^{\dagger}_{nm}(\boldsymbol{k})$$
$$\sum_{\boldsymbol{G_2}-\boldsymbol{G_1}+\boldsymbol{K}=\boldsymbol{0}} C_{\gamma}(\boldsymbol{G_2})\Bigg[C^{*}_{\gamma'}(\boldsymbol{G_1})\Big(V-\sum_{\beta}V_{\beta}\Big)-\sum_{\beta}3V_{\beta} \tag{3.55}$$
$$\sum_{\boldsymbol{G_2}-\boldsymbol{G_1}+\boldsymbol{K}\neq\boldsymbol{0}} C^{*}_{\gamma'}(\boldsymbol{G_1})3V_{\beta}\frac{\sin x - x\cos x}{x^3}e^{i(\boldsymbol{G_2}-\boldsymbol{G_1}+\boldsymbol{K})\cdot\boldsymbol{R_\beta}}\Bigg]$$

with $x = R_\beta|\boldsymbol{G_2}-\boldsymbol{G_1}+\boldsymbol{K}|$ and $V_\beta = \frac{4}{3}\pi R^3_\beta$, R_β being the radius of sphere β. This time, the Wannier coefficients are defined as

$$C_{\gamma}(\boldsymbol{G}) = \int_{BZ} d\boldsymbol{k}\sum_{m=1}^{N} U_{mn}(\boldsymbol{k})C_{\mu\boldsymbol{G}}e^{-i\boldsymbol{k}\cdot\boldsymbol{R}} \tag{3.56}$$

3.2.4 Wannier interpolation of matrix elements

It was noted initially in this thesis that Wannier interpolation permits one to save data on a coarse mesh, and then interpolate between-lying points without significant loss of precision. The electron-phonon interaction is of principal interest in semiconductor transport, but the cost of evaluating this matrix element from first principles on a fine $(\boldsymbol{k},\boldsymbol{k'})$-mesh is very high. Although lattice vibrations in crystals are usually described in a delocalized orthonormal basis, they may be described in a localized basis which spans the exact same space for the lattice vibrations [52]. The electron-phonon matrix element may be calculated from first principles on a coarse mesh and then effectively interpolated onto a finer mesh, as demonstrated by Giustino et al. [53].

Giustino et al. do not decompose the matrix element into a wavefunction overlap factor and an interaction overlap factor, as done in (2.2), so the approach employed for the MC program will differ: We start by determining the Bloch states on a coarse Brillouin-zone mesh. Next, we transform the set of Bloch states to a set of Maximally localized Wannier functions and express the wavefunction overlap factor in terms of these, as done in (3.51). To Wannier interpolate the wavefunction overlap factor, the unitary matrices are needed on a fine mesh. These may themselves be Wannier interpolated through

$$U_{mn}(\boldsymbol{R}) = \frac{1}{N}\sum_{\boldsymbol{k}} e^{-i\boldsymbol{k}\cdot\boldsymbol{R}}U_{mn}(\boldsymbol{k}) \tag{3.57}$$

$$U_{mn}(\boldsymbol{k}) = \sum_{\boldsymbol{R}} e^{i\boldsymbol{k}\cdot\boldsymbol{R}}U_{mn}(\boldsymbol{R}) \tag{3.58}$$

Here, $U_{mn}(\boldsymbol{R})$ is the contribution to unitary matrix $U_{mn}(\boldsymbol{k})$ from lattice point $\boldsymbol{R}$, as defined in (3.57). As mentioned earlier, the discretization of the Brillouin-zone yields Wannier functions periodic in a supercell, with the number of lattice points within this supercell equal to the number of discrete $\boldsymbol{k}$-points in the discretized Brillouin-zone. This number is denoted N in (3.57). Due to the exponential localization of WFs within this supercell, $U_{mn}(\boldsymbol{R})$ decays rapidly with $|\boldsymbol{R}|$ [54]. This in turn permits an inexpensive interpolation of the unitary matrix and thus the wavefunction overlap factor.

As long as the interaction matrix element (2.2) is also available on a fine mesh, the total scattering rates on the LHS of (2.2) are readily computed on a fine mesh.

Chapter 4

Implementation

4.1 Output from first principles programs

Now that the wavefunction overlap factor has been derived both in the (L)APW(+lo) and Wannier bases, the first step towards implementation is to obtain the necessary information from Wien2k and Wannier90 to compute the (L)APW(+lo) and Wannier overlaps, respectively.

From Wien2k, we have extracted the basis coefficients for region I and II, respectively, and the radial functions associated with each basis coefficient of region I. It is possible to read the basis coefficients from case.vector, where <case> is replaced with the session name of the particular Wien2k-simulation. This is however tedious as the case.vector file is unformatted. Another option, the one selected in this scheme, is to generate the files case.almblm and case.radwf. These print the basis coefficients and radial functions from region I by running the routine *lapw2*. For *lapw2* to generate case.almblm and case.radwf, the option ALM must be selected in the input file case.in2. Basis coefficients in case.almblm are displayed in ten columns: the first two pairs represent the APW basis coefficients, first the real and then the imaginary component; the next two pairs represent the basis coefficients in the LAPW method; and finally, the last two pairs denote local orbital basis coefficients. In case.radwf, an exponential mesh, yielding finer grid near the origin and coarser further out, is used to display two columns representing the large and small radial wavefunction components in (3.7).

For the interstitial region, the option WFPRI in case.in1 will write the region II basis coefficients to case.output1. If the crystal structure under simulation has inversion symmetry, then for each k-point, the local orbital-coefficients c_{lo} are printed immediately after the plane-wave coefficients. Recall that these coefficients appear in (2.40) in the discussion on lattices with inversion symmetry. Each local-orbital-coefficient corresponds to a particular

reciprocal lattice vector.

Finally, the unitary transformation, needed in the Maximally localized Wannier transformation, is given in case.wout after running the softwares Wien2Wannier and Wannier90 [15, 16]. Once all relevant data has been extracted, the next step is to implement routines computing the wavefunction overlap factor for region I and II, in the (L)APW(+lo) and Wannier bases, respectively.

4.2 Overlap routines

Numerical integration over three-dimensional space can be notoriously difficult [55]. The result may also vary according to what numerical scheme is employed. To minimize the error in the overlap computation, we therefore take two steps: First, we treat as much as possible of the overlap analytically. Second, if possible, we use routines already available in the Wien2k source code, to ensure high compatibility between overlap routines and those already in Wien2k used to generate the output.

4.2.1 (L)APW(+lo) overlap

Wien2Wannier

One option is to extract the wavefunction overlap factor from a software Wien2Wannier. Recall from Chapter 2.4.2, dealing with the maximal localization of Wannier functions, that an overlap between (L)APW(+lo) states at neighboring k-points is needed to construct MLWFs. This information may also be used to calculate scattering rates in the (L)APW(+lo) basis. The overlaps (2.84) are in fact tabulated in the program Wien2Wannier to provide necessary input for the program Wannier90. Since the overlaps are given free of any computational cost after a Wannierization has been performed, they may possibly be reused when calculating scattering rates.

Yet the overlaps needed in the construction of MLWFs differ from the scattering overlap (2.4) in three regards: First, an exponential factor $e^{i\boldsymbol{K}\cdot\boldsymbol{r}}$ is present in (2.4), but not found in the overlap (2.84) used to construct MLWFs. Second, in (2.4), unlike in Wien2Wannier, initial spin states are averaged over and final spin states summed over. Third, the overlaps needed in the construction of MLWFs are only taken between neighboring k-points. The initial and final charge carrier states are not restricted to neighboring k-points; they are not even restricted to states in the first Brillouin-zone. Thus, the overlaps needed to calculate scattering rates represents only a tiny fraction of the overlaps needed for determining the scattering rates of interest. We therefore conclude that although overlaps between (L)APW)+lo) basis functions are used to construct MLWFs, these are slightly different and additionally represent only a tiny part of the overlaps we need. The effort needed to extract this data is not worthwhile. We must therefore compute this overlap ourselves.

Region I

Starting with region I, the wavefunction overlap factor consists of basis coefficients multiplied with a radial and an angular integral. To carry out the radial integral, we seek a routine computing the radial integral over two-component relativistic radial functions on an exponential mesh. RINT13, a routine part of the subprogram $lapw1$ does exactly this [56]. The routine has been extracted from Wien2k, now working as part of a program reading case.radwf and then tabulating the radial overlaps. For the angular integral over three spherical harmonics functions, an expression was presented in Chapter 2.5. This expression has also been implemented, largely based on the EXCITING source code [50]. It returns the Gaunt number for a given set of angular and magnetic quantum numbers. Using the evaluated radial and angular integrals as well as the region I basis coefficients, the wavefunction overlap factor is readily computed.

Region II

For region II, the wavefunction overlap factor involves sums over reciprocal lattice vectors and the region I spheres β. A scheme for calculating optical matrix elements by Ambrosch-Draxl et al. was mentioned initially in this thesis. Although the optical matrix element $\langle n'\boldsymbol{k}| \nabla |n\boldsymbol{k}\rangle$ differs from the wavefunction overlap factor, in the basis of plane-waves, a routine computing the optical matrix element is easily modified to compute the wavefunction overlap factor. For plane-waves, the difference between a wavefunction overlap and one with ∇ is multiplication with the exponent wavevector; from a computational point of view, this is easily changed. Therefore, the routine $planew$, part of the software Optic, has been modified to compute the wavefunction overlap factor of region II. In addition to computing the wavefunction overlap factor instead of the optical matrix element, the routine has been generalized to arbitrary initial and final k-point.

4.2.2 Wannier overlap

The Wannier overlap has not yet been implemented. We will first need to Wannier transform the (L)APW(+lo) coefficients. This requires a $\boldsymbol{k}$-space integral over the Brillouin-zone, where the unitary matrix participates. The unitary matrix is outputted in Wannier90, but before running Wannier90, it is necessary to run the interface program Wien2Wannier which prepares data from a given Wien2k-simulation. Once Wannier90 has finished, the unitary matrix is available in case.wout. The $\boldsymbol{k}$-space integral involving the unitary matrix must be evaluated numerically, for example using the tetrahedron method [57].

Conveniently, the Wannier overlap and the (L)APW(+lo) overlap are linear combinations of exactly the same kind of terms. For region I, a radial integral over each sphere β in region I, and an integral over three spherical harmonics functions; for region II, a sum over reciprocal lattice vectors and region I spheres β. Once the Wannier coefficients are known, the Wannier overlap is readily evaluated with a cut-off radius invoked on the crystal lattice vectors.

4.2.3 Spin-dependent overlap

Spin-orbit coupling generally plays a significant role in transport phenomena and should eventually be included. In that case, Wien2k will output the wavefunction data in separate files for spin up and down, respectively. These files follow the nomenclature explained above, except for the addition of 'up' or 'dn' added at the end for spin up or down wavefunctions, respectively: instead of case.radwf, Wien2k outputs case.radwfup and case.radwfdn. Once the routines reading the wavefunction files have been modified, the wavefunction overlap factor may be computed with the overlap routines already implemented for region I and II in the (L)APW(+lo) overlap.

4.3 Numeric suitability for Brillouin-zone integration

Now that a new first-principles scheme has been developed for the calculation of wavefunction overlap factors, it is pertinent to turn to the following question: Are the overlap factors obtained suitable for numeric integration over the Brillouin-zone?

Starting with the (L)APW(+lo) overlap, one should initially appreciate that, apart from the radial integrals, no intermediate numeric steps have been taken to acquire the wavefunction overlaps. Once the radial integrals, Gaunt numbers and region II expressions, the latter found on the bottom line of (3.26), are computed for a particular set of bands and spin orientations, the overlap $G_{\mu\mu'}$ is entirely given by the (L)APW(+lo) basis coefficients. Performing a Brillouin-zone integral for the overlap amounts to varying the basis coefficients with respect to $\boldsymbol{k}$; for each k-point, a linear combination of two sets of basis coefficients is computed, while the radial integrals and Gaunt coefficients, which may be stored in advance, are reused for each grid point. The overlap for a given pair of wavevectors is readily extracted with the same level of detail as the (L)APW(+lo) coefficients themselves.

Comparably, the Wannier overlap involves an intermediate step, in which Wannier coefficients are constructed from the (L)APW(+lo) coefficients. Remember that the Wannier coefficients do not depend on wavevector $\boldsymbol{k}$; rather, they are labeled by a Bravais lattice vector $\boldsymbol{R}$. As seen from (3.30), the $\boldsymbol{k}$ dependence is inherited by $e^{-i\boldsymbol{k}'\cdot\boldsymbol{0}_{\boldsymbol{R}}+i\boldsymbol{k}\cdot\boldsymbol{R}}$ and the unitary matrices. To compute the Wannier integrals, we reuse the routines used to evaluate the radial integrals, Gaunt numbers, and region II lattice sums for the (L)APW(+lo) scheme. Once the Wannier integral has been computed, an integral over the Brillouin-zone amounts to collecting contributions from varying $\boldsymbol{k}$-points on which the overlap is tabulated. Through Wannier interpolation, a fine mesh is obtained efficiently at which the overlap is accurately tabulated.

Chapter 5

Results

Most of the time spent on this thesis has been devoted to implementing a working program which computes the normal (L)APW(+lo) overlap between two wavefunctions at arbitrary k-point. We apply this to GaAs to investigate bands principal in transport phenomena. In particular, we look at the wavefunction distribution between the atomic spheres and the interstitial region for these near-band edge states.

5.1 GaAs

A Wien2k-simulation has been run for GaAs. Since the overlap program has not yet been generalized to account for different spin states, the simulation excludes spin-orbit coupling. We are primarily interested in the bands central in carrier transport; these are highlighted with band index and color in figure 5.1.

According to figure 5.1, the edge of the valence band has a 6-fold degeneracy, with bands 12-14 all coinciding at $k = \Gamma$, each band associated with two spin states. The central-cell area of the mentioned bands is primarily made up of p-orbitals. In figure 5.1, bands 12, 13 and 14 are given in yellow, black and blue, respectively. The valence band edge 6-fold degeneracy disagrees with experiments, which instead reveal a 4-fold degeneracy. Had spin-orbit effects been included, the correct 4-fold degeneracy would be present at the valence band edge of figure 5.1 [2].

The conduction band edge has band index 15, and is given in red in figure 5.1. As shown, GaAs has a direct band gap for which the conduction band edge has a central-cell area of s-orbital character. The next conduction band valley is found near the X-point. Further up, directly above the conduction band edge, at $k = \Gamma$, bands 16-18 form a degenerate valley. Like for the valence band edge, the bands are superposed of p-orbitals, but in this case antibonding orbitals are formed, lying higher in energy than the corresponding bonding

orbitals [58].

The norm has been computed for bands 11-19 at $k = \Gamma$ and $k = L$. In figures 5.2 and 5.3, the total norm as well as the contributions from $|J_{n\boldsymbol{k},n'\boldsymbol{k'}}|$ and $|J_{n\boldsymbol{k},n'\boldsymbol{k'}}|$ are shown.

Wien2k distinguishes between three kinds of states: core, semi-core and valence states [59]. Core states are entirely confined to the atomic spheres of region I. Semi-core states have a few percent of their charge outside the atomic spheres, but are predominantly in region I. Finally, valence states have a significant charge distributed to the interstitial region.

As expected when computing the norm, values very close to 1 are obtained. This holds true for all bands both for $k = \Gamma$ and $k = L$, regardless of how the wavefunction is distributed between the two regions.

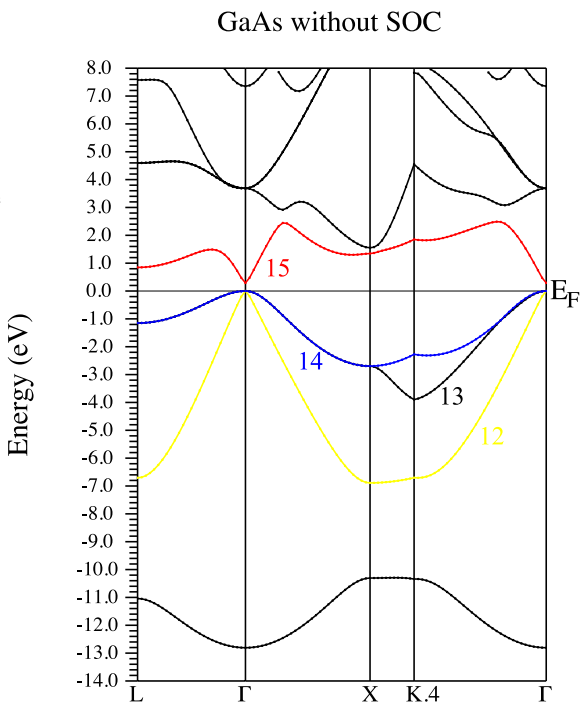

Figure 5.1: *Band structure of GaAs calculated with first principles program Wien2k. Spin-orbit coupling effects are not included. Bands 12-15 are of principal interest in transport phenomena and have been highlighted with band indices and colors. GaAs has a direct bandgap at k-point Γ, correctly predicted in this simulation. On the other hand, a 6-fold valence band edge is incorrectly predicted due to the exclusion of spin-orbit coupling effects; had these been included, a split-off band would form, yielding a correct 4-fold valence band edge.*

Shown in figure 5.1, band 11 is the lowest in energy. At the origin, only a few percent of the interstitial region contributes. Accordingly, we categorize it as a semi-core state. For $k = L$, the norm has a significant portion of its contribution from the interstitial region, so here, band 11 is a valence state.

At $k = \Gamma$, bands 12-14 constitute the top of the valence band. Here, the top of the valence band is made of p-orbitals. These must transform into one another as one rotates the wavefunctions with an angle corresponding to a symmetry operation for a Zinc Blende crystal. Bands 12-14 are therefore expected to have identical distribution of the norm between region I and II. Furthermore, the interstitial region is expected to host more of the wavefunction for higher-lying bands as these are more energetic. Peculiarly, band 12, compared to bands 13 and 14, has a larger portion of its wavefunction in the interstitial region. At the same time, the wavefunction of band 15 is distributed identically with that of bands 13 and 14. For a given band, it is the atomic spheres of region I that dictate

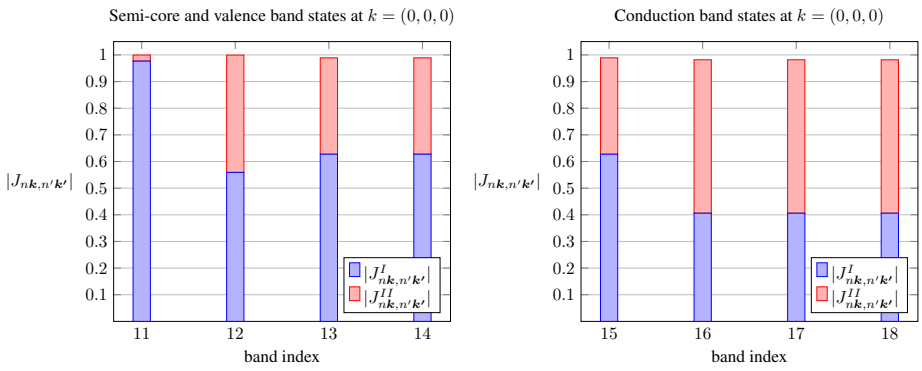

Figure 5.2: $|J_{n\boldsymbol{k},n'\boldsymbol{k'}}|$, *plotted at k-point* Γ *for bands 11-18, as given by Wien2k. Bands 12-14 constitute the top of the valence band, and are in the central-cell area made up of p-orbitals. These should transform into one another as one rotates them by an angle corresponding to a symmetry operation for a Zinc Blende crystal. Since band 12 has a larger portion of its wavefunction in the interstitial region, that is however impossible. Interestingly, band 15 is distributed identically with bands 13 and 14 between the atomic spheres and the interstitial region. This indicates that wavefunctions for bands 12 and 15 have been alternated in Wien2k, giving an incorrect band edge description. How this alternation has happened is unknown. At* $k = \Gamma$*, bands 16-18 should, like bands 12-14, also transform into one another as one rotates them by an angle corresponding to a symmetry operation for a Zinc Blende crystal. Being identically distributed between the atomic spheres and the interstitial region, this is in agreement with the band structure in 5.1.*

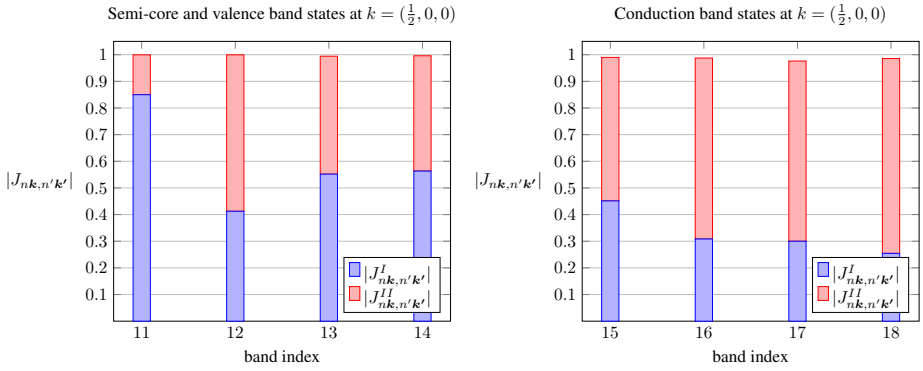

Figure 5.3: $|J_{n\boldsymbol{k},n'\boldsymbol{k'}}|$ *plotted at k-point L for bands 11-18, as given by Wien2k. Compared to wavefunctions at* $k = \Gamma$*, the interstitial region hosts a larger portion of the norm. In particular, at the origin, band 11 is a semi-core state; at* $k = L$*, it is a valence state. Oddly, the wavefunction of band 12 is weighted closer to the nucleus than band 15, indicating that bands 12 and 15 have been alternated. How this alternation has happened is unknown. Compared to* $k = \Gamma$*, we also see that the degeneracy for bands 16-18 has been lifted: whereas p-orbitals make up bands 16-18 at* $k = \Gamma$*, other orbitals mix in at* $k = L$ *to lift the degeneracy.*

the wavefunction distribution between region I and II. Yet, the atomic spheres are chosen arbitrarily; an accidental identical distribution of the wavefunction for bands 13-15 is

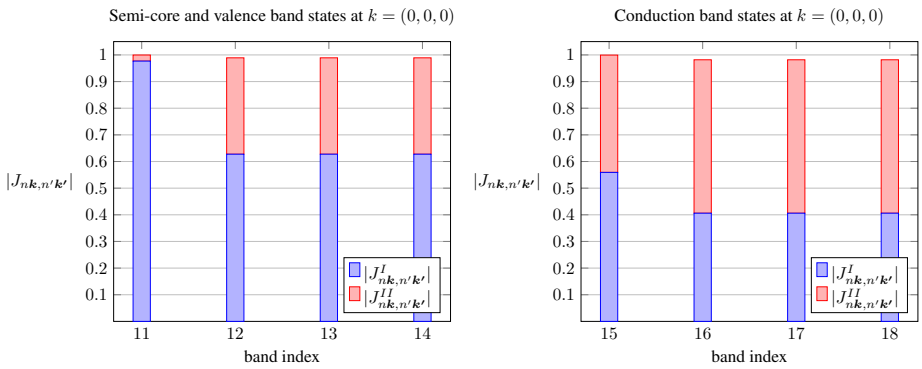

Figure 5.4: $|J_{n\boldsymbol{k},n'\boldsymbol{k}'}|$ *plotted at k-point* Γ *for bands 11-18. The wavefunction-to-band correspondence has been modified by alternating the wavefunctions for bands 12 and 15, restoring the valence band edge symmetry. Furthermore, the first conduction band's larger weight in the interstitial region, as compared with bands 13 and 14, is now appropriate as band 15 is a conduction band state.*

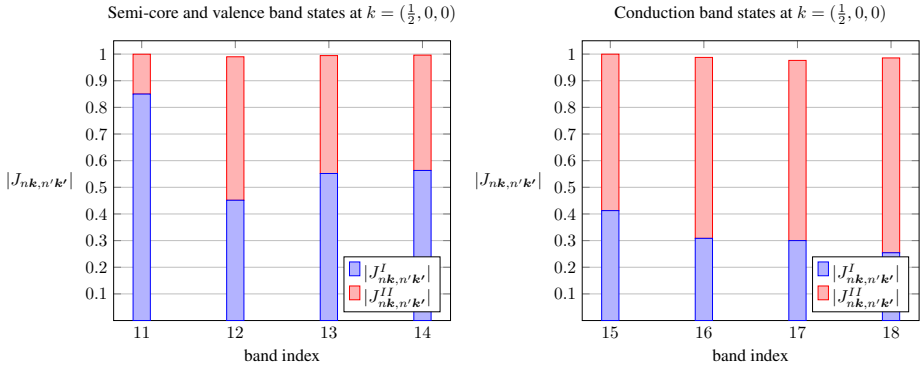

Figure 5.5: $|J_{n\boldsymbol{k},n'\boldsymbol{k}'}|$ *plotted at k-point L for bands 11-18. The wavefunction-to-band correspondence has been corrected. Compared to the valence bands, band 15 now appropriately has a larger contribution from the interstitial region.*

extremely unlikely. Assuming the wavefunction of band 12 has been alternated with that of band 15, the valence band edge symmetry is restored, and the first conduction band's larger weight in the interstitial region, as compared with bands 13 and 14, is appropriate. Hence, we conclude that the printed wavefunctions for bands 12 and 15 have somehow been alternated, presumably in Wien2k. Why this alternation has occurred is unknown. The alternation has been corrected in figures 5.4 and 5.5.

For $k = L$, we observe that for the valence bands 12-14, the interstitial region contributes more to the overlap than at $k = \Gamma$. The same holds true for band 15, having a majority of its charge in the interstitial region. Furthermore, the valence bands 12-14 no longer have identical wavefunction distribution between regions I and II. From figure 5.1, this is seen in light of the band degeneracy having been lifted at $k = L$. While the wavefunction of

band 12-14 is primarily superposed of p-orbitals near $k = \Gamma$, other orbitals mix in as one moves towards $k = L$.

As seen from figure 5.1, bands 16-18 form a second conduction band valley at $k = \Gamma$. Here, electrons are constructed using the same p-orbitals as those for bands 12, 13 and 14, but for bands 16-18 superposed to form antibonding orbitals. As expected, the norm is distributed between region I and II identically, as shown in figure (5.4). About 60% of the norm contribution comes from region II for all three bands.

At $k = L$, roughly 70% of the norm comes from region II. Here, analogous to bands 12-14, other orbitals mix in to lift the degeneracy as compared with $k = \Gamma$ where only p-orbitals participate. At $k = L$, band 16 has a slightly smaller contribution from region II than band 17, and band 17 has a slightly smaller contribution from region II than band 18. The clear correspondence between bands 12-14 and bands 16-18 further strengthens the theory that wavefunctions of bands 12 and 15 have been alternated in Wien2k.

Chapter 6

Conclusion

During the work with this master thesis, several achievements have been made. First, the wavefunction overlap factor in the bases (L)APW(+lo) and MLWFs has been derived. Both expressions are suitable for numeric integration over the Brillouin-zone, allowing us to use them in the MC program to simulate carrier transport in semiconductor materials. The Wannier overlap should eventually be used to compute the wavefunction overlap on a coarse mesh before Wannier interpolation is used to generate a finer mesh inexpensively.

The (L)APW(+lo) wavefunction overlap routine has been implemented and tested on a Wien2k-simulation for GaAs. A direct band gap is correctly predicted, but at the same time, an incorrect 6-fold valence band edge is incorrectly predicted due to the exclusion of spin-orbit effects. With regard to the band edge wavefunctions, a norm very close to 1 was obtained for bands 11-19 both for $k = \Gamma$ and $k = L$. Furthermore, the wavefunction distribution between an interstitial region and atomic spheres, respectively, has been investigated. Somehow, wavefunctions for bands 12 and 15 have been alternated in Wien2k. The cause of this alternation is unknown, so it was corrected manually. Electron states for higher bands tend to have a larger portion of their norm contribution from the interstitial region. Also, electron states for $k = L$, compared to states at $k = \Gamma$, tend to have a larger portion of their norm contribution from the interstitial region. Finally, for bands 12-14, and bands 16-18, respectively, the wavefunction distribution between the mentioned regions is identical at $k = \Gamma$, in agreement with degeneracies evident fromthe GaAs band structure.

Although a working implementation has been tested for the (L)APW(+lo), it applies only to the normal (L)APW(+lo) overlap. It should be generalized to Umklapp processes and also take spin states into account.

Finally, a scheme has been developed for Wannier overlaps. It is worthwhile to implement this scheme, allowing us to capitalize on Wannier interpolation.

Bibliography

[1] D. Vasileska, D. Mamaluy, H. R. Khan, K. Raleva, and S. M. Goodnick. Semiconductor device modeling. *Journal of Computational and Theoretical Nanoscience*, 5(6):999–1030, 2008.

[2] Dara Goldar. A preliminary Survey on Wavefunction Overlaps in (L)APW and Wannier function Bases (Specialization project). Technical report, Norwegian University of Science and Technology, 2016.

[3] Peter Blaha, Karlheinz Schwarz, and Georg K. H. Madsen. WIEN2K, An Augmented Plane Wave+ Local Orbitals Program for Calculating Crystal Properties (TU Wien, Austria, 2001). *Isbn 3-9501031-1-2*, page 254, 2001.

[4] Asta Katrine Storebø, Dara Goldar, and Trond Brudevoll. Simulation of infrared avalanche photodiodes from first principles. In *Proc. SPIE 10177, Infrared Technology and Applications XLIII*, pages 101771B–101771B–10, 2017.

[5] Carlo Jacoboni and Paolo Lugli. *The Monte Carlo Method for Semiconductor Device Simulation*. Springer-Verlag Wien New York, 1st edition, 1989.

[6] X. Gonze, B. Amadon, P. M. Anglade, J. M. Beuken, F. Bottin, P. Boulanger, F. Bruneval, D. Caliste, R. Caracas, M. Côté, T. Deutsch, L. Genovese, Ph Ghosez, M. Giantomassi, S. Goedecker, D. R. Hamann, P. Hermet, F. Jollet, G. Jomard, S. Leroux, M. Mancini, S. Mazevet, M. J T Oliveira, G. Onida, Y. Pouillon, T. Rangel, G. M. Rignanese, D. Sangalli, R. Shaltaf, M. Torrent, M. J. Verstraete, G. Zerah, and J. W. Zwanziger. ABINIT: First-principles approach to material and nanosystem properties. *Computer Physics Communications*, 180(12):2582–2615, 2009.

[7] Bjørnar Karlsen. Calculation of phonon and alloy scattering rates in zincblende structures using 14 x 14 kp and "ab initio" pesudopotential methods (Master thesis). Technical report, Norwegian University of Science and Technology, 2013.

[8] Tore Sivertsen Bergslid. Implementing a full-band Monte Carlo model for zincblende

structure semiconductors (Master thesis). Technical report, Norwegian University of Science and Technology, 2013.

[9] Juri Selvåg. High Precision, Full Potential Electronic Transport Simulator: Implementation and First Results (Master thesis). Technical report, Norwegian University of Science and Technology, 2014.

[10] J. Singh. Electronic and optoelectronic properties of semiconductor structures. *Annals of Physics*, 54(7):258, 2003.

[11] John P. Perdew. Density functional theory and the band gap problem. *International Journal of Quantum Chemistry*, 28(S19):497–523, 2009.

[12] Fabien Tran and Peter Blaha. Accurate band gaps of semiconductors and insulators with a semilocal exchange-correlation potential. *Physical Review Letters*, 102(22), 2009.

[13] O. Rubel, A. Bokhanchuk, S. J. Ahmed, and E. Assmann. Unfolding the band structure of disordered solids: From bound states to high-mobility Kane fermions. *Physical Review B - Condensed Matter and Materials Physics*, 90(11), 2014.

[14] Nicola Marzari, Arash A. Mostofi, Jonathan R. Yates, Ivo Souza, and David Vanderbilt. Maximally localized Wannier functions: Theory and applications. *Reviews of Modern Physics*, 84(4):1419–1475, 2012.

[15] Jan Kuneš, Ryotaro Arita, Philipp Wissgott, Alessandro Toschi, Hiroaki Ikeda, and Karsten Held. Wien2wannier: From linearized augmented plane waves to maximally localized Wannier functions. *Computer Physics Communications*, 181(11):1888–1895, 2010.

[16] Arash A. Mostofi, Jonathan R. Yates, Young Su Lee, Ivo Souza, David Vanderbilt, and Nicola Marzari. wannier90: A tool for obtaining maximally-localised Wannier functions. *Computer Physics Communications*, 178(9):685–699, 2008.

[17] Georg K. H. Madsen and David J. Singh. BoltzTraP. A code for calculating band-structure dependent quantities. *Computer Physics Communications*, 175(1):67–71, 2006.

[18] Giovanni Pizzi, Dmitri Volja, Boris Kozinsky, Marco Fornari, and Nicola Marzari. BoltzWann: A code for the evaluation of thermoelectric and electronic transport properties with a maximally-localized Wannier functions basis. *Computer Physics Communications*, 185(1):422–429, 2014.

[19] G. Gilat and L. J. Raubenheimer. Accurate Numerical Method for Calculating Frequency Distribution Functions in Solids. *Physical Review*, 147(2):670–670, 1966.

[20] Massimo Fischetti and Steven Laux. Monte carlo analysis of electron transport in small semiconductor devices including band-structure and space-charge effects. *Physical Review B*, 38(14):9721–9745, 1988.

[21] Warren E. Pickett, Henry Krakauer, and Philip B. Allen. Smooth Fourier interpola-

tion of periodic functions. *Physical Review B*, 38(4):2721–2726, 1988.

[22] Claudia Ambrosch-Draxl and Jorge O. Sofo. Linear optical properties of solids within the full-potential linearized augmented planewave method. *Computer Physics Communications*, 175(1):1–14, 2006.

[23] Xinguo Ren, Patrick Rinke, Christian Joas, and Matthias Scheffler. Random-phase approximation and its applications in computational chemistry and materials science. *Journal of Materials Science*, 47(21):7447–7471, 2012.

[24] Antoine Georges, Gabriel Kotliar, Werner Krauth, and Marcelo J. Rozenberg. Dynamical mean-field theory of strongly correlated fermion systems and the limit of infinite dimensions. *Reviews of Modern Physics*, 68(1):13–125, 1996.

[25] G. Kotliar, S. Y. Savrasov, K. Haule, V. S. Oudovenko, O. Parcollet, and C. A. Marianetti. Electronic structure calculations with dynamical mean-field theory. *Reviews of Modern Physics*, 78(3):865–951, 2006.

[26] E. Assmann, P. Wissgott, J. Kuneš, A. Toschi, P. Blaha, and K. Held. Woptic: Optical conductivity with Wannier functions and adaptive k-mesh refinement, 2015.

[27] F. Tran. *(private communication)*.

[28] Einar Halvorsen. Numerical calculation of valence band structure and hole scattering rates in GaAs. 1991.

[29] T. Brudevoll, T. A. Fjeldly, J. Baek, and M. S. Shur. Scattering rates for holes near the valence-band edge in semiconductors. *Journal of Applied Physics*, 67(12):7373–7382, 1990.

[30] B. K. Ridley. *Quantum processes in semiconductors: Fifth edition*. Oxford University Press, 1999.

[31] W. Kohn and L. J. Sham. Self-consistent equations including exchange and correlation effects. *Physical Review*, 140(4A), 1965.

[32] H. Eschrig and W.E. Pickett. Density functional theory of magnetic systems revisited. *Solid State Communications*, 118(3):123–127, 2001.

[33] Burak Himmetoglu, Andrea Floris, Stefano De Gironcoli, and Matteo Cococcioni. Hubbard-corrected DFT energy functionals: The LDA+U description of correlated systems. *International Journal of Quantum Chemistry*, 114(1):14–49, 2014.

[34] Hal Tasaki. The Hubbard model - an introduction and selected rigorous results. *Journal of Physics: Condensed Matter*, 10(20):4353, 1998.

[35] Vladimir I. Anisimov, Jan Zaanen, and Ole K. Andersen. Band theory and Mott insulators: Hubbard U instead of Stoner I. *Physical Review B*, 44(3):943–954, 1991.

[36] V. I. Anisimov, I. V. Solovyev, M. A. Korotin, M. T. Czyyk, and G. A. Sawatzky. Density-functional theory and NiO photoemission spectra. *Physical Review B*, 48(23):16929–16934, 1993.

[37] Gyaneshwar P. Srivastava. Broyden's method for self-consistent field convergence acceleration. *Journal of Physics A: Mathematical and General*, 17(13):2737, 1984.

[38] David J. Singh and Lars Nordstrom. *Planewaves, pseudopotentials and the LAPW method: Second edition*. Springer, 2006.

[39] Max Planitz. LAPACK Users Guide. *The Mathematical Gazette*, 79(484):210, 1995.

[40] Karlheinz Schwarz. DFT calculations of solids with LAPW and WIEN2k. *Journal of Solid State Chemistry*, 176(2):319–328, 2003.

[41] E. Sjöstedt, L. Nordström, and D. J. Singh. Alternative way of linearizing the augmented plane-wave method. *Solid State Communications*, 114(1):15–20, 2000.

[42] Georg K. H. Madsen, Peter Blaha, Karlheinz Schwarz, Elisabeth Sjöstedt, and Lars Nordström. Efficient linearization of the augmented plane-wave method. *Physical Review B*, 64(19):1–9, 2001.

[43] John C. Slater. Wave functions in a periodic potential. *Physical Review*, 51:846, 1937.

[44] A. H. MacDonald, W. E. Picket, and D. D. Koelling. A linearised relativistic augmented-plane-wave method utilising approximate pure spin basis functions. *Journal of Physics C: Solid State Physics*, 13(14):2675, 1980.

[45] Gregory H. Wannier. The structure of electronic excitation levels in insulating crystals. *Physical Review*, 52(3):191–197, 1937.

[46] E. I. Blount. Formalisms of Band Theory. *Solid State Physics - Advances in Research and Applications*, 13(C):305–373, 1962.

[47] Hendrik J. Monkhorst and James D. Pack. Special points for Brillouin zone integrations. *Physical Review B*, 13(12):5188–5192, 1976.

[48] Herbert H.H. Homeier and E.Otto Steinborn. Some properties of the coupling coefficients of real spherical harmonics and their relation to Gaunt coefficients. *Journal of Molecular Structure: THEOCHEM*, 368:31–37, 1996.

[49] J. Rasch and A. C. H. Yu. Efficient Storage Scheme for Precalculated Wigner 3 j , 6 j and Gaunt Coefficients. *SIAM Journal on Scientific Computing*, 25(4):1416–1428, 2004.

[50] J. K. Dewhurst, S. Sharma, and C. Ambrosch-Draxl. The EXCITING Code Manual. Technical report, 2015.

[51] Gianluca Panati and Adriano Pisante. Bloch Bundles, Marzari-Vanderbilt Functional and Maximally Localized Wannier Functions. *Communications in Mathematical Physics*, 322(3):835–875, 2013.

[52] W. Kohn. Localized basis for lattice vibrations. *Physical Review B*, 7(6):2285–2287, 1973.

[53] Feliciano Giustino, Jonathan R. Yates, Ivo Souza, Marvin L. Cohen, and Steven G. Louie. Electron-phonon interaction via electronic and lattice Wannier functions: Superconductivity in boron-doped diamond reexamined. *Physical Review Letters*, 98(4), 2007.

[54] Ivo Souza, Nicola Marzari, and David Vanderbilt. Maximally localized Wannier functions for entangled energy bands. *Physical Review B*, 65(3):035109, 2001.

[55] Laurence Marks. www.mail-archive.com/wien@zeus.theochem.tuwien.ac.at/msg13167.html. Accessed 2017.07.11, 2015.

[56] Laurence. Marks. www.mail-archive.com/wien@zeus.theochem.tuwien.ac.at/msg15875.html. Accessed 2017.07.11., 2017.

[57] P. E. Blöchl, O. Jepsen, and O. K. Andersen. Improved tetrahedron method for Brillouin-zone integrations. *Physical Review B*, 49(23):16223–16233, 1994.

[58] Charles Kittel. *Introduction to Solid State Physics: Fourth edition*. John Wiley & Sons, Inc, 2010.

[59] K. Schwarz, P. Blaha, and Georg K. H. Madsen. Electronic structure calculations of solids using the WIEN2k package for material sciences. *Computer Physics Communications*, 147(1-2):71–76, 2002.